Materials Science and Engineering R 77 (2014) 1–34

Contents lists available at ScienceDirect

Materials Science and Engineering R

journal homepage: www.elsevier.com/locate/mser

Biodegradable metals

Y.F. Zheng [a,b,*], X.N. Gu [c], F. Witte [d]

[a] State Key Laboratory for Turbulence and Complex System and Department of Materials Science and Engineering, College of Engineering, Peking University, Beijing 100871, China
[b] Shenzhen Key Laboratory of Human Tissue Regeneration and Repair, Shenzhen Institute, Peking University, Shenzhen 518057, China
[c] Key Laboratory for Biomechanics and Mechanobiology of Ministry of Education, School of Biological Science and Medical Engineering, Beihang University, Beijing 100191, China
[d] Julius Wolff Institute and Center for Musculoskeletal Surgery, Berlin-Brandenburg Center for Regenerative Therapies, Charité – Universitätsmedizin Berlin, Augustenburger Platz 1, 13353 Berlin, Germany

ARTICLE INFO

Article history:
Available online

Keywords:
Biodegradable metals
Magnesium alloys
Iron
Corrosion
Biocompatibility

ABSTRACT

After decades of developing strategies to minimize the corrosion of metallic biomaterials, there is now an increasing interest to use corrodible metals in a number of medical device applications. The term "biodegradable metal" (BM) has been used worldwide to describe these new kinds of degradable metallic biomaterials for medical applications and there were many new findings reported over the last decade. In this paper, the definition of BM and its classification are given for the first time, along with the summary of the degradation mechanisms of BMs and its environmental influencing factors, which includes the degeneration of mechanical integrity and the metabolism of the degradation products. The recently-developed representative Mg-based BMs (pure Mg, Mg–Ca alloy, Mg–Zn alloy, etc.), Fe-based BMs (pure Fe, Fe–Mn-based alloys, etc.) and other BMs (pure W, pure Zn and its alloys, Ca-based and Sr-based bulk metallic glasses, etc.) were comprehensively reviewed with emphases on their microstructures, mechanical properties and degradation behaviors, *in vitro* and *in vivo* performances, pre-clinical and clinical trials. Moreover, current approaches to control their biodegradation rates to match the healing rates of the host tissues with various surface modification techniques and novel structural designs are summarized. Finally, this paper comprehensively discusses the directions of future development and the challenges of transitioning BMs from raw materials to semi-products to final medical devices. All in all, BM belongs to "bioactive" biomaterials and its future research and development direction should lean towards "third-generation biomedical materials" with "multifunctional capabilities" in a controllable manner to benefit the local tissue reconstruction.

Contents

* Corresponding author at: Department of Materials Science and Engineering, College of Engineering, Peking University, Beijing 100871, China. Tel.: +86 10 6276 7411; fax: +86 10 6276 7411.
E-mail address: yfzheng@pku.edu.cn (Y.F. Zheng).

http://dx.doi.org/10.1016/j.mser.2014.01.001
0927-796X/

1. Introduction

1.1. Definition and classification of biodegradable metals

The traditional paradigm of metallic biomaterials requires metals with improved corrosion resistance in the body. A new class of biodegradable materials – so called "biodegradable metals" (BMs) – has been breaking this paradigm recently, emerging as an alternative for biomedical implants.

The definition of BMs can be given as follows: BMs are metals expected to corrode gradually *in vivo*, with an appropriate host response elicited by released corrosion products, then dissolve completely upon fulfilling the mission to assist with tissue healing with no implant residues. Therefore, the major component of BM should be essential metallic elements that can be metabolized by the human body, and demonstrate appropriate degradation rates and modes in the human body.

From the point of view of the materials science, BM can be classified as follows:

1. "Pure metals" (BM-PM)

This category includes the metals mainly composed of one metallic element, with impurity levels lower than the commercial tolerance limits. The corrosion rates of biodegradable metals in this category are mainly driven by the included trace of impurities.

2. "Biodegradable alloys" (BM-BA)

This category encompasses biodegradable metals with various microstructures and one or more alloying elements. Given the concerns for bio-safety of the corrosion products, the alloying elements and their quantities should be controlled without causing adverse pathophysiological and toxicological effects. BM-BA also encompasses biodegradable metallic glasses and biodegradable single crystal metals, which exhibit glassy or single crystal states, respectively, and intend to readily corrode in the human body.

3. "Biodegradable metal matrix composites" (BM-MC)

This category requires that all components within the composites are biodegradable with the major component being

a biodegradable metal. Fundamentally, the bottom line is that the materials are non-toxic to the body.

When metals react with body fluid, they give away electrons and form positive ions. In electrochemistry, the values of standard electrode potential provide a way to compare the relative ease of different metal elements to lose electrons to form ions in solutions. For some metals, they have a much greater tendency to form their ions than hydrogen does; an element is more ready to lose electrons and forms ions, the more negative its standard electrode potential value is. In other words, the more negative the standard electrode potential value is, then the more readily the metal degrades in an aqueous solution. The standard electrode potentials in an aqueous solution at 25 °C are −3.04 V for $Li^{+}_{(aq)} + e^{-} \rightarrow Li_{(s)}$, −2.93 V for $K^{+}_{(aq)} + e^{-} \rightarrow K_{(s)}$, −2.90 V for $Ba^{2+}_{(aq)} + 2e^{-} \rightarrow Ba_{(s)}$, −2.89 V for $Sr^{2+}_{(aq)} + 2e^{-} \rightarrow Sr_{(s)}$, −2.87 V for $Ca^{2+}_{(aq)} + 2e^{-} \rightarrow Ca_{(s)}$, −2.71 V for $Na^{+}_{(aq)} + e^{-} \rightarrow Na_{(s)}$, −2.37 V for $Mg^{2+}_{(aq)} + 2e^{-} \rightarrow Mg_{(s)}$, −1.18 V for $Mn^{2+}_{(aq)} + 2e^{-} \rightarrow Mn_{(s)}$, −0.76 V for $Zn^{2+}_{(aq)} + 2e^{-} \rightarrow Zn_{(s)}$, −0.44 V $Fe^{2+}_{(aq)} + 2e^{-} \rightarrow Fe_{(s)}$, and −0.14 V for $Sn^{2+}_{(aq)} + 2e^{-} \rightarrow Sn_{(s)}$ [1,2]. Among these metals, magnesium (Mg) and iron (Fe) based alloys have been extensively studied in recent years, and Li, Ca, Sr, Mn, Zn and Sn have been added into Mg or Fe to form various alloys.

1.2. Development of biodegradable metals

The earliest recorded use of Fe to repair the human body was a Fe dental implant. It was properly integrated into bone found in Europe that dated back to 200 A.D. [3,4]. Hieronymus Fabricius used Fe wires as sutures in the 17th century [4]. In 1775, Fe wires were used for fracture fixations, though concomitant infections were observed [5]. In 1906, Lambotte used Fe plates and screws for fracture fixation in a 17-year-old, but this treatment was a clinical failure due to loosely attached fractured ends four months after surgery [6,7]. Zierold [3,7] reported a study on bone tissue reaction to various metals in 1924 and found that Fe exhibited fast corrosion leading to the resorption of adjacent bone and that Mg and zinc (Zn) discolored the surrounding tissue.

In contrast to the sparse investigations of Fe and its alloys, surgeons have explored Mg and its alloys for numerous clinical applications, including the cardiovascular, musculoskeletal and general surgery, for nearly 100 years [7]. The investigation of Mg for clinical use started approximately in 1878 by Edward Huse [7,8], who successfully utilized a pure Mg wire ligature to stop hemorrhaging blood vessels. Several designs of Mg implants, including tubes, plates, sheets, and woven wires, had been developed as sutures or intestine, vessel, and nerve connectors in cardiovascular and other general surgeries [7]. In 1900, Payr introduced the use of tubular Mg connectors for the anastomosis of vessels [9,10]. The connection between the arterial and venous blood vessel ends solidified after eight days of implantation, with a severely thickened intima layer at the anastomosis and returned to normal thickness thereafter. Only the Mg tubes that were placed intravascularly caused thrombotic blood clotting at the end of the tubes, but no thrombosis was observed when the Mg tubes were placed extravascularly [7]. The Mg connectors were also successfully used for intestinal and nerve anastomosis in several animal trials as well as in humans [7,9–11]. During this same period, Payer also successfully used Mg sheets and plates to suture well-vascularized parenchymatous organs such as the liver and spleen in humans [7,9,10].

Given the blood clotting effect observed in animal trials and humans [9,10], efforts were made to treat aneurysms by inserting Mg arrows or wires in haemangiomas to enhance blood clotting from the mechanical destruction of the endothelium and the septa of the tumor, which leads to early transformation of a haemangioma into a fibrous granulation tissue [12–14]. Since no gas embolization was observed in patients [12,13], Mg implants were used in this clinical application by Payr [13,15], Sonntag [16], Glass [17] and Wilflingseder [18] for various types of haemangioma treatments.

For musculoskeletal applications, Mg implants, including fixation pins, nails, screws, wires (cerclage), pegs, cramps, sheets and plates, were developed for bone fracture treatments in several animal trials and in humans [7]. In 1907, Lambotte [6] used a Fe wire cerclage and an Mg plate with six steel screws to stabilize the fracture of the lower leg. Extensive subcutaneous gas cavities, local swelling and pain were observed one day post-surgery [6], which were caused by the fast corrosion of Mg due to the electrochemical reaction between Mg and Fe. Lambotte learned that to prevent galvanic corrosion of the Mg it should not be implanted with other metals. With such knowledge in mind, he started his investigation for Mg with his assistant Verbrugge [7]. In total, they reported 25 clinical cases using Mg and its alloys (Dow metal AZ63 and Electron Mg–8 wt.% Al) for fracture treatments in the next several years [6,19–21]. In these cases, the total resorption of Mg was observed over a period, ranging from three weeks to one year depending on the implant dimension and size and the site of implantation in the body. In the case of fast Mg dissolution within three weeks, an Mg plate and screw fixations were used and the bone fracture line was no longer visible after three weeks [19]. In addition to fast implant corrosion, patients reported a temporary numb feeling at the implantation site during Mg degradation, while no signs of infection or adverse reactions of skin, soft tissue, bone and joints were observed [19,21]. McBride reported that Mg could stimulate the early proliferation of connective tissues and overproduction of calluses, which were not firm during the early healing stage [22]. In 1940, Maier [23] used pins made of spindle-shaped Mg sheets in a humerus fracture, and the patient demonstrated positive functional results in the following 14 years. Troitskii and Tsitrin reported on 34 cases of pseudarthrosis treated with Mg–Cd alloy plates and screws, which were absorbed completely and stimulated callus bone formations [24].

Although the investigations revealed obvious advantages of Mg alloys, they were abandoned at the time due to their undesirable degradation in addition to the boom of inert stainless steel [7]. In recent times, as Mg alloy technology advances, both the mechanical and corrosion properties have been improved. The idea of degradable metals has been rediscovered and has attracted greater attention for temporary implant materials. Therefore, several key issues for BMs, have been widely investigated over the last decade, including the selection of alloying elements, adjustment for microstructural and mechanical properties, biodegradation mechanisms and their influencing factors, control of degradation rates and ion release behavior, and *in vitro* and *in vivo* biocompatibilities of BMs.

1.3. Degradation mechanism and its influencing factors

1.3.1. Generalized degradation mechanism

The typical mode of degradation in BMs is through a corrosion process. The corrosion generally proceeds by an electrochemical reaction with electrolyte to produce oxides, hydroxides, hydrogen gas, or other compounds. In the nearly neutral physiological environment, the corrosion reactions involve the following anodic dissolution of the metal and the reduction reaction (cathodic reaction):

$$M \rightarrow M^{n+} + ne^{-} \quad \text{(anodic reaction)} \tag{1}$$

$$2H_2O + 2e^{-} \rightarrow H_2 + 2OH^{-} \quad \text{(cathodic reaction)} \tag{2}$$

$$2H_2O + O_2 + 4e^{-} \rightarrow 4OH^{-} \quad \text{(cathodic reaction)} \tag{3}$$

$$M^{n+} + nOH^{-} \rightarrow M(OH)_n \quad \text{(product formation)} \tag{4}$$

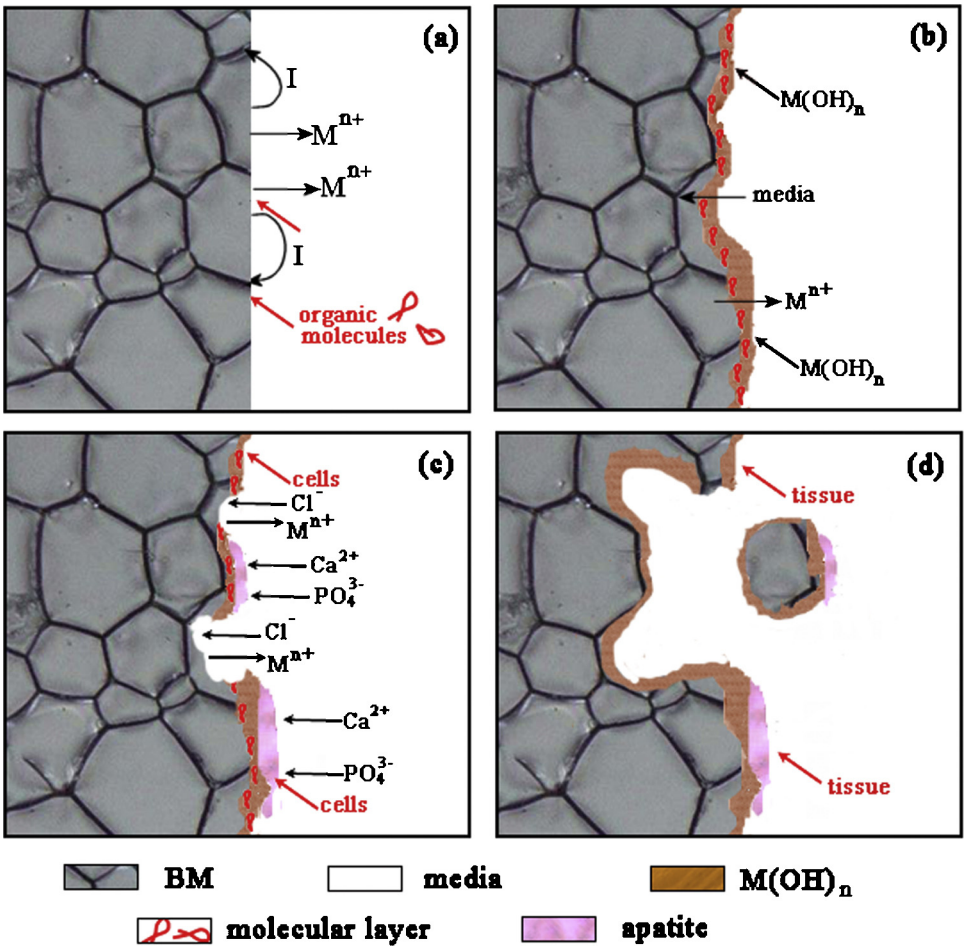

Fig. 1. Schematic diagram of the biocorrosion at BM/medium interface.

Fig. 1 illustrates the degradation mechanism of the BM in a physiological environment. Immediately after contacting the body fluid, the BM is oxidized into metal cations following the anodic reaction (Eq. (1)). The generated electrons are consumed by a cathodic reaction corresponding to the water reduction (Eq. (2)) for Mg-based BMs and the dissolved oxygen reduction (Eq. (3)) for Fe-based BMs. These reactions occur arbitrarily over the entire surface where a galvanic coupling forms due to different potentials between the metal matrix and intermetallic phase, or grain boundary, as shown in Fig. 1(a). Simultaneously, the organic molecules, such as proteins, amino acids and lipids, will adsorb over the metal surface, thereby influencing the dissolution of BM (Fig. 1(a) and (b)). The $M(OH)_n$ corrosion product layer is expected to form on the metal surface (Eq. (4)). However, the physiological environment is highly aggressive, especially due to the high concentration of chloride ions, which is normally fatal to the metallic hydroxide protective layer. Chloride adsorption causes the breakdown of the $M(OH)_n$ protective layer and leads to pitting corrosion (Fig. 1(c)). Generally, the corrosion of Fe-based BMs in pits is self-catalysis since the chloride ions tend to accumulate in pits and the pH of the solutions decreases in aqueous solutions [25]. The corrosion caused no alkalinization to Hank's solution [26] whereas the deep undermining of corrosion pits in Mg-based BMs rarely occurs given the fast localized alkalization and the repassivation of the $M(OH)_n$ layer. As the degradation proceeds, calcium phosphate based apatite deposits onto the undissolved $M(OH)_n$ layer due to the localized alkalization and the saturation of calcium and phosphate in the body fluid. Cells are also observed to adhere on the surface. With progressing implantation time, the adhered cells proliferate to form tissues adjacent to the corrosion product layer. Meanwhile, eroded BM may disintegrate from the whole BM matrix as irregular particles and fall into surrounding media. Such phenomenon is often observed on Mg-based BMs but rarely seen on Fe-based BMs. Depending on the particle size, the fibrous tissue or macrophages might enclose these particle, which may be further degraded until the metallic phase is completely exhausted (Fig. 1(d)).

1.3.2. Environmental Factors influencing the biodegradation behavior

1.3.2.1. Inorganic ions. The inorganic ions in physiological solutions usually influence the degradation of BM mainly in the following two manners: (i) the presence of Cl^-, one of the most abundant ions in physiological environment, is aggressive to the BMs by breaking down the passive film of corrosion products on the surface and leading to pitting corrosion [1,27]. The corrosion rates of Mg and Fe increase with increasing Cl^- concentrations up to ~3 wt.% NaCl [1,28]. SO_4^{2-} anion is also harmful to BMs, resulting in the degradation of the materials in a similar mechanism as caused by Cl^- ions [1]. (ii) The presence of HPO_4^{2-}/PO_4^{3-}, HCO_3^-/CO_3^{2-} anions and Ca^{2+} cations help to passivate Mg and Fe because they retard corrosion and form pits due to the precipitation of phosphate and carbonate salts [1,27,29,30]. For example, Xin et al. [27] ascribed the retarded corrosion rate to the multiple protection effects offered by magnesium phosphate and carbonate.

1.3.2.2. Buffering system. The buffering system is widely used to regulate the pH value of the simulated physiological solutions to

the near-neutral condition. The commonly used buffering agents in simulated body fluids include Hepes, Tris–HCl and HCO_3^-/CO_2, all of which significantly affect the degradation of Mg-based BMs [31]. The first two agents control the pH value by consuming the generated OH^- ions and they influence the corrosion product formation, which in turn accelerates the Mg dissolution, as shown in Eq. (4). HCO_3^-/CO_2, the most important buffering system in the human body (~27 mM), is not only capable of consuming the OH^- ions but also induces the precipitation of $MgCO_3$ that contributes to corrosion protection [31,32]. In contrast, the corrosion of Fe is insensitive to the pH value in the range of 4–10 in aerated water at room temperature [1], thus the buffering system will not be a concern for the biodegradation of Fe.

1.3.2.3. Organic molecules. For Mg-based BMs, many investigations confirmed that the delayed corrosion was due to the adsorption of proteins on the metal surface [29,32–34]. Yet the blocking effect of the adsorbed protein layer only matters in the initial degradation stage and weakens dramatically with an elongated immersion period [31,33]. In contrast, protein adsorption accelerates the corrosion of Fe-based BMs, as evidenced by the increased metal dissolution [35] and thicker carbon-rich films [36]. Omanovic et al. [37] and Tang et al. [38] found that the presence of bovine serum albumin (BSA) decreased the corrosion potential and enhanced the anodic dissolution of 304 and 316L stainless steels (SS). The adsorbed proteins such as albumin, serum, globulin, transferrin, and fibrinogen enhance the dissolution of pure iron (99.9 wt.%), 304 and 316L SS [35,38].

Amino acid is found to reduce the barrier effect of the insoluble salt layer against dissolution of Mg [29] and influencing Fe corrosion by inhibiting the iron phosphate formation [39].

1.3.2.4. Dissolved oxygen. According to electrochemical reactions in Eqs. (1) and (2), Mg-based BMs produce magnesium hydroxide and hydrogen gas and are thus relatively insensitive to oxygen concentration in the electrolyte. In contrast, dissolved oxygen is necessary for appreciable corrosion of Fe in near-neutral electrolytes (see Eq. (3)) [1]. It is indicated that the corrosion rate of mild steel is proportional to the dissolved oxygen concentration ranging 0–10 ppm at room temperature while increased oxygen concentration (10–25 ppm) leads to a reduced corrosion rate [1].

1.3.2.5. Stress. High strength is one of the most attractive properties for medical use of BMs in comparison with biodegradable polymers, which makes them promising for load-bearing applications. Many medical devices fabricated with BMs would work under complex stress environments *in vivo*, depending on the anatomical sites being implanted, and are expected to bear the combination of different kinds of mechanical loads, including tension, compression, and fluid shear stress, etc.

Altered degradation behaviors induced by tension and compression are observed for both Mg- and Fe-based BMs. For example, Gu et al. [40] reported the dramatically increased corrosion rate of as-cast AZ91D and as-extruded WE43 alloy under cyclic tension and compression loads far below the yield tensile stress. The corrosion rates of these two Mg-based BMs increased more than 10 times with an increasing applied load than that of unstressed ones. For Fe alloys, Bundy et al. [41,42] indicated that a plastically deformed 316L SS showed more than one order of magnitude higher corrosion current density than the samples stressed to the yield stress or non-loaded controls.

The flow of the electrolyte also has a significant effect on the corrosion of BM. For Mg-based BMs, the flow may produce fluid shear stress and influence the deposition of corrosion product layer or, on the other hand, take away the locally generated OH^- ions, thus affecting the corrosion behavior. For instance, Lévesque et al. [43] indicated that the relatively low shear stress (0.88 and 4.4 Pa) slowed down the corrosion of AM60B compared to the corrosion in static Hank's solution while higher shear stress (8.8 Pa) accelerated the corrosion. Chen et al. [44] reported enhanced corrosion of Mg–Zn alloys in m-SBF at a shear stress of 0.68 Pa. For Fe-based BMs, the blood flow brings the oxygen onto the metal surface and accelerates the corrosion rates. The corrosion of steel increased with the velocity of seawater ranging 0–7 m/s [1]. Additionally, the fluid shear stress may also be responsible for the accelerated corrosion without the influence of oxygen. Liu et al. [45] investigated the degradation of eight types of Fe-based BMs, including pure Fe, Fe–Mn, Fe–Co, Fe–Al, Fe–W, Fe–B, Fe–C, and Fe–S, in the circulating Hank's solution of dynamically applied 0.68 Pa of wall shear stress and dissolved oxygen concentration in the controlled range of 2.8–3.2 mg/l. The results revealed that these Fe-based BMs exhibited higher degradation rates than those immersed stilly in Hank's solution [45].

1.4. Degeneration of mechanical integrity with time

Adequate strength of the BM implants is desirable during healing and is critical for postoperative rehabilitation. As the degradation proceeds, the degeneration of mechanical integrity of BM can be expected. For instance, an initially fast reduction of bending strength and a slower reduction afterwards have been observed for Mg-based BMs [46,47]. The applied mechanical loads may accelerate this process due to the dual effect of corrosion and stress and lead to implants cracking (i.e. stress corrosion cracking (SCC) and corrosion fatigue). Mg-based BMs demonstrated a high susceptibility to SCC in SBF, as evidenced by the decreased tensile strength and time to fracture in slow strain rate test (SSRT) [48–50]. The reduction ratio of the strength was strongly influenced by the geometry of the tested samples [50]. Gu et al. [40] indicated that the as-cast AZ91D and extruded WE43 alloys exhibited over 50% loss of the fatigue limit in SBF at 37 °C in comparison with that in air. Although there was no report on the degeneration of mechanical integrity of Fe-based BM in physiological environments, the susceptibility of SCC and the degeneration of fatigue strength for the stainless steel in physiological solutions could be referenced [51].

1.5. Considerations on the biosafety of degradation products

The corrosion products generated by the gradually degraded BM implants may disturb the local physiological equilibrium at the implantation site. The bio-safety of each kind of degradation products has to be evaluated in the long-term. As shown from Eqs. (1) to (4), the degradation of BMs will give rise to metal cations, chemical reaction products (including the oxides, hydroxides, phosphates, and carbonates, etc.), change in local pH value, and hydrogen gas. Only below a certain concentration, these components (metal cations, hydrogen gas and hydroxyl ions) are tolerable and cause no harm to the host [52–55]. For example, high amounts of hydrogen gas generated per time interval can produce gas cavities, which are usually observed in the tissue around the implant, and can gradually diffuse into extracellular mediums that are constantly circulating depending on the local blood flow [53]. However, the gas cavities were not observed for most of the coated Mg-based BMs, which exhibit a slower initial degradation rate compared to the bare samples. The pathophysiology and toxicology of different metal cations will be later discussed in Section 2.

The precipitates of the solid metal salts produced by chemical reactions generally show relatively low solubility in aqueous solutions, which are difficult to eliminate from the human body. Table 1 summarizes the solubility values of the precipitates, reported as the corrosion products of BMs [27,56–58]. It can be

Table 1
The solubility product constant (K_{sp}) values at 25 °C for the metallic salts.

Hydroxides	K_{sp}	Carbonates	K_{sp}	Phosphates	K_{sp}
$Mg(OH)_2$	8.9×10^{-12}	$MgCO_3$	1×10^{-15}	$Mg_3(PO_4)_2$	1.04×10^{-24}
$Fe(OH)_2$	1.8×10^{-15}	–	–	–	–
$Fe(OH)_3$	4×10^{-38}				
$Zn(OH)_2$	4.5×10^{-17}	$ZnCO_3$	2×10^{-10}	$Zn_3(PO_4)_2$	9×10^{-33}
$Ca(OH)_2$	1.3×10^{-6}	$CaCO_3$	8.7×10^{-9}	$Ca_3(PO_4)_2$	1.3×10^{-32}

seen that $Mg(OH)_2$, the most common product of Mg-based BMs, displays moderate solubility and is found to slowly dissolve or react with chloride ions to become soluble $MgCl_2$. Janning et al. [59] reported the slow dissolution of a pure $Mg(OH)_2$ cylinder in the knees of rabbits who lost 19% of volume within six weeks. Other kinds of metal salts, including $MgCO_3$, $Mg_3(PO_4)_2$, $Zn(OH)_2$, $Zn_3(PO_4)_2$, and $Ca_3(PO_4)_2$, show much lower solubility in water and may be difficult to clear from the implantation site. However, they may show good biocompatibility, especially in bone tissues. For instance, $MgCO_3$ is used as a component for bioglass; $Mg_3(PO_4)_2$ and $Ca_3(PO_4)_2$ are used for bone cement; and $Zn_3(PO_4)_2$ is used as dietary supplements [3,60]. According to the work of Zhang et al. [26], some plate-like crystals and floc were observed on the surface of pure iron after immersion in Hank's solution for four weeks. Combined with the XRD and XPS result, it was found that the plate-like crystals were mainly composed of $Ca_3(PO_4)_2$ and $Fe_3(PO_4)_2{\cdot}8H_2O$ while the floc was mainly composed of $Mg_3(PO_4)_2$, $Ca_3(PO_4)_2$ and $Fe_3(PO_4)_2{\cdot}8H_2O$.

The detached particles from the BM matrix may include pure metal/alloy matrix particles and intermetallic phases. Theoretically, a pure metal/alloy particle could continue degrading and even show a faster degradation rate since it has a higher specific surface area. However, the degradability and the biocompatibility of the intermetallic phase particle still need further examination with a long-term study. This point should be considered for the future material design of the BM.

1.6. Analytical methods of the degradation rate in vivo *and* in vitro

1.6.1. Analytical methods of the degradation rate in vitro

The *in vitro* degradation/corrosion tests are simple and useful to predict the degradation behavior of the BMs. They are particularly helpful for material screening, quality control, and the study of degradation mechanisms. The common techniques in determining the *in vitro* corrosion rate are the electrochemical method and the immersion test. Corrosion is an electrochemical process, which describes the electron flow between anode and cathode. The electron flow represents the rate of the oxidation and reduction reactions at the BM/electrolyte interface, thus monitoring the electron flow provides the capability for assessing the kinetics of the corrosion process. The two methods, potentiodynamic polarization and impedance measurement, are usually adopted to determine the corrosion rates of BM. The corrosion current density i_{corr} can be estimated from the Tafel exploration in the potentiodynamic polarization curves and can also be calculated from the polarization resistance obtained from impedance measurements using Stern–Geary equation. The corrosion rate can be calculated following Eq. (5):

$$CR = K_1 \frac{i_{corr} W}{n\rho} \tag{5}$$

where CR refers to the degradation rate, $K_1 = 3.27 \times 10^{-3}$ mm g μA^{-1} cm^{-1} yr^{-1}, i_{corr} represents the corrosion current density, ρ stands for the density of the metal, and W and n refer to the atomic weight of the element and the valance of the element, respectively. However, the corrosion rate of Mg-based BMs obtained from the electrochemical methods may be unreliable due to the negative difference effect (NDE).

Several parameters are also needed for the immersion test. Both the weight loss of the BMs and the amount of metal ions released into the solution can be measured during the test. The corrosion rate of the BMs is calculated as Eq. (6) [61]:

$$CR = \frac{W}{At\rho} \tag{6}$$

where CR refers to the corrosion rate, W the calculated weight loss of the sample, A the exposure area, and t the immersion time, ρ is the standard density. For Mg-based BMs, samples are usually cleaned with chromate acid (180–200 g/l CrO_3) for 5–10 min to remove any corrosion products before measuring the final weight [62]. Chromate acid reacts with the corrosion products without damaging the Mg substrate. The corrosion products of Fe-based BMs samples could be removed by the solution (dissolving 20 g antimony trioxide (Sb_2O_3) and 50 g stannous chloride ($SnCl_2$) into 1000 mL hydrochloric acid (HCl, sp gr 1.19)) for 1 to 25 min [63].

The hydrogen volume generated from Mg-based BMs can also be used to calculate the amount of degraded Mg-based BMs, which is particularly useful when measuring the corrosion rate of Mg-based BMs. This technique allows the study of variation in degradation rates with respect to exposure time.

For Fe-based BMs, the degradation rate that tested in dynamic corrosion system should be more meaningful, especially for mimicking the situation within blood vessels. The dissolved oxygen and shear stress have a strong influence on the corrosion process, therefore self-made *in vitro* dynamic corrosion testing systems have been set up [43,45] with controllable attachments to adjust these factors.

1.6.2. Analytical methods of the degradation rate in vivo

A standard technique of the *in vivo* degradation rate of the implanted BM can be determined by the mass loss measurement of the retrieved BM sample. However, the tested animals have to be sacrificed first prior to retrieving the sample. The following cleaning and weighting steps may damage the implant/tissue interface and affect the accuracy of the results. Micro-CT is a non-destructive method that is more popularly used when determining the *in vivo* degradation of BM by characterizing the deep-frozen explanted sample in their biological environment as well as *in situ* conditions. The corrosion rate depends on the volume reduction of the BM [61,64]:

$$CR = \frac{\Delta V}{At} \tag{7}$$

where ΔV is the volume loss, A is the implant surface area, and t is the implantation time.

2. Pathophysiology and toxicology of metal elements used for biodegradable metals

As discussed in Section 1.5, the released metallic ions may induce systemic toxicity to the human body as well as local toxicity

Table 2
The summary of the pathophysiology and toxicology of Mg, Fe and the common used alloying elements [53,60,65,66].

Element	Human amount	Blood serum level	Pathophysiology	Toxicology	Daily allowance	Bone cell[d]	Vascular cell[d]
Essential nutrients							
Mg	25 g	0.73–1.06 mM	Activator of many enzymes; co-regulator of protein synthesis and muscle contraction; stabilizer of DNA and RNA	Excessive Mg leads to nausea	0.7 g	+	+
Fe	4–5 g	5.0–17.6 g/l	Component of several metalloproteins; be crucial in vital biochemical activities, i.e. oxygen sensing and transport	Iron toxicity gives rise to lesions in the gastrointestinal tract, shock and liver damage	10–20 mg	+–	+–
Ca	1100 g	0.919–0.993 mM	More than 99% has a structure function in the skeleton; the solution Ca has a signal function, including muscle contraction, blood clotting, cell function, etc.	Inhibit the intestinal absorption of other essential minerals	0.8 g	+	+
Zn	2 g	12.4–17.4 μM	Trace element; appears in all enzyme classes; most Zn appears in muscle	Neurotoxic and hinder bone development at higher concentration	15 mg	–	–
Mn	12 mg	<0.8 μg/l	Trace element; activator of enzyme; Mn deficiency is related to osteoporosis, diabetes mellitus, atherosclerosis	Excessive Mn results in neurotoxicity	4 mg	–	–
Potential essential metal							
Sr	0.3 g	0.17mg[a]	99% is located in bone; show dose dependent metabolic effect on bone; low doses stimulated new bone formation	High doses induce skeletal abnormalities	2 mg	+	+
Si	–	–	Cross linking agent of connective tissue; necessary for growth an bone calcification	Silica and silicate caused lung diseases	–		
Sn	30 mg	–	Tin-deficient diets in rat studies resulted in poor growth, reduced feeding efficiency, hearing loss, and bilateral (male) hair loss	Some organic compounds are poison, i.e. methyl and ethyl compounds	–	+–	+–
Other element							
Li	–	2–4 ng/g	Used in the treatment of manic-depressive psychoses	Plasma concentration of 2 mM is associated with reduced kidney function and neurotoxicity, 4 mM maybe fatal	0.1g[b]	+	+
Al	<300 mg	2.1–4.8 μg/l	–	Primarily accumulated in bone and nervous system; implicated Al in the pathogenesis of Alzheimer's disease	–	+	+
Zr	<250 mg		Probably excreted in feces; low systematic toxicity to animals	High concentration in liver and gall bladder	3.5 mg	+	+
Y and lanthanides		<47 μg[c]	Substituted for Ca^{2+} and matters when the metal ion at the active site; compound of drugs for treatment of cancer	Basic lanthanides deposited in liver; more acidic and smaller cations deposited in bone	–	+–	+–

[a] Sr concentration in total blood [60].
[b] The therapeutic dose for lithium carbonate is up to about 0.1 g/d in divided doses [60].
[c] The concentrations for Y and lanthanides (La, Ce, Nd, Sm, Eu, Gd, Tb, Dy, Ho, Er, Tm and Yb) are below 0.1, 0.44, 0.03, 0.07, 0.2, 0.1, 0.09, 0.1, 0.2, 0.03, 0.1 and 0.1 mg/l, respectively [60].
[d] The toxicity levels for bone- and vascular-related cells are according to the cytotoxicity test of the metal salts [52,67,68]; (+) stands for the mild toxicity, (+–) stands for the moderate toxicity, and (–) stands for the severe toxicity.

to the peri-implant cells. From the systemic toxicity point of view, the choice of alloying elements is critical in order to control the release of toxic metallic elements. Table 2 summarizes in three categories the pathophysiology and toxicology of Mg and Fe as well as commonly used alloying elements for Mg and Fe based BM: essential nutrient, potential essential metals, and the other common alloying elements. The body can even tolerate a toxic element at a low concentration below its threshold while a nutrient element can have an adverse effect at an excessive concentration. Thus, the amount of the alloying elements added into BMs needs to be carefully investigated with respect to the degradation rate and the physiological environment at the implantation site. Moreover, it is a key issue how to control the local concentration of the released metal ions below their permitted concentration levels for the design of the final BM medical devices since the concentration of the released metal ions at a certain position of the tissue around the implants varies with tissue reconstruction procedures of the host as a function of time, space (the distance to the BM implant) and local microenvironment (e.g. the local blood supply, which influences the diffusion and transfer of the released metal ions).

Furthermore, as a consequence of the biological effect of the released metal ions, they will have a more direct effect on the viability of local cells and tissues adjacent to the BM implants. Effects of the metallic cations on bone- and vascular-related cells are summarized in Table 2. Li^{+}, Al^{3+}, Mg^{2+}, Ca^{2+}, Sr^{2+} and Zr^{4+} reduce cell viability of bone-related (MG63 and MC3T3-E1) and vascular-related cells (human umbilical cord perivascular cells, HUCPV) at concentrations over 1000 μM indicating mild toxicity [52,67,68]. The IC_{50} values of Fe^{2+}, Fe^{3+} and Y^{3+} range between100 and

1000 μM showing moderate toxicity [52,68]. As for the element Sn, Sn^{4+} exhibits higher toxicity than Sn^{2+}. Notably, the IC_{50} values of Zn^{2+} and Mn^{2+} to MG63 and MC3T3-E1 osteoblast are in the range of 10–100 μM [52] and suggest the highest toxicity, although both elements are essential to humans. Loos et al. [69] also reported the negative effect of the alloying elements Zn and Mn with Mg, as evidenced by the reduction of viability and proliferation of endothelial cells (EC) and smooth muscle cells (SMC). Rare earth elements (REEs) belong to a class of elements that are often added into Mg alloys in the state of the mischmetal and show moderate toxicity to bone- and vascular-related cells. As reported, La^{3+} and Ce^{3+} inhibited the MG63, HUCPV, and macrophage cell line RAW264.7 at a low concentration of 30–500 μM, while Gd and Dy revealed the least toxicity with initial inhibitory concentration (IIC) of 2000 μM [67]. Besides the ionic cytotoxicity test using the metal salts, several alloying elements were screened by investigating the cytotoxicity of binary Mg–X alloys, adding 1 wt.% of alloying element for each alloy [70–72]. Results showed that the extracts from Mg–X alloy (X = Ca, Sr, Al, Si, Zn, Zr) did not significantly reduce the viability of fibroblasts (L929 and NIH3T3) and osteoblasts MC3T3-E1, but cytotoxicity was observed when Sn, Mn, and Y were added as the alloying elements. Mg–1Mn also revealed severe toxicity to human umbilical vein endothelial cells (ECV304) and vascular smooth muscle cells (VSMCs). These results coincided well with other investigations studying the cytotoxicity of metallic elements using metal salts.

As discussed above, the conventional cytotoxicity test could provide an initial indication of biocompatibility of metal cations while the genetic regulation test could provide a more accurate result and is also crucial in predicting the biocompatibility of alloying elements. In the case of vascular applications, Drynda et al. [73] found a significant up-regulation of inflammatory genes (IL-6, IL-8, and ICAM-1 genes) by the presence of Ce, Nd, Y, and Yb ions at a concentration of 50 μg/ml after culturing with smooth muscle cells (SMCs) for 24 h. It was reported that 0.03 mg/ml of Fe(II)-gluconatedihydrate reduced the amount of mRNA from genes that regulate the proliferation in SMCs and, thus, reduce the proliferation of VSMCs [74]. Therefore, the release of Fe^{2+} may help to control restenosis *in vivo*.

In the study of gene expression profile in which exposing mouse 3T3 fibroblasts to the degradation products of Fe–35Mn (wt.%), Purnama et al. [75] showed that the exposure to 3.25 mg/ml of Fe–35Mn powder up-regulated 75 genes and down-regulated 59 genes whilst up-regulation of 126 genes and down-regulation of 76 genes were observed in the presence of 0.25 mg/ml Mn powder. There were no genes found to be regulated by 5 mg/ml of Fe powder. Comparing the gene expression profile of 3T3 fibroblasts in the presence of Fe–35Mn and Mn, 68 up-regulated and 54 down-regulated genes were common. Among these genes, Caveolin-1 (cav1), the structural protein of caveolae (small and smooth plasma membrane invaginations present in various differentiated cell types) was one of the most down-regulated genes in the gene expression profiles [76]. Further studies indicated that cav1 gene expression was not influenced by exposure to ferrous ions while exposure to Mn for 24 h reduced cav1 gene expression by about 30% and >65% after 48 h compared with the control or 3T3 cells. Similar pattern were also observed in cav3 gene expression and, therefore, Purnama et al. [76] concluded that caveolins could be a potential biomarker to measure the cytotoxicity of alloying elements. For orthopedic applications, Mn and Fe were found to induce significant release of IL-6 at a concentration of 1 mM when cultured with MG63 osteoblasts [68].

When designing a BM, its composition is not only driven by the toxicology of the metallic elements but also the materials' performances, including the mechanical properties and degradation behavior, with respect to the specific implantation sites and therapeutic purposes. Notably, the degradation behavior is associated with local biocompatibility of the BM implants because of the releasing profile of the degradation products. If the BM degrades too fast, rapidly elevated pH value can cause toxicity in peri-implant cells and local tissues with a concomitant increase in the inflammatory response. Although Mg-based and Fe-based BMs have shown favorable results on animal models in terms of biocompatibility and inflammatory response, gas cavities have often been observed within bones as consequences of the rapidly degraded Mg-based BMs [70,77–79], as well as severe hemolysis due to the dramatic increase of pH values.

In the following Sections 3–5 we review the microstructure, mechanical properties, degradation behavior, and *in vitro* and *in vivo* biocompatibilities of each type of BM individually (Mg and its alloys, Fe and its alloys, Zn and its alloys, pure W, Ca-based bulk metallic glasses, Sr-based bulk metallic glass, and Zn-based metallic glasses), based on their alloying systems. Thereafter, Section 6 examines the fabrication of BM raw materials (wire, tube, and plate) and the design and process (machining, cutting, polishing and sterilization) of BM medical devices for the usage within bone and blood vessels; Section 7 discusses the challenge and future R&D directions for the commercialization of BM medical devices; and Fig. 2 schematically illustrates the link among Sections 3–7 in order to give the reader an overview.

3. Magnesium-based biodegradable metals

Mg and its alloys have been widely investigated and well accepted for automobile and aerospace applications. Commercial Mg alloys were originally designed for industrial usage, which potentially contain toxic elements (e.g. Al, RE, etc.) and are not suitable for biomedical applications. As a result, new kinds of Mg-based BMs with the latest alloying system (different from the existing industrial Mg alloy family), novel structure, and modified surfaces have been specially developed. Hundreds of publications are available to date regarding the characterization of the microstructures, testing of the mechanical properties, degradation behavior and ion release, and *in vitro* and *in vivo* biocompatibility studies to evaluate the feasibility of these Mg-based BMs for biomedical purposes. This section is subdivided into four parts: (1) pure Mg and new Mg alloying systems, including alloying with essential elements (Mg–Ca, Mg–Sr, Mg–Zn, and Mg–Si) or low toxic elements (Mg–Sn and Mg–Zr), and the modification of industrial Mg alloy systems (Mg–RE and Mg–Al); (2) novel structured Mg-based BMs (porous, composited, nanocrystalline, and glassy structures); (3) surface modification methods of the Mg-based BMs to adjust the degradation rate; (4) results of animal testing and clinical trial from the above-mentioned Mg-based BMs.

3.1. Development of Mg-based biodegradable metals

3.1.1. Pure Mg

Mg by itself is considered to be relatively safe. Hence, without the concern of releasing other alloying elements pure Mg seems attractive for medical use. However, the presence of impurities (iron, nickel, and copper) in Mg is unavoidable and dramatically accelerates its corrosion, which is observed when the amount of impurities exceeds the tolerance limit (0.005 wt.% for Fe and Ni, 0.05 wt.% for Cu). Qiao et al. [80] reported the degradation of high purity (HP) Mg was accelerated 3–60 times when the Fe concentration increased to 26–48 ppm. Song [81] found that high purity Mg (~0.0045 wt.% Fe, <0.002 wt.% Cu and <0.002 wt.% Ni) has the corrosion rate of a thousand-fold less when compared to the commercially pure (CP) Mg (0.02 wt.% Fe, <0.002 wt.% Cu, and <0.002 wt.% Ni) in Hank's solution. Unfortunately, relative low strength is observed for pure Mg even after processing (the yield

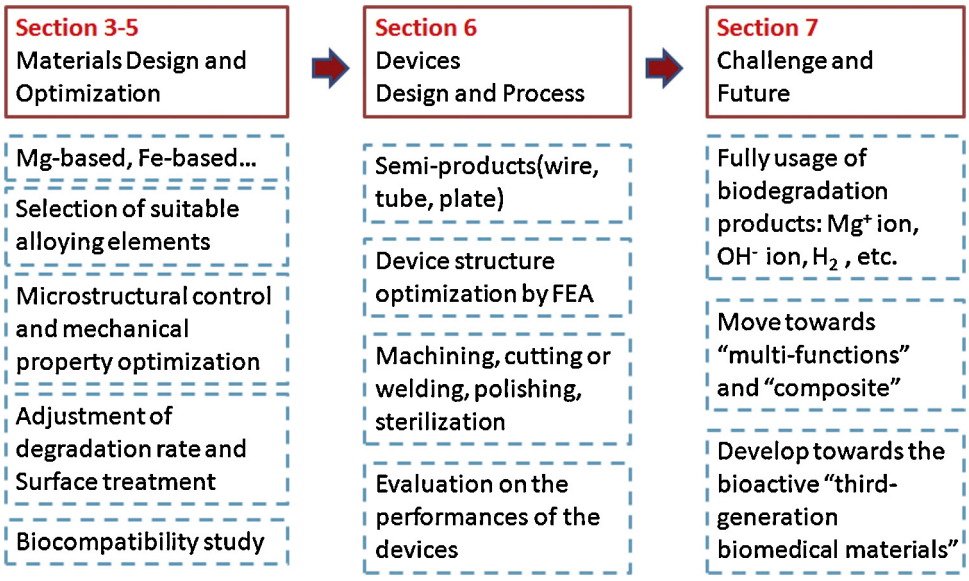

Fig. 2. Schematic diagram to illustrate the links among Sections 3–7.

tensile strength is 21 MPa for as-cast Mg, 90–105 MPa for as-extruded Mg, and 115–140 MPa for as-rolled Mg [82]), so further improvement is needed for load bearing biomedical applications. Therefore, several low toxic alloying elements have been added to develop Mg–X alloy systems (X = alloying element) and investigated for their mechanical and degradation properties.

3.1.2. Mg–Ca and Mg–Sr based alloy systems

Ca and Sr belong to group 2 of the periodic table and share similar chemical and metallurgical properties. The solubility of Ca and Sr in Mg is relatively limited, about 1.34 wt.% and 0.11 wt.% respectively under equilibrium conditions. Incorporation of supersaturated Ca and Sr into Mg leads to precipitation of Mg_2Ca and $Mg_{17}Sr_2$ phases along the grain boundaries. Alloying elements Ca and Sr can refine the microstructure of Mg and improve the strength and creep properties under elevated temperatures due to the formation of thermally stable intermetallic phases. However, these intermetallic phases are brittle, which can act as potential sources for cracking to occur and indicates a negative effect on the ductility of Mg, and also accelerates the degradation due to galvanic corrosion.

Fig. 3 summarizes the relationship between ultimate tensile strength, elongation, and degradation with the amount of alloying elements in various as-cast Mg–X alloys. It can be seen that as the alloying Ca element increases in the range of 1–3 wt.%, the tensile strength and elongation of the as-cast Mg–Ca alloys are reduced [70]. Wan et al. [83] reported a 0.6 wt.% of Ca addition could improve the bending and compressive strength of pure Mg while a higher Ca addition deteriorated these properties. Taking the degradation behaviors of the alloys (Fig. 3(c)) into consideration, the appropriate Ca content should be in the range of 0.6–1 wt.% [70,83–85]. Furthermore, Zn, Y, and Sr were introduced in the Mg–Ca binary alloys to optimize their mechanical and degradation properties [86–88]. The introduction of Zn (2.31 wt.%) into the as-cast Mg–3Ca alloy could improve the strength and ductility of the alloy, and its presence supports the formation of the eutectic phase (α-Mg + Mg_2Ca + $Ca_2Mg_6Zn_3$) that leads to a decreased degradation rate of the alloy [86]. The addition of Y (1 wt.%) negatively impacted the compressive strength, corrosion resistance, and biocompatibility of the as-cast Mg–1Ca alloy whilst an improvement in ductility was observed [87]. Berglund et al. [88] designed a series of Mg–xCa–ySr alloys (x = 0.5–7.0 wt.%; y = 0.5–3.5 wt.%), and found that the Mg–1Ca–0.5Sr alloy exhibited the slowest degradation rate (~1.5 mm/yr in Hank's solution) but still maintained appropriate compressive strength (274 ± 4 MPa).

For the binary Mg–Sr alloys, an increase in strength and reduction in elongation are observed, up to 3 wt.% in the as-cast state, when increasing the amount of Sr but higher than 3 wt.% of Sr addition negatively impacts the alloys (Fig. 3(a) and (b)) [89,90]. In addition, the increasing Sr content deteriorates the corrosion resistance of the as-cast Mg–Sr alloys (Fig. 3(c)) [89–91] whilst Gu et al. [71] reported that the as-rolled Mg–2 wt.% Sr alloy exhibited the highest ultimate tensile strength and the slowest degradation rate among experimental as-rolled Mg–Sr alloys with Sr content ranging 1–4 wt.%. Consequently, it is recommended to lower the contents of alloying elements Ca (<1 wt.%) and Sr (<2 wt.%) to improve mechanical and degradation properties of biomedical Mg-based BMs.

3.1.3. Mg–Zn based alloy systems

Zn is an important alloying element with a relatively high solubility in Mg (6.2 wt.%). It contributes to the mechanical properties of the alloy because of its solid solution strengthening and aging strengthening effect. As reported, the ultimate tensile strength and elongation of as-cast Mg–Zn alloys significantly increased with increasing Zn contents up to 4 wt.%, but any higher percentage of Zn would lead to reduction of both properties [92] (Fig. 3(a) and (b)) and decrease the corrosion resistance of the alloy [92] (Fig. 3(c)).

Taking both the mechanical and degradation properties as main concerns, the Mg–Zn alloys with low Zn content (<4 wt.%) were further alloyed by adding third alloying elements, including Ca [92,93], Mn [94], Sr [89], Y [95], and Zr [96]. The introduction of Ca, Sr, and Y refined the microstructures while contributing little to the mechanical properties of the Mg–2Zn alloy [89,92,93,95]. Mn and Zr additions effectively improved the strength of Mg–Zn alloys. For instance, the as-cast Mg–2Zn–0.2Zr alloy exhibited much higher tensile property (UTS = 186.9 MPa, Elong. = 18%) than that of as-cast Mg–2Zn alloy (UTS = 145.9 MPa, Elong. = 12.2%). The degradation behaviors of the Mg–Zn alloys were also explored. Low contents of Ca, Mn, and Sr were found to slow down the degradation rate [89,92–94]. Zhang et al. [92,93] found that 0.2 wt.% Ca addition could reduce approximately one third of the degradation rate of as-cast Mg–4Zn alloy and that the degradation

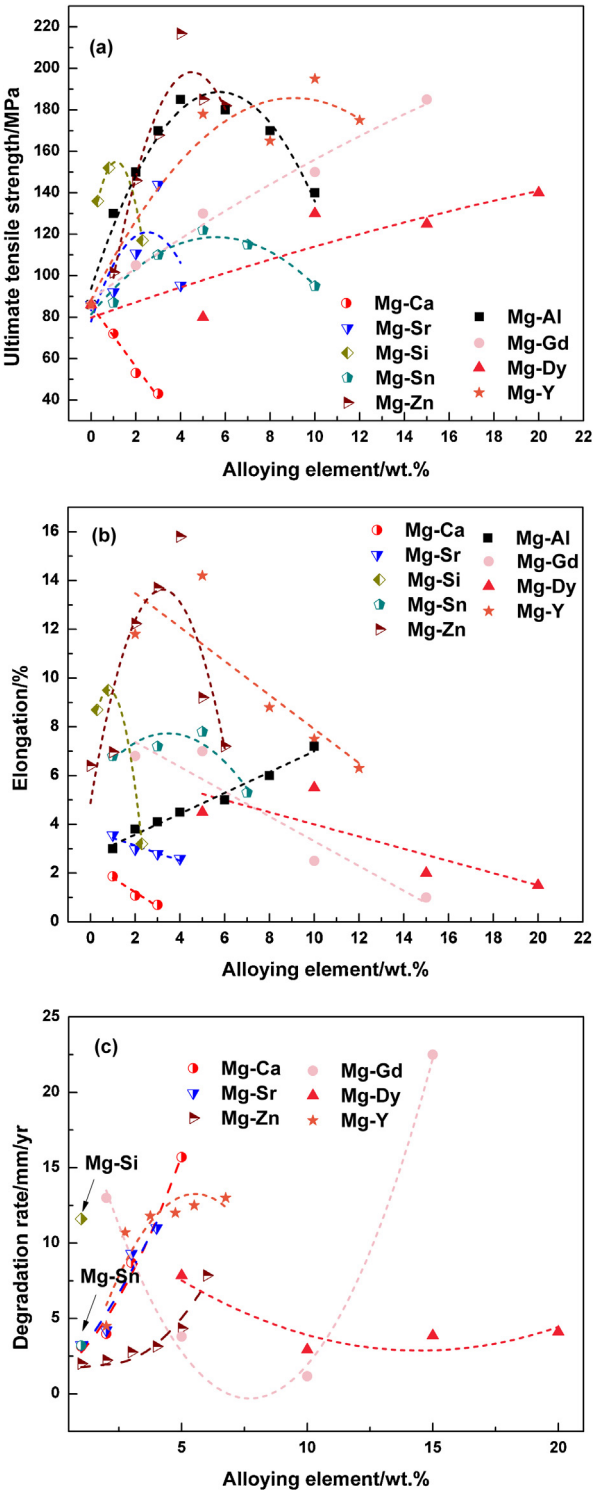

Fig. 3. Summary of (a) ultimate tensile strength, (b) elongation and (c) degradation rates for binary Mg–X alloys in the as-cast state as a function of alloying element content. The dotted lines in figure (a) and (b) are added for easier recognition of the variation of properties.

rate of as-cast Mg–4Zn–*x*Ca alloy increased with increasing Ca content (x = 0.2–2 wt.%).

3.1.4. Mg–Si based alloy systems

Si exhibits nearly no solid solubility in Mg. It reacts with Mg and precipitates as an intermetallic compound of Mg_2Si. The *in situ* precipitation of the Mg_2Si phase can effectively strengthen the Mg alloys due to its high melting temperature, low density, high hardness, and low thermal expansion coefficient. Gu et al. [72] reported that Si is the most effective alloying element to improve the yield strength (YS) and ultimate tensile strength (UTS) of the pure Mg than the alloying elements Al, Ag, In, Mn, Sn, Y, Zn, and Zr. The YS, UTS, and elongation of the as-cast Mg–1 wt.% Si alloy are 80 ± 0.6 MPa, 193.77 ± 2.03 MPa and 14.83 ± 0.29%, respectively. As summarized in Fig. 3(a) and (b), the optimal Si content is around 0.8 wt.% resulting in the highest ultimate tensile strength and elongation [97]. However, the Mg_2Si phase presents Volta potential difference relative to the α-Mg matrix and accelerates the degradation rate dramatically. As-cast Mg–1Si alloy showed nearly three times faster degradation rate than that of the as-cast pure Mg in Hank's solution [72]. Zhang et al. [98] introduced Ca and Zn into Mg_2Si as a means to refine and modify its morphology thereby improving the corrosion resistance and the mechanical properties of Mg–Si alloys. With the addition of Ca, the eutectic structure of the Mg_2Si phase turned into a needle-like structure. Adding 0.4 wt.% of Ca into Mg–0.6 wt.% Si alloy did not benefit its mechanical property but reduced its degradation rate to over 50%. The addition of 1.5 wt.% Zn to Mg–0.6 wt.% Si alloy could obviously modify the morphology of the Mg_2Si phase from a coarse eutectic structure to a small dot or short bar shape. As a result, the tensile strength, elongation, and corrosion resistance of the resulting Mg alloys were improved significantly [98].

3.1.5. Mg–Sn based alloy systems

As shown in Fig. 3(a) and (b), the UTS and elongation of the as-cast Mg–Sn alloys increases with up to 5 wt.% of Sn, yet adding any higher quantities of Sn deteriorates its strength and ductility [99]. Adding the third alloying element Ca could refine the dendritic microstructure of the Mg–5 wt.% alloy and suppress the formation of Mg_2Sn thus resulting in the increased shear strength and creep resistance of the Mg–5Sn alloy [100]. Gu et al. [72] found that the as-cast Mg–1 wt.% Sn alloy exhibited higher YS, tensile strength, and elongation than as-cast pure Mg while it showed decreased elongation after hot rolling. Yang et al. [101] designed a series of Mg–Sn–Mn alloys (Sn 1.0–3.0 wt.% and Mn 0.5–1 wt.%) for stent use among which the as-rolled Mg–3Sn–0.5Mn showed the best combination of mechanical performance and corrosion resistance.

3.1.6. Mg–Zr based alloy systems

Zirconium (Zr) is known as a powerful grain refiner for Mg alloys. This element is usually used in alloys containing Zn, RE, Y, and thorium (Th) and cannot be used together with Al and Mn since they form stable compounds with Zr [82]. Recently, the Mg–Zr alloys have attracted considerable attention due to their high specific damping capacity (~80%), which may help to suppress the vibrations generated during movement and stress at the implant/bone interface [102]. Gu et al. [72] indicated that 1 wt.% of Zr addition in Mg resulted in significant improvement of the strength and ductility of the metal, exhibiting UTS of 171.87 ± 2.31 MPa and elongation of 27 ± 2%, and reduced the degradation rate by 50%. Zhou et al. [103] fabricated the ternary Mg–Zr–Ca alloys that exhibited increasing tensile strength and elongation when Zr content increased from 0.5 wt.% to 1 wt.%. The as-cast Mg–1Zr–1Ca alloy indicated approximately 125 MPa in ultimate tensile strength and 8% in elongation to failure. The co-addition of Sr and Sn could effectively reduce the degradation of as-cast Mg–Zr–Ca alloy [104]. In addition, the as-cast Mg–Zr–Sr alloys with a wide range of Zr content 1–5 wt.% were investigated [105], among which the degradation rate increased with increasing Zr content and the Mg–1Zr–2Sr alloy exhibited the lowest degradation rate in SBF. In general, the alloying amount of element Zr should be lower than 1 wt.% for biomedical Mg-based BMs [106].

3.1.7. Mg–Al based alloy systems

Aluminum (Al) is the most commonly used alloying element for Mg alloys with a maximum solubility of 12.7 wt.% in Mg. Several Mg–Al based alloy systems have been developed for industrial applications, such as AZ and AM alloy systems, and are usually used as material models to study the corrosion mechanism of Mg alloys. As summarized in Fig. 3(a) and (b), increasing amounts of Al up to 6 wt.% improves the UTS of binary Mg–Al alloy but any higher amount reduces the alloy strength. The alloy elongation increases with increasing Al content (Fig. 3(b)). In addition, the presence of Al improves the corrosion resistance of an Mg alloy by forming Al_2O_3 film on the alloy surface. Wen et al. [107] indicated that the degradation rate of AZ31, AZ61, and AZ91D alloys was relatively high (3–8 mm/yr) in the first 24 h immersion period in m-SBF and slowed down with a prolonged immersion period up to 24 d in an order of AZ91D (1.23 mm/yr) < AZ61 (1.32 mm/yr) < AZ31 (2 mm/yr). In this *in vitro* experiment, the AZ91D alloy exhibited relatively uniform corrosion morphology with a few shallow pits, while obvious corrosion pits were seen on the surface of AZ31 and AZ61 [107]. In contrast, severe pitting was observed on AZ91D when implanted *in vivo* [108]. However, considering the neurotoxicity of element Al, Mg–Al-based alloys are not recommended candidates for biomedical applications in humans.

3.1.8. Mg–Y and Mg–REE based alloy systems

Rare earth elements (REEs) usually alloy with Mg to improve its high temperature strength and creep resistance. They are frequently added as mischmetal (mainly Ce, La, and Nd) or didymium (85% Nd and 15% Pr). The Y and seventeen other rare earth elements (REEs) can be divided into two groups considering their solid solubility in Mg: high solid solubility group (Y, Gd, Tb, Dy, Ho, Er, Tm, Yb, and Lu) and limited solubility group (Nd, La, Ce, Pr, Sm, and Eu). Generally, the Mg–RE alloy system is suitable for heat treatment because of the temperature dependent solid solubility variation of REEs in Mg.

Ce, La, and Nd are the most commonly used REEs in Mg–REE alloys. Given their relative low solid solubility in Mg (0.23 wt.% for La, 0.74 wt.% for Ce and 3.6 wt.% for Nd), the intermetallic phases would easily precipitate and result in galvanic corrosion. Birblis et al. [109] found that the volume of the intermetallic phase increased with increasing REEs content (ranging in 0–5 wt.%) in high-pressure die-cast binary Mg–REE alloys, resulting in the accelerated degradation in 0.1 M NaCl because of galvanic corrosion. Mg–REE alloys exhibited corrosion current densities of 20 $\mu A/cm^2$ for 3.53 wt.% of Nd addition, 30 $\mu A/cm^2$ for 5.07 wt.% of La addition and 60 $\mu A/cm^2$ for 4.76 wt.% of added Ce compared to approximately 10 $\mu A/cm^2$ for commercially pure Mg. After T4 heat treatment, the WE54 alloy exhibited a slower degradation rate whereas the degradation rate increased after T6 heat treatment, which was mainly attributed to the intermetallic precipitation during the aging treatment [110,111]. The Mg–Nd–Zn–Zr alloy with the nominal composition of 2.0–4.0 wt.% Nd, 0.1–0.5 wt.% Zn, and 0.3–0.6 wt.% Zr was designed for medical use, which exhibited good mechanical properties after extrusion and the subsequent cyclic extrusion and compression (approximately 300 MPa in UTS and 30% in elongation) [112]. T5 treatment could improve the strength and corrosion resistance of the Mg–Nd–Zn–Zr alloy while slightly deteriorating the ductility [113].

The alloying elements with high solid solubility in Mg at eutectic temperatures (11.4 wt.% for Y, 25.3 wt.% for Dy and 23.49 wt.% for Gd) were selected for biomedical Mg alloy designs to avoid the formation of intermetallic phases and the resulted galvanic coupling formation. The mechanical and degradation properties of Mg can be tailored over a wide range by the addition of a single REE (Fig. 3). The solid solubility of REEs changed greatly with respect to the temperature and, thus, the subsequent heat treatment will also contribute to the adjustment of the Mg–REE alloy behavior. Generally, the increasing amount of added elements Y, Dy and Gd resulted in improved alloy strength and weakened ductility (Fig. 3(a) and (b)). The degradation rate of binary Mg–Y, Mg–Dy, and Mg–Gd all depend on the concentration of each alloyed element with the optimal addition amount being 2 wt.% for Y, 10 wt.% for Dy, and 15 wt.% for Gd (Fig. 3(c)) [114–116]. In addition, the YS and UTS of Mg–(5–15 wt.%)Dy alloys decreased after the T4 treatment while the degradation rate dramatically slowed down (i.e. the degradation rate of Mg–5 wt.% Dy alloy decreased from about 7.9 mm/yr to 0.5 mm/yr [116]). In contrast, a higher degradation rate was observed after the aging treatment at 200 °C as well as an increased strength and lower ductility for Mg–Dy alloys [116]. Liu et al. [115] indicated that the binary Mg–Y alloys exhibited increased degradation rates in 0.1 M NaCl with increasing Y content ranging from 0 to 7 wt.% while decreased degradation rates were observed in 0.1 M Na_2SO_4 solution when Y content was higher than 3 wt.% (Fig. 3(c)).

3.2. Novel structure design for Mg-based biodegradable metals

3.2.1. Porous structure

Porous scaffold is a key component in tissue engineering for bone regeneration, which allows tissue ingrowth, prevents implant loosening, permits the transportation of body fluid, and also shows the potential to serve as a platform for drug delivery [117]. Generally, the powder metallurgy (P/M) technique, the pressing of a mixture of metal powders with removable spacer (i.e. Carbamide) particles, is one of the most commonly used methods to prepare the porous Mg alloys. A following sintering step burns out the spacer particles to obtain the porous structure; the porosity and pore size are adjustable by the content and size of the adopted spacer particles [118–120].

Another approach to obtain the porous Mg scaffold is by the negative salt-pattern molding process. An open porous AZ91 alloy scaffold was produced, with the porosity ranging from 72 to 76% and pore size varying between 10 and 1000 μm (Fig. 4(a)), by infiltrating the molten Mg into a NaCl preform and then washing out the salt preform in a NaOH solution, as reported by Witte et al. [78,79]. Staiger et al. [121] further improved this negative salt-pattern molding process to fabricate a specially designed porous Mg scaffold. Porous Mg was accurately architected first by the computer-aided design (CAD) and then by printing a positive polymeric 3D template. The 3D template was used to create the negative salt template by salt infiltration followed by sintering to remove the polymer. In the third step, the liquid Mg melt mold was infiltrated under pressure and the porous Mg scaffold was obtained after removing of the salt (Fig. 4(b)). This technique showed highly accuracy (5–12% error) with macroscopic features as fine as 0.8 mm.

In addition, the pore size and porosity of the porous Mg scaffolds could also be accurately controlled by the laser perforation technique (Fig. 4(c)), as reported by Geng et al. [122]. Gu et al. [123] fabricated a lotus-type porous pure Mg using a metal/gas eutectic unidirectional solidification method (GASAR process) (Fig. 4(d)), which exhibited slower decay even when compressive yield strength was applied during immersion in SBF.

Numerous publications have shown that reduction in mechanical properties and increments of degradation rates of the porous Mg scaffold are usually observed as the porosity and pore size increase, regardless of the technique that was adopted. For instance, a study by Wen et al. [119] found the strength and elastic modulus of P/M porous Mg scaffolds decreased with increasing porosity (35–55%) and pore size (70–400 μm) while the degradation rate increased. The compressive strength of the laser-perforated Mg scaffolds noticeably dropped when the porosity increased from 42.6% to 50.34% [122].

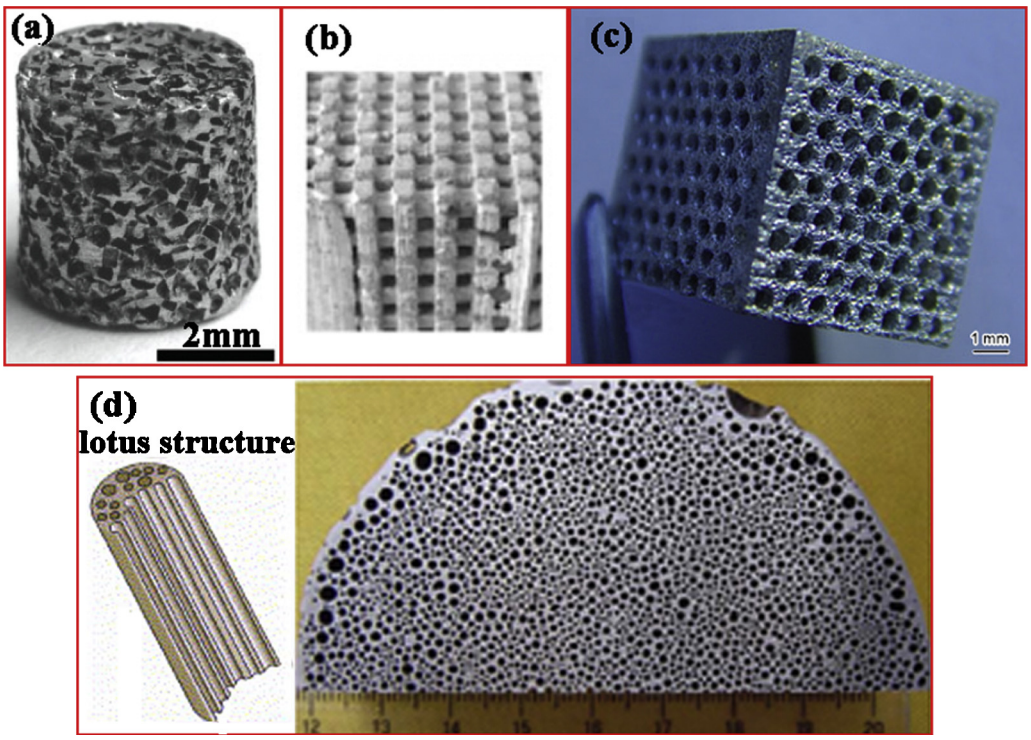

Fig. 4. (a) AZ91D scaffold prepared using NaCl as spacer [78,79]; (b) Mg scaffold designed by CAD and the following negative pattern molding [121]; (c) honeycomb-structured magnesium scaffolds fabricated by laser perforation technique [122]; (d) lotus-type porous pure magnesium prepared by metal/gas eutectic unidirectional solidification method [123].

3.2.2. Composite structure

Mg metal matrix composites (MMCs) exhibit adjustable mechanical and corrosion properties as determined by the selection of the reinforcement material. The content, distribution, and size of the reinforcements are of major importance for mechanical and degradation properties of Mg MMCs. Various reinforcements were adopted to prepare Mg MMCs, such as calcium phosphate-based ceramic [124–131], bioactive glass (BG) [132], zinc oxide [133], and calcium particles [134], through powder-metallurgical routes (P/M) and stirring casting methods.

(1) P/M method: Several authors adopted a conventional blend-press-sinter route to prepare the MMCs [126,133]. Lei et al. [133] prepared the P/M Mg/ZnO MMCs containing 20 wt.% of ZnO nanoparticles. The inclusion of ZnO nanoparticles improved the tensile strength, surface hardness, and corrosion resistance of the Mg matrix but showed a reduction in elongation. In addition, a dose dependent effect on the fluorapatite (FA) nanoparticles was observed for the mechanical properties of AZ91/FA MMC [126]. The compressive strength of the alloy AZ91 could be increased when adding FA nanoparticles for up to 20%; exceeding such a threshold would achieve reversed results or reduction in strength. The degradation of the AZ91/FA composite decreased with increasing FA content.

A subsequent hot extrusion process was adopted following the P/M route to improve the mechanical properties and bonding strength between the matrix and the reinforcement. Witte et al. [129] indicated that the P/M AZ91D/20 wt.% HA MMC exhibited the yield tensile strength (YTS) of 264.3 ± 10 MPa and improved corrosion resistance as well as cytocompatibility compared with those of the master AZ91D alloy. Feng et al. [124] produced the ZK60/CPP MMC incorporated of 10–30 wt.% calcium polyphosphate particles (CPP) with particle size less than 10 μm. The UTS of ZK60/CPP MMC decreased from ~280 MPa to ~200 MPa by increasing CPP content. Further study by Feng et al. [125] indicated that the mechanical properties of ZK60/CPP MMC could be improved by the selection of ultrafine CPP particles (<750 nm), demonstrating higher YTS (319.5 MPa) and elongation (30.5%) when composed with 5 wt.% of CPP particles. Gu et al. [127] reported decreased mechanical property and corrosion resistance with an increase in HA particle (2–3 μm) content for P/M Mg/HA composite.

(2) Stirring casting method: Another approach for MMCs development is to introduce the reinforcement into the melt followed by the stirring casting technique. In general, bioceramic or bioglass are selected to be the reinforcement, yet the poor wettability of the ceramic particles limits the incorporating amount as well as the dispersion of the reinforcement. Several methods have been carried out to overcome this limitation of the stirring casting method. Ye et al. [130] modified the nano HA particles with gelatin and successfully added 1 wt.% of nano HA particles into an Mg–Zn–Zr alloy melt. Huan et al. [132,135] introduced bioglass (BG) into a semi-solid ZK30 melt and cast the ZK30/BG MMCs with 0–20 wt.% of BG under high pressure. Liu et al. [131] adopted the combination of high shear and MCAST (Melt Conditioning by Advanced Shear Technology) units to disperse the β-TCP particles or break up the agglomerates in the Mg–3Zn–Ca melt through the shear strain generated by the flow. With this technique, most particles were pushed into the last solidified region and adjacent to the eutectic $Ca_2Mg_6Zn_4$ phase. Moreover, Gu et al. [128] proposed a novel Mg–Ca alloy based composite using melt infiltration method with the HA/TCP scaffold as porous perform. This kind of composite exhibited a significantly reduced degradation rate than that of the bulk Mg–Ca alloy.

To summerize, the P/M and a subsequent extrusion process would provide the obtained MMCs with a better mechanical property. Compared with the P/M MMCs, which exhibited less than 0.5% in porosity due to the extrusion process, the semi-solid cast composite was found to be microporous, thus, indicating a more accelerated degradation than the master alloy [96]. The incorporation of calcium phosphate-based reinforcement and bioglass particles can generally improve the bioactivity of the master alloy

with accelerated depositions of calcium phosphate in simulated body fluid.

3.2.3. Ultrafine-grained structure

As discussed in Section 1.3.1, Mg alloys are highly susceptible to galvanic corrosion due to the impurity or secondary phases, which act as internal cathodes. Thus, the corrosion mechanism of Mg alloy is often observed as localized corrosion adjacent to the cathode. One strategy to minimize this effect is to refine the microstructure of Mg alloys.

Gu et al. [136] refined the grain size of the Mg–3Ca alloy to 200–500 nm by rapid solidification (RS) and the grain size decreased with increasing cooling rate. In comparison with the as-cast Mg–3Ca alloy, the Mg–3Ca alloy processed by RS exhibited dramatically reduced degradation rate from 21 mm/yr to 0.36–1.43 mm/yr (higher the RS speed, lower the degradation rate) and showed more uniform corrosion morphology on the sample surface [136]. However, Xu et al. [137] found that the RS Mg–Zn–Ca (Zn content is 6, 10, and 20 wt.% respectively with Ca content being 1 wt.%) rods revealed fine grains but had accelerated degradation than the counterpart in the as-cast state.

Furthermore, ultrafine or nanocrystalline Mg alloys can also be obtained by severe plastic deformation techniques (SPD), such as the equal channel angular pressing (ECAP), high pressure torsion (HPT), or cyclic extrusion and compression (CEC). The final grain size of the consequent Mg alloys obtained a range from less than 1 μm to several micrometers with respect to the processing parameter. Zhang et al. [112] indicated that the as-CECed Mg–Nd–Zn–Zr alloy exhibited fine grain size (~1 μm) and enormously improved tensile properties (71% and 154% higher YS and elongation than the as-extruded state). The UTS and elongation were ~300 MPa and ~30%, respectively. The degradation rate also slowed after CEC. Similarly, the ultrafine-grained Mg–Zn–Ca alloy prepared by the HPT process revealed improved corrosion resistance compared to the as-extruded ones [138]. The ultrafine-grained AZ31 alloy, prepared by the ECAP with the back pressure (BP-ECAP) method, revealed a significantly improved UTS (~380–420 MPa) and elongation (~27–35%) [139]. Gu et al. [140] found that as-ECAPed and BP-ECAPed AZ31 (grain sizes ranging from 2 to 8 μm) displayed faster degradation rates than those of the as-extruded samples (grain size ~28 μm), which may be attributed to the residual inhomogeneous large-sized grains during recrystallization [140]. Wang et al. [141] found similar fatigue and degradation performance of the as-ECAPed AZ31 in comparison with the hot-rolled samples. Compared to the extruded or hot-rolled samples, pits with smaller size and shallower depth were observed for the ultrafine-grained or nanocrystalline Mg alloys after corrosion [112,138,140]. An interesting future pursuit is the rapid solidified ribbon of Mg-RS66 that exhibits ultrafine grain size (about 1 μm) after reciprocal extrusion [142,143]. This kind of Mg alloy combines altered mechanical properties (UTS 400 MPa, Elongation 23.5%) and sufficient corrosion rates *in vivo* [144].

3.2.4. Glassy structure

Investigations were also carried out recently for Mg-based bulk metallic glasses (BMGs), because their single-phase structure and chemical homogeneity can minimize the galvanic corrosion effect. Several studies have reported the Mg–Zn–Ca BMGs synthesized by RS [57,145,146] or mechanical alloying technique [147]. The investigated Mg–Zn–Ca BMGs exhibited much higher strength but poor plasticity (2–4%) than that of the crystalline counterpart and the conventional engineered Mg alloys. For examples $Mg_{66}Zn_{30}Ca_4$ BMG shows higher compressive strength (716–854 MPa) in comparison to crystalline alloy AZ91D (400 MPa) and $Mg_{67}Zn_{28}Ca_5$ glassy wire exhibits higher tensile strength (675–894 MPa) than that of crystalline alloy WE43 (270 MPa) [57,148]. Additionally, the Mg–Zn–Ca BMGs revealed slower degradation rates and more uniform degradation modes with small and shallow pits well distributed on the surface in comparison with the crystalline pure Mg [145]. It was reported that the hydrogen evolution of the Mg_{95-x}–Zn_x–Ca_5 BMGs decreased when x ranged among 25–35 and was nearly eliminated when $x > 29$ [57,146]. The *in vivo* degradation of $Mg_{95-x}Zn_xCa_5$ BMGs correlated well with the *in vitro* hydrogen evolution test. No gas cavities were observed around the $Mg_{60}Zn_{35}Ca_5$, owing to the formation of a passivating $ZnO/ZnCO_3$ layer [57,146].

Intrinsic brittleness and/or embrittlement due to structural relaxation are a primary negative concern for the future clinical application of Mg-based BMGs. Wessels et al. [146] examined the relaxation at 20 °C and 37 °C for $Mg_{95-x}Zn_xCa_5$ BMG. An increase in the characteristic relaxation time from 10 to 30 days at 20 °C was observed as Zn increased from 29 to 32 at.%, correlating with dramatically reduced hydrogen gas. González et al. [149] indicated that 2 at.% Pd alloying in $Mg_{72}Zn_{23}Ca_5$ resulted in the formation of crystalline phases containing Pd, which contributed to a harder surface and delayed degradation.

Wang et al. [150] focused efforts on improving the ductility of MgZnCa BMGs by alloying with Yb, and reported a significantly improved ductility under bending and tensile loading through minor alloying with rare-earth element ytterbium (Yb) at an atomic concentration of 2% and 4%. The enhanced ductility is attributed to the increased density of shear bands close to fracture ends and larger plastic zones on the fracture surface. In comparison with that of Yb-free control, an *in vitro* cell culture study confirms an improved biocompatibility of this Mg-based BMGs alloyed with Yb as determined by MTT, live-dead, and cytoskeleton staining assays, respectively.

3.3. Surface modification of Mg-based biodegradable metals

Surface modification is one of the most effective ways not only to reduce and control the degradation behavior but also to improve the surface biocompatibility of Mg-based BMs. In the following sub-sections, the development and characterization of coatings for Mg alloys using various surface modification technologies will be summarized in three groups: mechanical, chemical, and physical methods (Table 3).

3.3.1. Mechanical methods

Common mechanical surface modification methods, such as machining [156,158], grinding [157], milling [151–153], burnishing [154,157], and laser shock peening [155], have been investigated on Mg alloys. An improved surface integrity was obtained with increased compressive residual stress and microhardness (HV) to different degrees by different methods.

Cryogenic machining with large edge radius tools led to the most desirable surface integrity on AZ31B [156]. The spraying of liquid nitrogen could also significantly reduce the surface temperature on AZ31B substrate and result in the formation of a grain-refined layer with more enhanced surface integrity (including grain refinement, surface roughness reduction, strong basal texture, and higher residual stress) than the dry machining technique.

The effects of cutting edge radius and cooling methods (dry and cryogenic) on surface integrity in machining of AZ31B were investigated [158]. Both the dry- and cryogenic-burnished surfaces exhibited better-improved degradation behaviors than the ground surface due to the formation of the grain-refined layer, while little difference was observed between the dry- and cryogenic-burnished groups. Besides the grain size and texture effect [158], the residual stress was also considered to influence the

Table 3
Summary of different surface modification techniques for biomedical Mg alloys.

Surface modification method	Techniques and modified layer	Main layer structure	Layer thickness	Residual stress[a]	HV[a]	v_{corr}[a]	Ref.
Mechanical methods							
High-speed dry milling	Cutting speed 1200–2800 m/min; feed 0.05–0.4 mm/rev; depth of cut 0.1–0.5 mm; increased HV up to 12 μm depth			+	+		[151–153]
Ball burnishing	Dual purpose oil lubricant and coolant, hydraulic pressure 1–16 MPa; 5–6 °C increase in temperature; increased residual plastic strain until 250 μm depth			+	+		[154]
Laser shock peening	The estimated spot diameter ~250 μm, average power 8 W, power density 78 GW/cm^2, performing in water confined regime at a depth of 1–2 mm			+			[155]
Cryogenic machining/burnishing	Cutting speed 100 m/min, feed rate 0.1 mm/rev, rake angle −7°, using liquid nitrogen as coolant; formation of a nanocrystalline grain structured layer with strong basal texture on the surface	Nano crystalline grain structure	3.4 mm/burnishing; 15 μm/machining	+	+	–	[156–158]
Chemical methods							
Chemical conversion coating	Immersing in 40% HF for 3–168 h, RT.		<3 μm to			–	[64,159,160]
Fluoride treatment	Conversion coating thickness depends on the treating time	MgF_2	200 μm				
Alkali heat treatment	Hydrothermal treated in NaOH, 160 °C, 3 h	$Mg(OH)_2$	100 μm			–	[161–164]
	Alkalized solution, i.e. $NaHCO_3$ based solution, RT, following heat treatment at 773 K, 10 h	MgO	<30 μm				
Electrochemical treatment	Anodic oxidation, 2–100 V, 3–10 min;		<20 μm			–	[165–168]
Anodic oxidation and MAO	MAO, 300–500 V, 5–35 min, alkaline based electrolyte with addition of Ca, P, Si and F containing compound	MgO and others					
Electrodeposition	Acidic Ca and P containing electrolyte, 0.4-20 mA/cm^2 for 30–80 min, 60–85 °C	DCPD, HA, FHA	10–20 μm			–	[169–172]
Biomimetic deposition	Immersing in SCS for 48 h followed by heat treatment at 300 °C for 2 h	HA	300 μm			–	[47,173–177]
	Immersing in concentrated SBF and followed by NaOH or steam treatment	HA					
	Immersing in acidic Ca, P or other cations containing electrolyte, pH 4–5, 60–80 °C, 2 min, 7 d	Ca–P based compound	0.2–20 μm				
Sol–gel	Thin film prepared by dipping-coating method followed by heat treatment	β-TCP, HA	0.45–500 μm			–	[178,179]
Organic and polymer coating	Dip-coating methods obtained saline based, PLGA, PLLA, Chitosan, PEI/PSS/8HQ/PSS multilayered coating	Saline based, PLGA, PLLA, PCL, CS, PEI/PSS/8HQ/PSS	2–70 μm			–	[180–186]
	Spin coating methods obtained PCL, PLLA coating		0.3–1 μm				
	Spraying methods obtained PCL coating						
Physical methods							
Ion implantation PIII&D	10–60 kV, 2–4 h, including O, Zn ion implantation, ~nm of the modified layer					+/–	[185,187–190]
IBAD	C–N (240 nm thick) and calcium phosphate coating (3 μm thick)					–	[191,192]
PVD, PECVD	High purity Mg coating					–	[193–195]

[a] +/– stands for the increased/decreased values for materials properties parameters, including residual stress, hardness HV and degradation rate v_{corr}.

degradation of Mg alloys but with little actual contribution [152,157].

Salahshoor et al. [151–153] studied the Mg–0.8Ca alloy processed by high-speed dry milling and indicated this technique was safely performed without chip ignition. A clean surface was generally obtained with slight flank build-up formation. The strain hardening effect with increased surface HV was observed within 12 μm of depth below surface [152,153].

Salahshoor et al. [154] carried out the ball burnishing process on the Mg–0.8Ca alloy using dual-purpose oil serving as both lubricant and coolant. Cooled by the dual-purpose oil, the in-depth distribution of temperature fields showed only about a 5–6 °C increase in the applied pressure range. Both compressive and tensile residual stress increased beneath the surface. The residual stresses were all compressive below 200 μm depth. Small tensile residual stresses (10–60 μm below surface) were also observed for some pressures.

Sealy et al. [155] used the laser shock peening (LSP) method to impart compressive residual stress to the Mg–Ca alloy and found that high compressive residual stress has great potential to slow corrosion rates.

3.3.2. Chemical methods

3.3.2.1. Chemical conversion coating. Chemical conversion coatings are produced by chemically bonding a superficial metal oxide or metal salt layer to the Mg alloy surface. This method can be used individually or as pretreatment before polymer coating.

(1) Fluoride conversion coating

Two typical techniques have been carried out for fluoride treatments. For the first technique, Mg alloy samples were directly treated with hydrofluoric acid or fluoride salt. An MgF_2 conversion

layer is formed on the Mg alloy surface based on the chemical reaction occurring at the interface between the sample and solution [159,160,196]. Yan et al. [160] indicated that the thickness of MgF_2 layer on AZ31B increased with increasing time of treatment and became a constant (about 2.75 μm) after 72 h in hydrofluoric acid. At the same time, the 72 h fluoride treated AZ31B showed the lowest corrosion current density and could maintain its mechanical integrity for approximately 45 d in simulated body fluid [160]. For the second technique, Mg alloy samples were pretreated in a sodium hydroxide solution to establish a $Mg(OH)_2$ layer. The $Mg(OH)_2$ layer was then converted into an MgF_2 layer by immersing it in hydrofluoric acid. The thickness of the MgF_2 layer is normally thicker than those produced by the first technique, depending on the immersion time in sodium hydroxide solution [64,73]. Both techniques could slow down the corrosion rate of the Mg alloy substrate. The fluoride treatment might benefit the orthopedic application due to its osteoblastic stimulation and increased bone formation [60]. The fluoride treatment was also used as the pre-treatment technique followed by the subsequent organic [180] or ceramic [197] coatings.

(2) Alkali treatment

Alkali-heat treatment has been introduced to improve the corrosion resistance of the Mg alloy substrate by forming a $Mg(OH)_2$ or MgO coating on the sample surface. Al-Abdullat et al. [198] reported that a $MgCO_3$ coating was formed during a $NaHCO_3$ alkali treatment, which provided better protection than the $Mg(OH)_2$ layer and enhanced the precipitation of calcium and phosphorous on the sample surface. Li et al. [161] indicated that the successive heat treatment at 773 K could convert the $MgCO_3$ coating into MgO coating, which further improved the corrosion resistance and showed no signs of inhibitory effects on cell growth. Gu et al. [162] investigated the corrosion behavior of alkali-heated Mg–1Ca alloy using different alkaline solutions and found the corrosion rate of samples followed the ranking orders: $NaHCO_3$ heated < Na_2HPO_4 heated < Na_2CO_3 heated. Zhu et al. [163] carried out the alkali-heat technique by hydrothermal treatment on AZ31 in NaOH solution at 160 °C. Thereafter, they found that the hydrothermal treatment in deionized water could improve the corrosion resistance of the substrate. The corrosion rate slowed down with increasing temperature and time of the treatment [164]. All of the reported alkali-heated methods were proved to improve the corrosion resistance of the substrate and the calcium phosphate deposition *in vitro*.

3.3.2.2. Electrochemical treatment.

(1) Anodic oxidation and micro-arc oxidation

Anodic oxidation is an electrolytic process encompassing the anodic electrode reactions combined with electric field driven metal and oxygen ion diffusion to *in situ* produce an oxide film on the anode surface. It is a well-established method to slow down the corrosion rate of Mg alloys. Hiromoto et al. [199] indicated that the degradation rate of anodized pure Mg varied with the applied voltage in 1 N NaOH: 7 V > untreated ≈ 20 V > 100 V. The successive steam treatment could effectively seal the pores in anodized film and significantly retard the degradation. In addition, a porous film formed at 7 V and 100 V, showing local corrosion and more precipitation of calcium phosphate than the non-porous film formed at 2 V and 20 V in Hank's solution [166,199].

Micro-arc oxidation (MAO) shares the similar electrolytic process with anodic oxidation while performing at a high-voltage discharge. MAO can remarkably improve the material properties including hardness, wear resistance, corrosion resistance, and adhesion strength compared to the anodic oxidation treatment. Gu et al. [165] reported the degradation and cell biocompatibility of an MAO treated Mg–Ca alloy at 300–400 V. The applied voltage influenced the thickness and pore size of MAO coating and, thus, affected the degradation behavior. The 360 V treated MAO coating produced the most superior long-term corrosion resistance during the 50 d immersion in Hank's solution, promoted the MG63 cell adhesion and proliferation, and also improved the wear resistance [200] and blood compatibility [201] of the Mg substrate.

To improve the biocompatibility and bioactivity of the coating, Ca and P were also introduced into the electrolyte [168,202,203]. Srinivasan et al. [203] compared the MAO coating obtained from a KOH-based and a $Ca(OH)_2$-based electrolyte with the same level of phosphate ions at 30 mA/cm^2 for 15 min. The MAO coating obtained from the $Ca(OH)_2$ electrolyte exhibited a thinner coating (38 ± 5 μm) than the KOH coating (56 ± 6 μm) while the calcium containing compounds in the coating contribute to higher corrosion resistance and stability than the compounds containing potassium. Srinivasan et al. [202] further optimized the Ca/P ratio in the electrolyte and indicated that the coating obtained from 1:5 electrolytes possessed the best corrosion resistance. Yao et al. [168] also reported that the change of Ca concentration in electrolytes was effective for adjustment of the Ca/P ratio in the coating of AZ91D given a reduced corrosion current density by two orders of magnitude [168]. However, the MAO coating achieves a porous surface that weakens the protection effect of the coating. In order to further slow down the degradation, the subsequent treatments have been applied to seal the pores including sol–gel [204], electrodeposition [205–207], and the polymer sealing [208–210] methods.

(2) Electrodeposition

Electrodeposition is an electrical process, such as electrolysis or electrophoresis, which is utilized to deposit a material onto the substrate. To improve the surface biocompatibility and bioactivity, calcium phosphate coatings, including hydroxyapatite (HA), fluoridated hydroxyapatite (FHA), and brushite (DCPD), have been prepared by the electrodeposition technique using the acidic $Ca(NO_3)_2$, $NH_4H_2PO_4$, and $NaNO_3$ electrolyte systems. It has been indicated that the as-deposited coating phase is DCPD, which can be transformed into HA after alkali heat treatment [169,211]. The HA coating showed lower solubility than the DCPD coating and, thus, exhibited better protective effects [169]. However, the HA coating is fragile and can be easily broken down. Song et al. [169] found that a FHA coating could be obtained by adding NaF in the above electrolyte system. This FHA coating was more stable than the DCPD and HA coatings and, thus, remained intact after immersion in m-SBF for one month. It was shown to promote osteoconductive minerals precipitation as well as cellular proliferation and differentiation. Wang et al. [171] suggested a pulse electrodeposition process using positive and reverse currents. This technique improved the bonding force between the coating and the substrate as well as the protection effect of the coating [212]. A Ca-deficient HA coating was prepared by the pulse electrodeposition process [171], and it could slow down the degradation, strengthen the Mg–Zn–Ca alloy substrate, as well as improve bone response [170,171]. In addition, the Ca-deficient HA coated Mg–Zn–Ca alloy exhibited local peeling-off coating and faster degradation under the compressive stress close to the human tibia [213].

3.3.2.3. Biomimetic deposition. The biomimetic process is based on simple chemical immersion techniques to produce Ca–P coating on the substrate wherein different kinds of solutions have been adopted. Keim et al. [174] and Zhang et al. [214] reported the

preparation of bone-like calcium phosphate coating by immersing Mg substrate into concentrated SBF for 24 h. A Ca–P coating was then obtained, which could delay the degradation of pure Mg and enhance cell adhesion and spreading. Yang et al. [176] reported the slower degradation of AZ31 with a calcium phosphate coating prepared by 48 h immersion in supersaturated calcification solution (SCS). The pH of the solution investigated above is neutral.

Recently, Gray-Munro et al. [215] found that the calcium phosphate coatings were better deposited onto Mg alloys under mildly acidic conditions. The kinetics of the biomimetic deposition was influenced by the anodic dissolution of Mg substrate, leading to a poor crystalline Mg containing HA coating formed on the surface. Wang et al. [47] indicated that the calcium phosphate coating was effective to reduce the degradation of AZ31B and also noted that the coated AZ31B maintained 85% of the initial strength integrity after a 120 d immersion in SBF. In addition, the coating was found to gradually degrade and even disappear *in vitro* and *in vivo* with degradation products simultaneously depositing on the Mg alloy surface [47]. Its simplicity in preparing the coating solution could not only be counted as advantageous, because other easily inserted biocompatible ions could also invaluably benefit the biomimetic coating. Zhang et al. [175,216,217] and Singh et al. [218] successfully incorporated Zn and Si into the biomimetic calcium phosphate coating, which exhibited good protection of the Mg alloy substrate and improved surface cytocompatibility.

3.3.2.4. Sol–gel treatment. Sol–gel coating is prepared using a colloidal solution as the precursor to synthesize an integrated network, which will be further crystallized at high temperature to generate a porous, nanocrystalline coating with a controlled microstructure. Hu et al. [178] prepared a nano TiO_2 coating on AZ31 by the sol–gel method, and found that the degradation behavior of the resulting coating film depended upon the annealing temperature (250–400 °C) and time (1–2.5 h). With increasing annealing temperature, the size of nanospherical TiO_2 particles increased and led to an increased degradation rate. Moreover, the degradation rate decreased with prolonged annealing time at 300 °C. Roy et al. [179] used the calcium nitrate, phosphorus pentoxide and tetraethyl orthosilicate as precursors and obtained the porous coating (~50 μm) composed of nano sized Si-containing calcium phosphate particles. The incorporation of Si improved the crystallization of the HA, but did not alter the degradation kinetics of the Mg–4Y alloy substrate. The coatings were found to be stable for at least 3 d *in vitro* before parts of the coatings would peel off. Improved adhesion and proliferation of MC3T3-E1 cells were observed on such Si-containing Ca–P sol–gel coating.

3.3.2.5. Organic and polymer coating. The organic and polymer based coatings have attracted great attention because of their potential for drug delivery systems and their ability to function with organic biomolecules. The degradable polymer based coatings are assumed to provide the protection of the Mg alloy substrate in the early stage and gradually degrade with time. Several degradable polymer coatings, such as polycaprolactone (PCL) [186,219,220], poly(L-lactic acid) (PLLA) [186,220], poly(DL-lactide-co-glycolide) (PLGA) [221], and chitosan [222], were applied to Mg alloys by dip coating, spin coating, and spraying methods. The above degradable polymer coatings were shown to slow down degradation and improve surface biocompatibility of the alloys, as confirmed by the enhanced cell attachment and proliferation on the coatings [186,219–222]. Generally, the thickness and quality of the coatings mainly depend on the viscosity of the polymer medium, which in turn depends on the molecular weight and concentration of the polymer that would further influence the protective effect of the coatings. Li et al. [221] found that higher (4%) concentration of the PLGA solution for dip coating would lead to a thicker coating (72 ± 5 μm) than the solution with a lower (2%) concentration (33 ± 5 μm), but both PLGA coated Mg–6Zn alloys exhibited similar degradation behavior. Wong et al. [219] applied two different concentrations (2.5% and 3.33%) of PCL solution to modify the PCL membrane by spraying different pore sizes and porosities. Both *in vitro* and *in vivo* corrosion tests indicated that the AZ91D coated with low porosity PCL membrane exhibited slower degradation than that with high porosity membrane [219]. Xu et al. [186,220] reported the preparation of uniform and non-porous PCL and PLLA coatings on extruded Mg under spin coating condition. The PLLA coating, exhibiting an amorphous nature, provided better protection effect and bonding to Mg substrate in comparison with the semi-crystallized PCL coating. For both coatings, the low molecular weight (LMW) polymers resulted in a thinner coat and better adhesion strength than the high molecular weight (HMW) polymers whereas faster degradation was observed for LMW coated Mg alloys. Gu et al. [222] reported that the six-layer coating prepared by chitosan with a molecular weight of 2.7×10^5 had a smooth and intact surface morphology and provided better protection of Mg–1Ca alloy substrate.

Some non-biodegradable polymer coatings have also been proposed to modify the surface of biomedical Mg alloys. Zomorodian et al. [180] reported a glycidoxypropyltrimethoxysilane (GPTMS) based coating on AZ31 comprising an inner dense layer with ~1.5 μm in thickness and an outer porous layer of a few hundred nanometers. The surface pretreatment of the Mg alloy substrate strongly influenced the coating durability. Pretreatment by hydrofluoric acid was more effective than the mechanical polishing [180]. The single layered poly(ethylene imine) (PEI) [223] and multilayered PEI/(poly(styrenesulfonate, sodium salt)) and PSS/(8-hydroxyquinoline)8HQ/PSS [224] also provided protection to the Mg alloy substrate. The effect of the protection was related to the solvent type, pre- and subsequent treatment (i.e. the degradation behavior was further improved with glutaraldehyde stabilizer). Additionally, a conducting polymer coating was applied using the electrodeposition method, which needed a polystyrene (PS) coating for Mg electrode preparation and the final electrodeposition of 3,4-ethylenedioxythiophene (EDOT) [225].

Another application of the polymer was to seal the porous MAO or hydrothermal coating with an aim to further reduce the degradation rate of the substrate as well as to support the platform for drug delivery. The MAO/PLGA/paclitaxel (PTX) coating was prepared by the dipping method on AZ81, which improved corrosion resistance and the biocompatibility of the MAO coating [184]. The PTX exhibited a sustained releasing profile with no significant burst release, and the releasing rate could be controlled by the ratio of the LA:GA of the PLGA layer [184]. Xu et al. [185] also reported a similar drug releasing behavior of a composite coating, containing a cross-linked gelatin with PLGA nano particles and PTX, prepared by the emulsion solvent evaporation/extraction technique on MAO modified WE42 alloy. Ng et al. [226] prepared a Mg stearate coating anchored in the $Mg(OH)_2$ layer formed during the hydrothermal treatment. This double-layered coating improved the corrosion resistance of pure Mg compared to a single $Mg(OH)_2$ coating.

3.3.3. Physical methods

The surface modification methods of biomedical Mg alloys based on the physical treatment include ion implantation, plasma immersion ion implantation [187,227] and deposition (PIII&D) [228], ion-beam assisted deposition (IBAD) [191,192], physical vapor deposition (PVD) [193,194], plasma enhanced chemical vapour deposition (PECVD) [195], and ion plating [229].

Ion implantation is a process that introduces the energetic ions into the surface layer of the metal substrate via bombardment.

Aiming at improving the corrosion resistance, several passive elements have been implanted with Mg in order to form a metal oxide layer on the surface, including Cr, Zn, Al, Zr, and Ti. Unexpectedly, the inclusion of Cr and Ti induced the galvanic corrosion and resulted in accelerated degradation [227,230] while adding the element Al could slow down the degradation due to the aluminum oxide layer [231]. Wan et al. [187] also reported the increased degradation rate of Mg–Ca alloy after implantation of Zn ion at 60 kV. Wu et al. [190] implanted O and observed a much thicker oxide layer on the surface of Mg–Zn–Nd–Zr alloys; however, this technique contributed little to the enhancement of corrosion resistance. The combination of prior implantation of the passive elements (i.e. Cr and Al and the following O) could thicken the metallic oxidized surface layer and retard the surface degradation of Mg [189,190,227]. In contrast, Liu et al. [228] adopted the PIII&D technique to introduce Ti, Al, and Zr individually into AZ91 at 10 kV. An implanted layer with a tri-layer microstructure was obtained with an outer layer composed of mainly metal oxide with a small amount of MgO and $Mg(OH)_2$, an intermediate layer containing metal oxide and metallic implanted particles, and a bottom layer rich in implanted metallic elements. Among three groups, the implantation and deposition of Al provided the best protection to AZ91 substrate owing to the compact Al_2O_3 and intermixed layer [228].

In the case of IBAD techniques, Yang et al. [191,192] indicated that IBAD coating (CN and CaP coating) significantly increased the surface hardness and elastic modulus and also slowed down the degradation of AZ31. The ion-plating of Ti coating also benefited in delaying the degradation of pure Mg [229].

The above-mentioned elements Cr, Ti and Al are reported for theoretical purposes but would not be recommended for biomedical applications.

3.3.4. Comprehensive comments on the current surface modification techniques

The main purpose of surface modification of Mg-based BMs is to slow down their degradation rate. Most of the reported coatings can reduce the degradation rate of the Mg alloy substrate to different extents. As shown in Fig. 5, the reduction of the degradation rate ranges from ~20% to over 90% after surface modification. However, the degradation of the coated Mg alloys is suppressed but not stopped. The cracks or defects could be observed on the coating as the degradation process continues, which might accelerate the degradation of the substrate locally. For example, Gu et al. [165] reported the presence of cracks on the 360 V MAO treated Mg–1Ca alloy after 50 d of immersion in Hank's solution. Therefore, the durability and integrity of the coat is crucial for the lifetime of medical devices fabricated from Mg-based BMs, which is related to the topography and bonding strength of the coatings to the Mg-based BM substrate.

The coating topography shows a significant impact on effectiveness of the coating on Mg-based BMs. Theoretically, a thick and compact coating will better resist the corrosion of the Mg based BM substrate. However, it is almost impossible to get a complete compact coating by chemical methods because of the hydrogen bubbles generated during coating. Thus, a pre-treatment to improve the corrosion resistance of the substrate could also benefit the quality and the resulted protection effect of the coating. Fig. 6 presents the surface morphology of coatings prepared by different methods. The alkali-heated, biomimetic deposited, and electrodeposited coatings exhibited rough and crystallized surface morphologies with thickness ranging between 0.2 and 300 μm. These three coating were composed of the pile-up crystals precipitated from the treating electrolyte and, thus, usually revealed a relatively loose coating structure. The fluoride

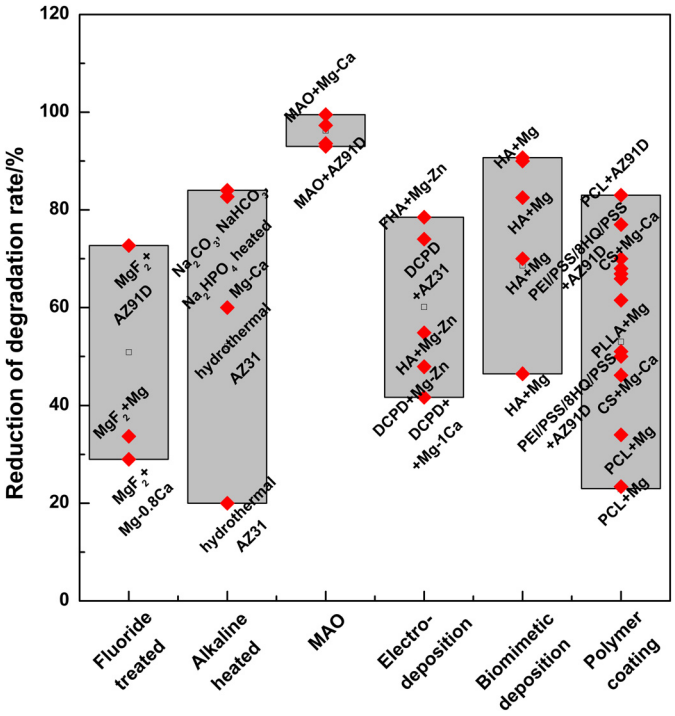

Fig. 5. Comparison of the coating effectiveness on corrosion resistance of Mg alloys substrates.

treatment and the spin-coated PLLA coating produced a relatively smooth surface but limited coating thickness (~several micrometers). The above-five coating methods protect Mg-based BM substrate in a similar way. The MAO coating, with a porous outer surface but a compact inner underneath surface feature, could protect the Mg based BM substrate most effectively, as shown in Fig. 6(d).

The bonding strength of the coating to the substrate is strongly influenced by the surface modification method. The coatings prepared by chemical methods indicate relatively low bonding strength in the order of several MPa. For example, Sekiguchi et al. [233] reported that the shear strength of chemical conversion coatings on AZ31 and AZ91D ranged between 3 and 16 MPa. The spin-coated PLLA and PCL coatings showed close bonding strength ranging between 1.5 and 4.1 MPa [186]. The bonding strength can be significantly improved by the electrochemical methods. The calcium phosphate coatings prepared by the pulse electrodeposition, which exhibited the positive and reverse pulse currents, improved the shear strength between the coating and Mg alloy substrate to 41.8 MPa [171] in comparison with the traditional electrodeposited HA coating (14 MPa) [234]. As the degradation of the Mg alloy substrate proceeds, the bonding strength of the coating with the substrate decreases.

The development of different coating technologies targeted different clinical applications, such as coronary stents and orthopedic implants. As summarized in Table 3, great interest has been focused on Ca–P based inorganic and degradable polymer coatings, mainly aiming at bone implants and intraluminal stent related applications, respectively. In general, rough Ca–P based inorganic surfaces obtained by the alkali-heated, MAO, biomimetic deposition, electrodeposition, and sol–gel methods are not appropriate for stent application, whereas biopolymer coatings are helpful for enhancing the hemocompatibilty of the bare Mg-based BM, especially at the initial implantation stage.

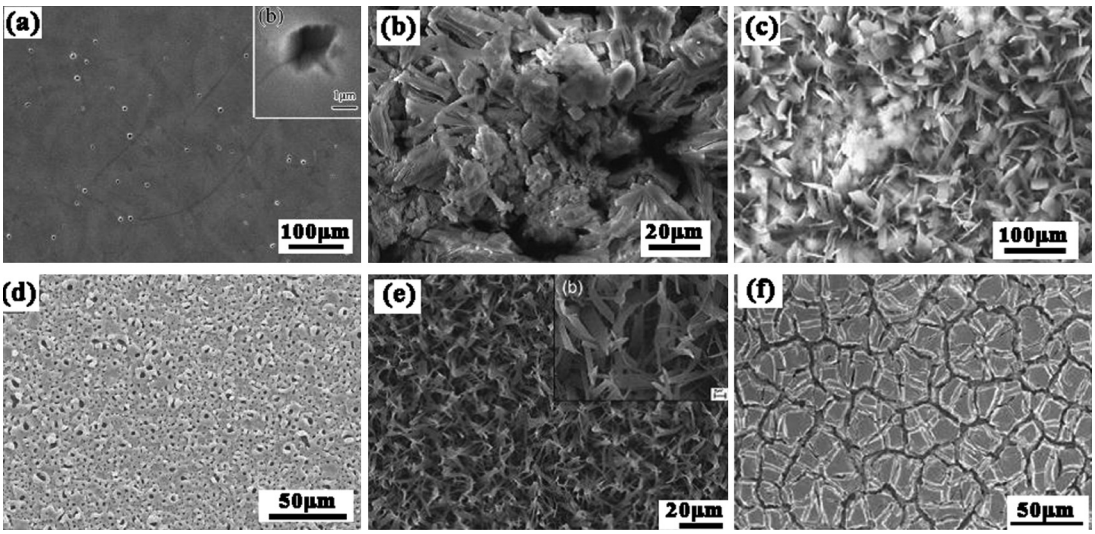

Fig. 6. The surface morphology of the coatings prepared by different methods: (a) fluoride conversion coating [232], (b) alkali-heated coating [162], (c) biomimetic deposition [214], (d) MAO coating [200], (e) Electrodeposited [169], and (f) PLLA coating [186].

3.4. Animal testing and clinical trials of Mg-based biodegradable metal implants

3.4.1. Animal testing of Mg-based biodegradable metal implants within bone

Over 20 kinds of Mg-based BMs have been evaluated within bones of small (rats, guinea pigs, and rabbits) and large (sheep) animal models to characterize the *in vivo* corrosion as well as the bone response. The results are summarized in Table 4.

(1) Mg-based BMs indicate good biocompatibility in bone. All of the conducted research reported enhanced new bone formation around the implants of Mg-based BM and in the vicinity including enhanced local periosteal and endosteal bone formation. The degradation product layer on experimental Mg-based BM implants revealed high deposition of Ca–P based mineral. Half of the cases in which bare Mg-based BMs were implanted showed direct contact between the layer of degradation product and new bone, while the rest indicated the presence of a fibrotic layer or a gap between the degradation product layer from bare Mg-based BM implant and the new bone, as listed in Table 4. Zhang et al. [242] indicated that the layer comprised of two distinct membrane structures with many fibroblasts in one that is closer to the bone. This layer was still present six months post-surgery. All of the cases with modified surfaces demonstrated a direct contact between Mg-based BM implant and the new bone without the fibrotic layer.

(2) The subcutaneous gas cavities were observed in approximately 70% of the reported cases for bare Mg-based BM implant (see Table 4), which usually initiated in the early stages (7–30 d) of implantation and gradually disappeared without special treatment but with moderate inflammatory response. Witte et al. [53] considered the formation of gas cavities to be related to the anatomical implantation sites because of different hydrogen solubility and diffusion coefficients in different tissues. Therefore, the local gas cavities could be avoided for the Mg-based BMs exhibiting slower degradation rates with less hydrogen generation per time interval. The gas cavities were not observed in all cases of the surface-modified Mg-based BMs. There was an exceptional case in which no gas formation was observed in a fast degrading RS/PM Mg–5Bi–1Ca alloy that almost completely dissolved in four weeks [246]. Remennik et al. [246] attributed the lack of local gas cavities to the fine microstructure (grain size ~2 μm), which restricted the coalescence of hydrogen gas bubbles on the metal surface. Thus, the large gas–liquid surface enhanced hydrogen dissolution and local removal from the corrosion front.

(3) The bare Mg-based BMs exhibited a wide range of degradation period from 4 to 52 weeks (1 year) depending on their chemical composition and processing history (see Table 4). Furthermore, the degradation of the implanted Mg-based BM was also strongly related to the local microenvironment (local perfusion, stress, pH) at the anatomical implantation sites. The Mg-based BM implant exhibited a faster degradation within the bone tissue or areas with high blood supply (i.e. marrow cavity or the cancellous bone) than within the cortical bone tissue [240]. Zhang et al. [242] found that up to 95% of the extruded Mg–Mn–Zn alloy implants degraded in the bone marrow in comparison to 5% in the cortical bone six weeks post-surgery. Remennik et al. [246] revealed that, depending on the area of implantation, degradation rate could be ranked in the following order: subcutaneous > muscle > bone.

(4) The fast degeneration of mechanical integrity of bare Mg-based BM needs to be improved independent of the implantation site. From Table 4, surface coating could provide the protection of Mg-based BM substrates in the early stages of implantation, exhibiting slower degradation and higher corrosion uniformity and, thus, slow down the strength decay. The Mg–0.8Ca alloy indicated a 40% loss in volume and resulted in 70% loss in bending strength while a 25% volume and 55% decay in strength were observed when coated with the MgF_2 layer over a six-month period of implantation [237].

3.4.2. Animal and clinical testings on Mg-based biodegradable metal implants within blood vessels

To date, AE21 and WE43 bare stents were investigated with animal models, and the Mg based absorbable metal stent (AMS) was designed and evaluated in both animal tests and clinical trials, as summarized in Table 5. It can be seen that these Mg-based BM stents are associated with a high procedural success rate and are well tolerated within different kinds of blood vessels, such as coronary and pulmonary arteries, and lower limb vessels (see Table 5). The degradation of Mg-based BM stent was safe with acceptable host responses in animals and humans, even a newborn baby. However, intimal hyperplasia and the resulting reduction of

Table 4
Summary of animal tests of Mg alloy implants within bone.

Implants	Implantation site		Period/ weeks	New bone	Bone contact	Gas cavity	Degradation rate/mm/yr or residual implant %	Strength loss	Ref.
AZ31/gravity cast, rod AZ91/gravity cast, rod WE43/gravity cast, rod	Marrow cavity, guinea pig		18	+	+	+	0%		[61,108]
LAE442/gravity cast, rod							30 vol.%		
AZ91/cast, rod	Femoral diaphysis, rabbit		8	+	+	–	67 vol.%		[219]
AZ91 + PCL/cast, rod							95–100 vol.%		
AZ31/extruded, screw	Hip bone, sheep		12	+	+		Main body		[235]
Mg–Sr/rolled, rod	Marrow cavity, mice		4	+	–	+	1.01 mm/yr		[71]
LAE442/extruded, rod	Femoral condyle, rabbit		12	+	–	–	0.31 mm/yr 89 vol.%		[64]
LAE442 + MgF_2/extruded, rod					+	–	0.13 mm/yr		
LAE442/extruded, rod					–	–	79 vol.%[a]	~46%[a]	
Mg–0.8Ca/extruded, rod, smooth	Marrow cavity, rabbit		24	+	–	–	60 vol.%[a]	~72%[a]	[236,237]
Mg–0.8Ca + MgF_2/extruded, rod					+	–	74.67 vol.%	~55%	
Mg–0.8Ca/extruded, rod Smooth	Femoral epicondyle, rabbit		28	+		+	V_{corr}, sand balst >		[238,239]
Sand blast				+		+	threaded > smooth		
Threaded				+	–	+			
Mg–0.8Ca/extruded, screw	Transcortical implantation in tibia, rabbit	Muscle	8	+		+	91.23 vol.%	Decreased pull out force to 123.37 N	[240]
		Cotex					98.63 vol.%		
		Marrow cavity					91.18 vol.%		
Mg–Ca/cast, screw	Femoral diaphysis, rabbit		12	+	–	+	1.27 mm/yr 20mass%		[70]
Mg–6Zn/extruded, rod	Femoral diaphysis, rabbit		14	+	–	+	2.32 mm/yr 13%		[46]
Mg–Mn–Zn/extruded, rod	Femoral diaphysis, rat		18	+	–		46%		[241,242]
Mg–Mn–Zn + Ca–P coating/extruded, rod	Femoral diaphysis, rabbit		4	+	+	–	Main body		[177]
Mg–2Zn–0.2Ca/extruded, rod	Femoral diaphysis, rabbit		50	+	–	–	2.15 mm/yr[b]		[243]
Mg–2Zn–0.2Ca + MAO + DCPD/extruded, rod					+	–	1.24 mm/yr[b]		
Mg–5Zr/cast, rod Mg–1Zr–2Sr/cast, rod Mg–2Zr–5Sr/cast, rod	Tibia, rabbit		12	+	– + –	+	V_{corr}, Mg–1Zr–2Sr > Mg–5Zr and Mg–2Sr–5Sr		[105]
Mg–Y–Nd–HRE*/–, rod	Femoral diaphysis, rat		24	+	+	–	Main body	Increasing bonding strength with time	[244]
WZ21/extruded, pin	Femoral diaphysis, rat		24	+	+		V_{corr}, WZ21 < BMG < ZX50		[245]
ZX50/extruded, pin				+	–	+		100% loss at 3months	
MgZnCa BMG/cast, pin				+	+			Fracture at 3 months	
Mg–5Bi–1Ca/RS, rod	Femoral condyle, rabbit		4	+	–	+	1.85 mm/yr		[246]
AZ91D scaffold/porosity 72–76%	Condyle, rabbit		12	+	–	+	0%		[78,79]

[a] LAE442 and Mg–0.8Ca show 35 vol.% and 65 vol.% left and over 70% and 90% bending strength loss after 52w (1 year) implantation.
[b] Both bare and MAO + DCPD coated Mg–Zn–Ca alloy completely dissolved after 32w implantation.

Table 5
Summary of animal tests and clinical trial of Mg alloy stent within blood vessels.

	Alloy	Biocompatibility	Degradation	Ref.
Animal test	AE21 stent (pig, coronary artery)	40% loss of perfused lumen diameter between days 10 and 35 due to neointima formation; a 25% re-enlargement between days 35 and 56 caused by vascular remodeling	Linearly degradation ~89 d	[247]
	WE43 stent (minipig, coronary artery)	The struts are covered by neointima after 6 d; higher minimal lumen diameter on week 4 and 12 than the 316L stent group	~98 d	[248]
	AMS (pig, coronary artery)	Show signs of degradation 28 d postsurgery; less neointima compare to 316L stent; stenosis increased from 28 d to 3 months; decreased lumen area due to the negative remodeling	~60–120 d	[249–251]
Pediatric use	AMS (preterm baby, pulmonary artery)	Normal serum Mg level on 72 h, persisted left lung perfusion throughout the 4-month follow-up, clinical tolerable to baby	~5 months	[252]
	AMS (newborn baby, aortic arch)	Restenosis after 3 weeks implantation; implantation of a 2nd AMS; the stent struts were substituted by a jelly-like $CaPO_4$ compound and fibrotic structure; flexible stent segment	–	[253,254]
	AMS (2-month-old girl, aorto-pulmonary collateral)	Restenosis after 4 months implantation of AMS	–	[255]
Clinical trial	AMS (20 patients, 23 stents, lower limb vascular)	A low immediate elastic recoil; 89.5% primary clinical patency after 3 months and 72.4% after 24 months; no blood or vessel toxicity	–	[256,257]
	AMS INSIGHT (60 patients, 74 stents, lower limb vascular)	Lower angiographic patency rate 31.8% for AMS treatment and comparable complication rate 5% with PTA treatment (patency 58%, complication rate 5.3%)	~4 months	[258]
	PROGRESS-AMS (63 patients, 71 stents, 8 centers, coronary artery)	Restenosis caused by stent recoil and intra- and extra-stent neointima at 4 months; the neointima decreased after over 12 months; No myocardial Infarction, subacute or late thrombosis, or death occurred	~4 months	[259,260]
	BIOSOLVE-I DREAMS (46 patients, two cohorts, cohort 1 for 6 months and 2 for 12 months)	7% rate of target lesion failure, 4.7% revascularization rate, no significant change of vasoreactivity between 6 and 12 months, reduced lumen loss from 6 month to 12 month, no death and no thrombosis	–	[261]

lumen diameter were detected in all cases. Moreover, Mg-based BM stents exhibited half of the proliferated intimal area in comparison to the traditional 316L SS stent [248,249]. Waksman et al. [262] reported that the subsequent β-radiation adjunct therapy could reduce the formation of neointima from $1.30 \pm 0.62\ mm^2$ to $0.49 \pm 0.34\ mm^2$ at 28 d follow-up.

Nearly all cases reported the unexpected high restenosis rates in follow-up observations because of negative vascular remodeling and the intimal hyperplasia [259]. As summarized in Table 5, the Mg-based BM stents exhibited a progressive degradation within blood vessels ranging from ~60 d to ~5 months. However, a much faster decay of mechanical integrity and the resulting fast degeneration of stent radial force could be expected. Heublein et al. [247] reported a positive vascular remodeling resulting in the re-enlargement of the lumen diameter between 35 d and 56 d follow-up. Schranz et al. [253] reported the Mg-based BM stent struts were substituted by a jelly-like $CaPO_4$ compound and fibrotic structure in a treatment case for critical recoarctation of the aorta in a newborn; and the stented vessel segment was flexible without influencing the surgical patch augmentation.

To overcome the limitations of the first generation of AMS, AMS-3 (named DREAMS) was developed with modifications to its chemical composition, strut design, and fast degradable polymer-coating carrier with an anti-proliferative drug. The preclinical studies showed prolonged scaffolding and stent integrity, less neointima proliferation, and increased radial force [263]. The first animal trial in the porcine model showed promising results in terms of the safety and efficacy for sustaining anti-proliferative effects up to 90 d and significant improvement in lumen diameter at 14 d and 28 d follow-up if compared to the bare AMS [263]. The one-year follow up of the clinical trial for BIOSOLVE-I DREAMS with 46 patients enrolled revealed significantly reduced lumen loss from six to twelve months, which was considered as a result of plaque regression and late expansive remodeling. In addition, the natural vessel angulation was observed in the six-month follow-up and maintained at twelve months, suggesting the real restoration of the vessel's natural architecture [261]. But, the study suffers from "the absence of a direct comparison with other permanent stents or scaffolds." Furthermore, it included only a few patients with simple lesions; thus, the results cannot be generalized to other types of lesions and findings need to be confirmed in larger studies [264].

4. Iron-based biodegradable metals

4.1. Development of Fe-based biodegradable metals

Compared with Mg-based BMs, Fe-based BMs have similar mechanical properties to stainless steel and are more attractive from a structural point of view (Table 6). However, the preliminary animal tests have revealed a slow degradation rate *in vivo*. Large portions of the pure Fe stent remained intact in the blood vessels twelve month post-surgery, which was considered to cause reactions similar to those found in permanent applications [77]. A more serious limitation is that its ferromagnetism negatively impacts the compatibility with certain imaging devices, such as the magnetic resonance imaging (MRI). Hence, research has focused on the development of new kinds of Fe-based BMs by modifying the

Table 6
Summary of the properties of reported Fe-based biodegradable metals.

Materials		YS/MPa	UTS/MPa	Elongation/%	Magnetic suspectibility/μm^3/kg	v_{corr}/mm/yr	Ref.
Pure Fe	Cast	–	–	–	–	0.008	
	Annealed (550 °C)	140 ± 10	205 ± 6	25.5 ± 3	–	0.16 ± 0.04	[265]
	Electroformed	360 ± 9	423 ± 12	8.3 ± 2	–	0.85 ± 0.05	[265]
	ECAPed (8 passes)	–	470 ± 29	–	–	0.02	[266]
	P/M	–	–	–	–	5.02[a]	[267]
	SPS	–	–	–	–	0.016	[268]
Nitride Fe		561.4	614.4	–	–	0.225	[269]
Fe–10Mn/forged + ht2[b]		650	1300	14	–	7.17[a]	[270]
Fe–10Mn–1Pd/forgerd + ht2[b]		850	1450	11	–	25.10[a]	[270]
Fe–30Mn/cast		124.5	366.7	55.7	–	0.12	[271]
Fe–30Mn–6Si/cast		177.8	433.3	16.6	–	0.29	[271]
Fe–30Mn/forged		169	569	60	0.16	0.12	[272]
Fe–30Mn–1C/forged		373	1010	88	0.03	0.2	[272]
Fe–3Co/rolled[b]		460	648	5.5	–	0.142	[45]
Fe–3W/rolled[b]		465	712	6.2	–	0.148	[45]
Fe–3C/rolled[b]		440	600	7.4	–	0.187	[45]
Fe–3S/rolled[b]		440	810	8.3	–	0.145	[45]
Fe–20Mn/P/M		420	700	8	0.2	–	[56]
Fe–25Mn/P/M		360	720	5	0.2	0.52	[56]
Fe–30Mn/P/M		240	520	20	0.2	–	[56]
Fe–35Mn/P/M		230	430	30	0.2	0.44	[56]
Fe–0.6P/P/M		–	–	–	–	7.75[a]	[267]
Fe–0.05B/P/M		–	–	–	–	7.17[a]	[267]
Fe–5W/SPS		–	–	–	–	0.138	[268]
Fe–1CNT/SPS		–	–	–	–	0.117	[268]
316L SS		190	490	40	0.5	–	[56]

[a] The electrolyte was simulated body fluid (Kokubo), while the other electrolytes were Hank's solution, PBS or 0.9% NaCl.
[b] The chemical composition was in atom percentage, while the others were in weight percentage.

chemical composition, microstructure, and surface of Fe with diverse manufacturing process technologies including casting, powder metallurgy, electroforming, and inkjet 3D-printing, to achieve a faster degradation and improved MRI compatibility, as illustrated in Fig. 7. For example, powder metallurgy Fe–Mn alloy had a faster *in vitro* degradation compared to the same alloy produced by casting because of the PM process porosity increasing the degradation rate. Electroformed iron also showed a faster *in vitro* degradation compared to Armco® Fe fabricated by casting since the electroformed material had a much finer microstructure with increased volume of grain boundaries, which are more susceptible to corrosive attack [273].

Alloying, subsequent processing, and heat treatment are common approaches to modify the mechanical, corrosion, and ferromagnetic properties of pure Fe [274]. Based on the microstructural, corrosion, magnetic, and toxicological considerations, Mn has been shown to be a suitable alloying element. Mn lowers the standard electrode potential of Fe [270] and exhibits anti-ferromagnetic behavior with 29 wt.% of addition [275,276]. Moreover, Mn is a trace element that is necessary in many

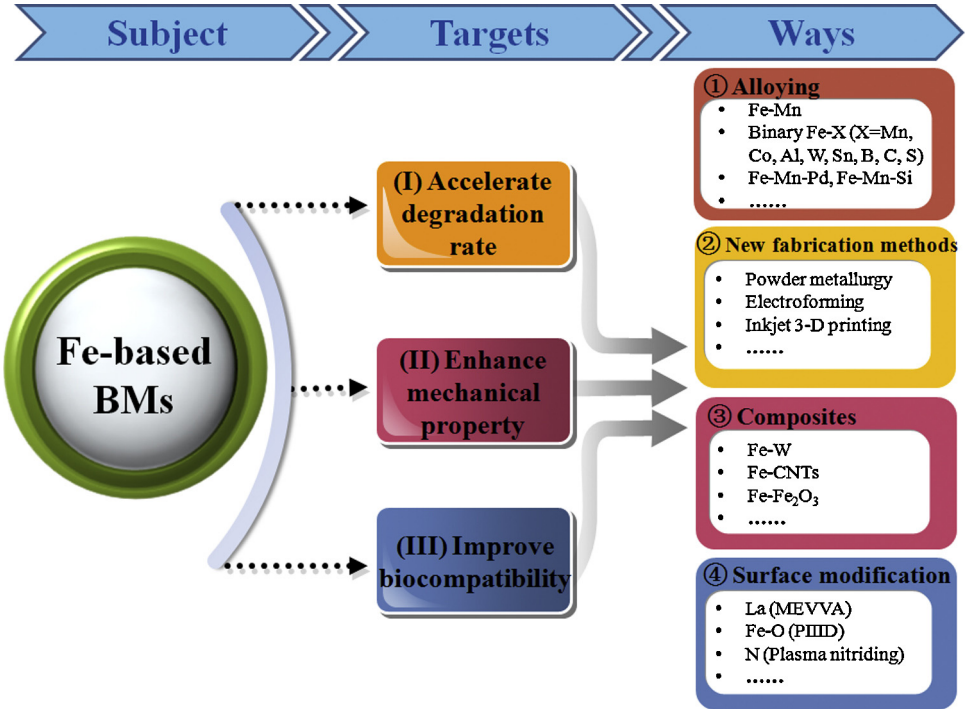

Fig. 7. Status of present research on Fe-based biodegradable metals.

enzymatic reactions. As summarized in Table 6, alloying with Mn increases the strength and degradation rate of pure Fe (i.e. as-cast Fe–30Mn (wt.%)) [271]. Liu et al. [271] also indicated that the addition of 6 wt.% of Si in Fe–30Mn established the shape memory effect, with which a recovery ratio 53.7% could be reached when the sample was deformed to the total strain of 3% and the exact pre-strain of 2.73%. A study by Xu et al. [272] reported that the as-forged Fe–30Mn–1C alloy showed significantly improved UTS and elongation up to 1010 MPa and 88%, respectively, which were exceedingly higher than those for 316L SS (490 MPa, 40%), and could simultaneously further reduce the magnetic susceptibility of the alloy. Enhanced degradation behaviors were observed for Fe–30Mn–6Si and Fe–30Mn–1C alloys in comparison with Fe–30Mn alloy [271,272]. Schinhammer et al. [270] indicated that adding 1 wt.% of Pd into the as-forged Fe–10Mn alloy could improve the tensile strength but weaken the ductility. High UTS (>1400 MPa) at ductility levels above 10% could be achieved by the subsequent heat treatment. The degradation rate of Fe–10Mn–1Pd accelerated ten times that of low carbon steel. Schinhammer et al. also did a study for Fe–Mn–C(–Pd) alloys [277]. The Fe–Mn–C–Pd alloys are characterized by an increased degradation rate compared to pure iron. The highest degradation rates of ≈0.21 mm $year^{-1}$ in SBF were measured for the TWIP-1Pd CW12-700 samples. The increase in the degradation rate compared to the TWIP samples was by a factor of 1.6. The results of cytotoxicity test for TWIP-1Pd show that it is mainly Mn that limits the cytocompatibility of the alloys [278]. Liu et al. [45] investigated the effect of eight alloying elements (Mn, Co, Al, W, Sn, B, C, and S) at 3 at.% on the degradation and biocompatibility of pure iron, and recommended using Co, W, C, or S as the alloying element for pure Fe, due to their appropriate mechanical properties, faster degradation rate, and the accepted cyto- and hemo-compatibility.

The powder sintering process has tried to fabricate Fe-based BMs. Hermawan et al. [275,276] prepared the Fe–Mn binary alloys containing 20–35 wt.% of Mn through the powder sintering process from high purity Fe and Mn powders followed by a series of cold rolling and resintering cycles. Fe–20Mn and Fe–25Mn were constituted of γ + ε phases. Both alloys showed higher ultimate strength (702 ± 11 MPa for Fe–20Mn and 723 ± 19 MPa for Fe–25Mn) but less ductility (7.5 ± 1.5%, 4.8 ± 0.4%) and degradation rates (0.5 ± 0.1 mm/yr for both alloys) than Fe–30Mn (518 ± 14 MPa, 19.0 ± 1.4%, 0.7 ± 0.1 mm/yr) and Fe–35Mn (428 ± 7 MPa, 32.0 ± 0.8%, 0.7 ± 0.1 mm/yr), which were composed of a single γ phase. In addition, the magnetic susceptibility of the Fe–Mn alloys decreased as Mn content increased, but it was not changed by the plastic deformation [275,276]. Metabolic activities of 3T3 fibroblasts were closely observed for the Fe–Mn alloy powders with different Mn contents. The inhibition effect increased with increasing powder concentrations [56]. Wegener et al. [267] prepared the Fe–C, Fe–P, Fe–B, and Fe–Ag alloys through the PM methods. It was revealed that alloying element P features beneficial properties in density and strength, but it increases the degradation rate of the resulting Fe-based BM.

Moravej et al. [279] prepared the pure Fe films using an electroforming technology. The texture and microstructure of the electroformed pure Fe varied with electrodeposition current density. The pure Fe film deposited at 2 A/dm^2 showed a strong ⟨1 1 1⟩//ND texture with the average grain size ~4 μm and the most uniform degradation. After annealing at 550 °C, the YS and UTS decreased to 270 ± 6 MPa and 292 ± 14 MPa, respectively, while its ductility improved to 18.4 ± 4%, which was better than the as-cast pure Fe [265] (Table 6). Both static and dynamic *in vitro* degradation tests indicated a faster corrosion rate of the electroformed pure Fe than that of as-cast pure Fe, which could be attributed to the fine-grain structure and structural defects in electroformed pure Fe [265,280].

Nie et al. [266] found that nanocrystalline pure Fe prepared by the ECAP technique exhibited superior strength and much stronger corrosion resistance than that of commercial pure iron (Table 6). Increasing ECAP pass resulted in higher strength and decreased degradation rates as well as improved uniform degradation behavior of the pure Fe. In addition, the nanocrystalline pure Fe better stimulated the proliferation of L929 and ECV304 cells, while inhibited the viabilities of VSMCs.

In order to achieve a faster degradation rate of pure Fe, a variety of secondary phases were added into Fe matrix to generate micro-galvanic corrosion between Fe matrix (anode) and secondary phases (cathode). Tungsten (W) and carbon nanotubes (CNTs) are conductive and act as superior cathodes. Fe_2O_3 is one of the main compositions of degradation products of Fe. Recently, three kinds of Fe based composites (Fe–W, Fe–CNT, and Fe–Fe_2O_3) were prepared by spark plasma sintering (SPS) technique. The addition of three kinds of reinforcement could significantly improve the ultimate compressive strength (981–1256 MPa) of Fe (813 MPa) without weakening the ductility of Fe (~40% for all composites). Furthermore, the addition of W or Fe_2O_3 only slightly enhanced the degradation rate (2.8 μg/cm^2/h) in comparison to pure Fe (2.62 μg/cm^2/h), while the addition of CNT increases obviously (4.3 μg/cm^2/h) [268].

Chou et al. [281] fabricated Fe–30Mn BM scaffolds by 3D printing, which maintained an open porosity of 36.3% and formed a mixed phase alloy of martensitic ε and austenitic γ phases. Despite the presence of high open porosity, the printed scaffolds demonstrated tensile mechanical property values very similar to those of natural bone and appropriate for low load-bearing applications, such as craniofacial scaffolds. Electrochemical corrosion tests showed the 3D printed Fe–Mn desirably corrode significantly more rapidly than pure iron. Cell viability testing of MC3T3-E1 seeded directly onto the Fe–Mn scaffolds and demonstrated good *in vitro* cytocompatibility compared to tissue culture plastic. It indicated that 3D inkjet printing is a promising method for the fabrication of other BMs.

4.2. Surface modification of Fe-based biodegradable metals

Only three related literatures [282–284] are available, and claimed to slow the degradation of Fe as well as improve the surface biocompatibility by modifying the surface, as opposed to the above-mentioned strategy of development of new Fe-basedBMs (i.e. to accelerate its biodegradation rate). Zhu et al. [282] prepared Fe–O thin films on pure Fe by plasma immersion ion implantation and deposition (PIIID). It indicated that Fe–O film fabricated under low oxygen flux effectively reduced the degradation rate of pure Fe. Besides, Fe–O film reduced the number of adhered platelets, restrained the activation of platelets, and favored the adhesion and proliferation of HUVECs. Zhu et al. [283] also implanted lanthanum ion into pure Fe and obtained a similar effect on the degradation and biocompatibility of pure Fe compared to the Fe–O film. In addition, pure Fe was modified by plasma nitriding and the nitride layer, which was composed of epsiv-$Fe_{2-3}N$ and gamma-Fe_4N and greatly decreased its degradation rate [284].

4.3. Animal testing on Fe-based biodegradable metal implants

Table 7 summarizes the literature on animal tests for biodegradable Fe stents to present. In 2001, Peuster et al. [285] evaluated the feasibility of Fe stents (99.8%) by implanting stents into the descending aortas of New Zealand white rabbits. A continuously intact endothelial surface was found on the implanted stent without thrombus formation. Similar luminal area was observed and then compared with the native descending artery during the following six to eighteen months. There was pronounced accumulation of degradation products at the junctions

Table 7
Summary of animal tests for Fe-based biodegradable metals.

Material	Animal model	Duration	Findings	Ref.
Pure iron stent	Rabbits, descending aorta	6–18 months	No thrombogenicity, no significant neointimal proliferation and systemic toxicity, faster degradation at junctions of the stent; locally discoloration of intima	[285]
Pure iron stent	Porcine, descending aorta	360 days	Complete coverage of neointima after 14 d; accumulation of degradation product adjacent to the stent struts and within adventitia accompanied by macrophages; disintegration of struts after 1 year with large portions of the stent residue; no sign of iron overload or iron-related toxicity	[77]
Pure iron stent	Porcine, coronary arteries	28 days	Locally discoloration of the vascular wall adjacent to the stent; degradation was evidenced at 28 d; similar vessel parameters to Co–Cr stent	[286]
Pure iron wire	Rat, artery lumen or artery matrix	1–9 months	Fe wire experienced substantial corrosion within artery matrix, whereas experienced minimal biocorrosion in blood-contacting environment	[287]
Nitrided iron stent	Porcine, iliac arteries	12 months	A nearly intact endothelial cells layer formed on the stented vessel wall; a decreased inflammation scoring, ~30% loss of in-stent luminal diameter, ~47% reduced strut thickness and corrosion product accumulation 12 months postimplantion	[269]

of the stent struts, resulting in slightly elevated vessel walls and a focal brownish discoloration of the intima [285]. Later on, they evaluated the long-term biocompatibility of pure Fe (>99.5%) stent in the porcine descending aorta for 360 d in comparison with 316L SS stents [77]. The results were in agreement with those reported in 2001. No signs of Fe overload or Fe-related organ toxicity were found and the amount of neointimal proliferation from Fe stents was comparable with that from 316L SS stents. Moreover, Waksman et al. [286] explored the short-term safety and efficacy of pure Fe stents in porcine aorta and found no significant differences in any of the vascular, inflammatory, and healing parameters measured between Fe and Co–Cr stent groups.

Mueller et al. established a small animal model to evaluate the potential of iron as a degradable implant material [288]. The rolled Fe foils were inserted into the tails of mice. Histological and gene expression analysis showed that iron implants degraded slowly and lead to a mainly local accumulation of iron deposits that was accompanied by a limited inflammatory reaction without indications of toxic effects.

Pierson et al. [287] developed an arterial wire implantation model by implanting Fe wire into rat artery lumens or artery walls to simulate different arterial environments, (i.e. stent blood contact and stent matrix contact). Substantial corrosion of Fe wire within the artery wall was found in both short-term and long-term degradations whereas blood-contacting wire implants were preserved from corrosion. Besides, bio-corrosion products of the Fe wire retained within the encapsulating neointima in an expanded form.

Wu et al. [289] implanted eight iron stents into the coronary artery of eight healthy mini-swine for four weeks using eight Vison stents as a control. The neointimal proliferation of iron stents was similar to that of Vison stents. There were no thrombosis, inflammation, or necrosis in both groups. Percentage of neointimal coverage measured by SEM was 84% and the stent strut coverage measured by optical coherence tomography (OCT) was 99%.

Feng et al. deployed bio-corrodible nitrided iron stents in juvenile pig iliac arteries. After one month, a nearly intact layer of endothelial cells formed on the stented vessel wall. At three or six months post-operation, the stented vessels remained well patented [269].

5. Other biodegradable metals

5.1. 5.1 Zn-based alloys

Vojtěch D et al. [290] prepared binary Zn–Mg alloys containing Mg content up to 3 wt.% for medical applications, and found that the addition of 1 wt.% Mg significantly improved the mechanical properties of pure Zn (from UTS ~30 MPa, Elong. ~0.25% to UTS ~110 MPa, Elong. ~1.75%) while higher Mg content reduced the mechanical properties. Pure Zn and binary Zn–Mg alloys exhibited close corrosion rates (~0.018–0.145 mm/yr), which were significantly lower than those of Mg and AZ91HP alloys. Wang et al. [291] fabricated the Zn–Mg alloys with Mg content being 35, 40 and 45 wt.%, and found that the micro-hardness of Zn–Mg alloys increased with the decreasing Mg content and the increasing cooling rate. Zn–40Mg alloy exhibited better corrosion resistance than the other two alloys.

5.2. Tungsten

Tungsten has been explored for its versatility as an embolic material for the occlusion of neurysms and tumor-nourishing vessels [292,293]. Tungsten is also considered to be degradable due to the fact that an elevated level of tungsten in both blood and urine were induced after the implantation of tungsten embolization coils in patients [292]. To evaluate the local or systemic toxicity of tungsten, Peuster et al. [293] implanted tungsten coils into sub-clavain arteries of New Zealand rabbits. They found that the corrosion of tungsten coils led to a steady increase in serum tungsten levels starting as early as 15 min after implantation. The mean serum tungsten level rose from 0.48 μg/l to 12.6 μg/l after four months of implantation while no associated local or systemic toxicity was observed. In addition, Peuster et al. [294] also assessed the *in vitro* degradation kinetics and cytoxicity of tungsten coils on human cells. Only very high (>50 μg/l) tungsten concentrations resulted in local cytopathological effects on human endothelial, smooth muscle cells, and human dermal fibroblasts. However, tungsten degrades rather slowly (29 μg/day [294]), which may only be suitable for very small volumes of implant applications.

5.3. Ca-based, Sr-based and Zn-based bulk metallic glasses (BMGs)

Besides the Mg-based BMGs, Ca-based, Sr-based, and Zn-based BMGs have also been developed as candidates for biodegradable metals.

Wang et al. [58] reported that the low concentrations (~10–30%) of $Ca_{65}Mg_{15}Zn_{20}$ BMG extract benefited the viability and growth of different cell lines, including L-929, MG63, VSMC, and ECV304 cells, while high concentrations led to apoptosis of MG63 cells. Moreover, the degradation rate of $Ca_{65}Mg_{15}Zn_{20}$ BMG varied dramatically from the *in vitro* to *in vivo* test, which dissolved within 3 h in Hank's solution but degraded in ~4 weeks inside the medullary cavity of the mouse [58]. Even osteolysis (because of the rapid degradation), endosteal new bone formation, and appropriate inflammatory response were observed in certain regions.

Recently a $Ca_{48}Zn_{30}Mg_{14}Yb_8$ BMG was developed with fracture strength (600 MPa) significantly higher than that of $Ca_{65}Mg_{15}Zn_{20}$ BMG (364 MPa) [295]. In addition, it exhibited a low degradation rate without observable hydrogen evolution and maintained the mechanical integrity after 30 d immersion in Hank's solution.

Li et al. [296] reported several CaLi-based BMGs ($Ca_{65}Li_{6.46}Mg_{5.54}Zn_{23}$, $Ca_{65}Li_{7.54}Mg_{6.46}Zn_{21}$, $Ca_{65}Li_{9.96}Mg_{8.54}Zn_{16.5}$, and $Ca_{65}Li_{14.54}Mg_{12.46}Zn_8$), which showed ultralow density (<2 g/cm^3), and polymer-like thermoplastic formability at near-room temperature. However, these CaLi-based BMGs degraded rapidly, dissolving completely in water in 791 h.

Zhao et al. [297] fabricated three Sr-based BMGs ($Sr_{60}Mg_{18}Zn_{22}$, $Sr_{60}Li_5Mg_{15}Zn_{20}$, and $Sr_{40}Mg_{20}Zn_{15}Yb_{20}Cu_5$) and found that the degradation behavior of Sr-based BMGs could be adjusted by micro alloying using elements Cu, Yb, and Li. $Sr_{40}Mg_{20}Zn_{15}Yb_{20}Cu_5$ BMG exhibited the appropriate compression properties (408.2 ± 20 MPa, 4%) and slowest degradation rate among the stuided Sr-based BMGs [298].

Jiao et al. developed Zn-based BMGs [299] and found that Zn-based BMG with composition of $Zn_{38}Ca_{32}Mg_{12}Yb_{18}$ shows a slower degradation rate than pure Mg and that hardly any hydrogen is generated during the immersion time. Its compression fracture strength did not show obvious decline after being immersed in Hank's solution for 30 d. Cytotoxicity tests revealed that this Zn-based BMG shows good cytocompatibility to MG63 osteoblast cells.

For most of the above-mentioned biodegradable BMGs, their fast corrosion rate in physiological environments is a limit for further clinical application. Surface modification is an effective method for slowing down the corrosion rate of biodegradable BMGs. For example, Li et al. [300] introduced fluoroalkylsilane (FAS) coating, pure Fe film and (Fe + FAS) bilayer on the surface of $Ca_{60}Mg_{15}Zn_{25}$ BMG, and found that these coatings are quite effective to retard the biodegradation.

6. Design and processing of BMs — from raw materials to final medical devices

All steps are inseparable from selecting the materials, processing them into semi-products, designing devices, and manufacturing to the performance of the device in its final form as an implant. As a result, an integrated investigation for the material, design, and performance of the device is needed for BMs, as illustrated in Fig. 8 with a generalized system design chart.

6.1. Design and processing of BM raw materials into semi-products

6.1.1. Alloy design of BM by theoretical calculation

The computer-aided design can provide valuable information and guidance to the experimentalists for implementing appropriate experimental designs and alloy development strategies at reduced time and cost.

Velikokhatnyi et al. [301] used the density functional theory implemented in the Vienna Ab-initio Simulation Package to investigate the effects on thermodynamics of the overall reaction of the alloy with pure water by introducing different alloying elements (Ca, Zn, Y, Al, and Fe) into Mg crystal lattice. The results showed that Fe and Zn retarded the hydroxide film formation at the metal surface but, because of the relatively low chemical and structural stability of the film, the corrosion characteristics of these alloys under physiological conditions deteriorated with respect to undoped Mg. Alloying with Ca, Y and Al helped form a more stable and chemically less reactive hydroxide protective film due to the stronger cohesive energy, possibly better stabilizing the alloys with stronger corrosion resistance.

Based on DFT calculations, Muzyk et al. [302] performed analyses of the roles of 13 alloying elements in terms of their effects on the generalized stacking fault energies of three slip systems – (0 0 0 1) [1 1 2 0], {1 −1 0 0} [−1 −1 2 0], and (0 0 0 1) [1 1 0 0] – in Mg alloys. The highest reductions of unstable stacking fault energy (γ_{USF}) and stacking fault energy (γ_{SF}) are observed in

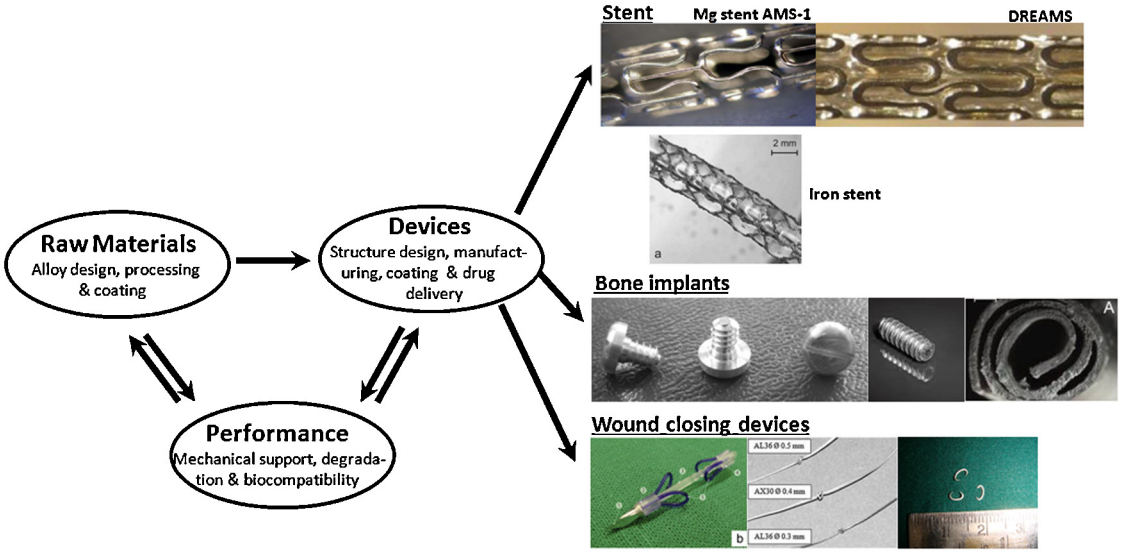

Fig. 8. Generalized materials, systems design chart for biodegradable Mg alloys designed for biomedical applications.

the alloys with Pb and Sn, which greatly decrease the energy barrier for partial dislocations and stacking fault formations. The highest energies of γ_{SF} were found for Mg alloyed with Ag, Cu, Fe, Mn, Ni, Ti, and Zr. The most pronounced tendency for emission of partial dislocations and for mechanical twinning is expected for alloying with Al, Ti, Zn, and Zr. These results have potentially important implications for the design of high-strength Mg-based BMs, which generally exhibit low yield strength due to the lack of efficient strengthening mechanisms.

6.1.2. Processing of BM raw materials into semi-products

The subsequent deformation processes, such as extrusion, rolling, and forging, are also known to modify the microstructure and the mechanical properties of given as-cast BMs.

Fig. 9 shows the mechanical and degradation properties of two representative BMs in the cast and wrought state, Mg-based and Fe-based BMs. The wrought Mg-based BM reveals improved yield tensile strength and elongation to fracture than that of the as-cast Mg-based BM counterpart. The severe plastic deformation (SPD) techniques can further refine the microstructure of Mg-based BMs with the final grain size of several micrometers and improved ductility. The deformation process also benefits the degradation behavior of wrought Mg-based BM with a given composition. The degradation rate drops to a relatively lower value and varies in a small range compared to the as-cast Mg-based BM as shown in Fig. 9(b). However, the SPD techniques contribute little to the degradation behavior compared to the wrought Mg-based BM.

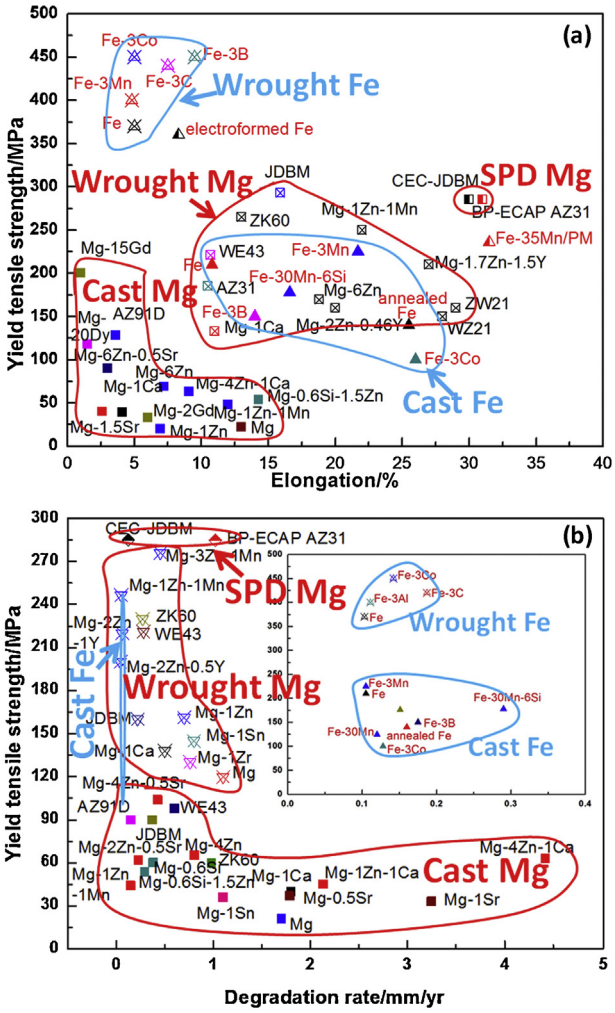

Fig. 9. The (a) mechanical properties and (b) degradation rate of cast and wrought Mg alloys in Hank's solution at 37 °C [89,93,94,98,95,303–305]. The deformation process here includes hot extrusion and rolling.

For Fe-based BMs, the deformation process (rolling in this case) also increases the strength of as-cast Fe-based BMs but deteriorates the ductility and contributes little to the degradation behavior. The workability of Fe-based BMs, in general, is quite good and the process technology is well-established. For example, various high quality pure iron wires, plates, foils, micro-foils, tubes, and rods with various diameters/thicknesses are commercially available in tons. In contrast Mg-based BMs shows limited ductility and poor workability at room temperature because of the hexagonal crystal lattice [82]. Currently the studies on the formability of small sized semi-products that are made of Mg-based BMs (i.e. wires and tubes) are quite limited.

(1) Wires: Wires made of pure Mg (99.99% purity) with a diameter of about 0.1 mm for biomedical applications (sutures, knots) have been reported in 1920 by Seelig et al. [7]. Recently pure Mg (99.95% purity) and AZ31 wires, with the smallest diameter of 0.4 mm, have been fabricated through the extrusion and drawing process [306–308]. The extruded AZ31 wires with 2 mm in diameter were drawn through several passes and annealed at a temperature higher than 200 °C at each pass [308]. Seitz et al. [309] produced the Mg wire (ZEK100 (Zn 1 wt.%, RE 0.5 wt.% and Zr 0.5 wt.%), AX30 (Al 3 wt.% and Ca 0.8 wt.%), AL36 (Li 6 wt.% and Al 3 wt.%), and Mg–0.8Ca (Ca 0.8 wt.%)), with diameters of 0.5, 0.4, or 0.3 mm by a wire-extrusion process from a pre-extruded bars (30 mm in diameter) at 300–450 °C. The extruding forces varied within 600–800 kN. For the drawn and extruded Mg wires, they exhibited dramatically refined grain sizes and improved tensile strength of 300–400 MPa [308,309]. However, the dramatically reduced ductility was observed from drawn AZ31 wires, extruded ZEK100, and Mg–0.8Ca wires. The resulting extruded AX30 and AL36 wires exhibited elongation values close to those wires forming extruded profiles (~10%), which were able to form tight knots. Additionally, $Mg_{67}Zn_{28}Ca_5$ BMG wires with great surface quality were produced via a melt-extraction setup that was designed in-house [148]. These wires exhibited a tensile strength of 675–894 MPa with a characteristic strength of 817 MPa and a Weibull modulus of 20.6 GPa. Moreover, the 99.99% pure Mg wire with 0.2 mm in diameter could be produced [310].

(2) Tube: The requirements in stent applications challenge the manufacturing of mini-tubes made of Mg-based BMs. A numerical simulation has been analyzed by software from MSC/Superform to form thin-wall tubes made of AZ31 using forward extrusion through hollow casting ingots in order to appropriately choose three major processing parameters: cone angle of female die, friction coefficient, and extrusion ratio. Tubes with the length of 1.5 m, diameter of 20 mm, and two wall-sizes (1.5 mm and 0.6 mm) were experimentally fabricated [311]. Lin [312] prepared two kinds of WE43 tubes (3 mm in diameter and 1 mm in wall thickness; 2 mm in diameter and 0.5 mm in wall thickness) through several extrusion passes. In addition, WE43 mini-tubes with the diameter of 1.7 mm and the wall-size of 0.15 mm are commercially available from VASCCOTUBE [313].

6.2. Design and manufacturing of BM medical devices

6.2.1. BM device design

The BMs are potentially adopted for manufacturing cardiovascular stents, bone implants, and wound closing devices, as shown in Fig. 9. In cases where implants are expected to bear mechanical loads, the designs of BM biomedical devices are particularly challenging given the local corrosion profile of BM, complex device geometries, and the loading conditions to which they are subjected.

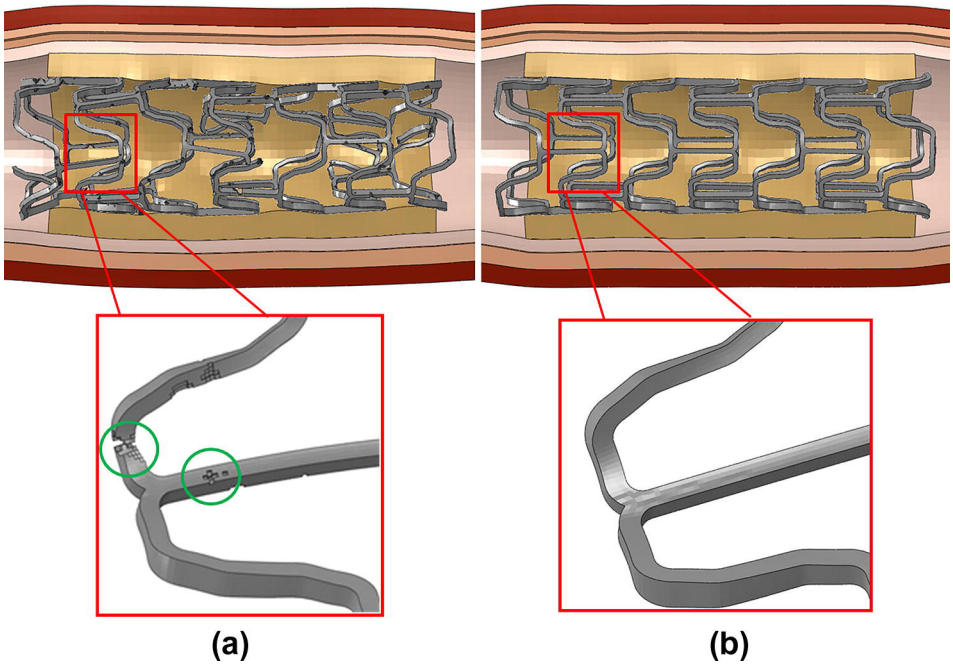

Fig. 10. Finite element simulation results for (a) pitting corrosion and (b) uniform corrosion processes in a biodegradable metal stent in a geometrically ideal artery geometry. It is observed that pitting corrosion attack leads to a non-uniform breaking down of the stent geometry, with a localized attack predicted to occur, as circled, in (a) [319].

6.2.1.1. Finite element analysis. A number of finite element analysis (FEA) studies have investigated the performance of BM stents, to predict stent performance, stress distribution after expansion and associated degradation process in the vessels aiming to optimize the stent design. Grogan et al. [314] compared the performances of Mg alloys, Fe and permanent metallic stents using three stent designs: Generic [315] for permanent metallic stent, Magic stent [260] for Mg, and PUVA stent [285] for Fe. Mg and Fe stents were predicted to exhibit less than 20% and 50% of respective maximum allowable device curvatures. Less than 50% of resistance to longitudinal compression was expected from the permanent metallic stents. To achieve comparable radial strength and recoil of Co–Cr stent, the struts of the Mg and Fe stents require 2.4 and 1.5 times greater cross-sectional areas. Similar results also reported that 48% increased strut width could reduce the maximum principal strain and stress as well as enhance the scaffolding ability by 24% in the work of Wu et al. [316].

Computational modeling of the degradation process and the associated mechanical integrity degeneration are also investigated in a FE framework. A continuum damage model was developed for Mg alloy stents considering superposition of stress corrosion and uniform corrosion [317,318]. The former describes the stress-mediated localization of the corrosion attack through a stress-dependent evolution law while the latter affects the free surface of the material exposed to an aggressive environment. As the model depicted, the beginning of Mg alloy degradation was concentrated mainly at the more deformed locations after stent expansion. The degradation proceeded with the mass loss of the outer surface of the stent, associated with the decreasing mechanical integrity of the stent. The optimized Mg alloy stent, with thicker strut than the Magic stent design, showed decreased maximum principal stress after recoil (163 MPa) and increased half normalized time of vessel recoil [318]. Grogan et al. [319] developed a phenomenological corrosion model in a FE framework to predict the loss of stent mechanical integrity using both pitting corrosion and uniform corrosion models. Pitting corrosion attacks led to a non-uniform breaking down of the stent geometry (Fig. 10(a)) while the uniform model in Fig. 10(b) predicted the homogeneity. The experimental results were in good accordance with the numerical results using the pitting corrosion model [319].

6.2.1.2. Device prototypes. (1) *Cardiovascular stent*: Table 8 presents the geometric sizes and properties of different stents. Take the example of a Biotronic Mg alloy stent; it moved from the old-generation AMS to new-generation DREAMS (Fig. 8). The stent strut thickness has been reduced from 165 μm to 125 μm using a modern 6-crown design and the cross section of the stent strut has been changed from rectangular to square, obtaining a higher collapse pressure 1.5 bar than AMS-1. Similar to the FEA results, a NOR-I Fe stent with similar geometric sizes to AMS exhibited much higher supporting strength to the vessels, which is close to the Crossflex stainless steel stent.

Table 8
The geometric sizes of the cardiovascular stents [285,320].

Stent/material	Thickness (μm)	Diameter (mm)	Length (mm)	Recoil (%)	Collapse pressure (atm)
AMS-1/Mg alloy	165	3.0, 3.5	10, 15	<8	0.8
AMS-2, DREAMS/Mg alloy[a]	125	3.0, 3.25, 3.5	12, 16, 20	5	1.5
NOR-I/iron	100–120	3–6	16	2.2	3.5
Crossflex/stainless steel	–	3.5	15	–	0.6
NIR Primo/316L	–	3.5	16	–	>1.5
Multi-link Vision/Co–Cr	100	4	15	–	0.9

[a] The shape of the strut in cross-section has been altered from rectangular (AMS-1) to square (AMS-2 and DREAMS).

(2) *Bone implants*: The most popular design of BM bone implants is Mg-based BM bone fixation staples [240] and interference screws [321] (see Fig. 8). For orthopedic applications, the majority of current studies use Mg-based BM in the form of a solid monolith (bar or rod form). Recently AZ31 sheet was spirally wrapped into a hollow, cylindrical scaffold that contained interlayer spaces (Fig. 8). This scaffold design was claimed to be advantageous due to its decrease in weight (about 50%) while maintaining mechanical strength and composite elastic modulus. It also had a hollow cylinder shape similar to cortical bone, and the internal open space will allow the in-growth of tissue that facilitates the removal of degradation byproducts [322].

(3) *Wound closing devices*: With the increasing importance of natural orifice transluminal endoscopic surgery, endoscopy is gradually replacing open surgery in the gastrointestinal tract. Completely degradable wound-closing rivets offer the combined advantages of miniaturizing the system, reducing the extent of intervention, and allowing efficient and secure tissue joining and wound closure. Several kinds of Mg-based BM wound closing devices, such as sutures, microclips and rivets, have been prototyped, as shown in Fig. 8. For example, a microclip for laryngeal microsurgery was designed with the bioabsorption within two weeks and made of pure Mg and poly-e-caprolactone (PCL)-coated pure Mg [323]. The Mg microclip could be deployed rapidly using modified 2-mm micro-laryngeal cup forceps, which enables the clip to close in a circular shape. *In vitro* and *in vivo* tests showed this clip held securely to the vocal fold mucosa. Macroscopic and histological studies showed no significant injury to the contralateral vocal fold [324].

6.2.2. BM device manufacturing

It is well known that the surface characteristics play a critical role in determining the performances of BMs. Thus, in this respect, the fabrication process used to manufacture devices needs to be especially concerned. This procedure could alter the chemistry of BM surfaces or introduce defects/contaminants and, thereby inadvertently alter the implant performance.

Some studies have been conducted on the machining and polishing of Mg-based BMs, given their high chemical activity and relatively soft matrix, which might easily change the surface chemistry.

(1) *Machining*: The machining of functional elements such as holes and threads of orthopedic implants is usually required using wire electro discharge machining (EDM), turning, or milling techniques. The generated heat is one of the main problems for Mg-based BMs machining that may lead to ignition of the chips. Guo et al. [153] reported a safely performed high speed dry milling for an Mg–0.8Ca alloy using polycrystalline diamond (PCD) tools with process characteristics of lamella structured chips and slight flank build-up. In turning AZ91, no adhesion on flank face occurred using carbide tools coated with PCD compared to uncoated and TiN-coated carbide tools [151]. This is related to lower friction between PCD coating and Mg plus the higher thermal conductivity of PCD, which caused lower heat generation and faster heat conduction from the cutting edge zone, respectively. Additionally, several kinds of coolants are used to reduce the surface temperature on Mg alloys. In contact with water-based coolants, Mg tends to have chemical reactions and forms hydrogen, which is extremely flammable. Oil-based lubricants introduce the danger of oil mist explosions. However, Salahshoor et al. [154] used the dual-purpose oil serving as both lubricant and coolant during the ball burnishing process on the Mg–0.8Ca alloy, which can effectively reduce the temperature indicating only a 5–6 °C increase in the applied pressure range. Pu et al. [156] compared the influence of dry and cryogenic machining (spraying the liquid nitrogen on the machined surface) using different cutting edge radius tools on the surface integrity of AZ31B and found that the cryogenic machining with a large cutting edge radius could lead to the desired surface finish. Besides, Klocke et al. [325] reported the wire electro discharge machining technique for WE43. The applied trim cut with sequential decreasing discharge energies could effectively improve the surface integrity and reduce the surface roughness.

(2) *Laser machining or laser cutting:* Very few reports could be found on the laser cutting of Mg-based and Fe-based BMs. Without surface coatings to raise absorption of laser beam, extruded AZ31 sheets of 1 mm thickness were able to be successfully cut by a carbon dioxide laser at the condition of beam power 400 W and feeding speed 25 mm/s [326]. The average height of drosses was about 300 μm when feeding speed was larger than 12 mm/s. Furthermore, by using argon as assist gas, processing damages like cracks and pores were inhibited. However, the oxidation of laser-cut surfaces was not depressed perfectly; some oxides were observed in drosses and at the top edge of cut surfaces. The thickness of the melted and resolidified layer was 7 μm at the upper part of cut surface and 24 μm at the lower part. The re-solidified layer consisted of two thin layers at the lower part of the cut surface. Refined pores less than 1 μm were observed at the interface of these two layers [327]. Additionally, Peuster et al. [285] applied the laser cutting in a nitrogen atmosphere to prevent the corrosion of Fe stents.

(3) *Polishing*: The finishing process of a BM surface is important to increase the quality of products. Electropolishing is usually performed to remove burrs and mechanical defects resulting from the heat ablation of the laser cutting, etching, and forming steps and to achieve a smooth product surface. Magnetic abrasive polishing (MAP) has been verified on the AZ31 with an improving strategy of the magnetic force with a permanent magnet [327], since it equipped with flexible tool including iron powder and abrasive particle. Not only is the cutting force and generated temperature lower than other machining processes, it is also possible to polish the free surface of products.

(4) *Sterilization*: The available reports on sterilization methods include disinfecting of Mg- or Fe-based BM implants by ethylene oxide before implantation [243], sterilizing by exposure to γ-radiation (25 kGy, 6–8 h) [108,240,285], and UV radiation (30 min in a Procleaner device) [287]. There was a recent comparative study on the effects of various sterilization methods on surface characteristics and biocompatibility of pure Mg and Mg–Ca alloys [328], including steam autoclave sterilization, ethylene oxide steam sterilization, glutaraldehyde sterilization, dry heat sterilization and Co60 γ-radiation sterilization technologies. It indicated that Co60 γ-radiation sterilization comprehensively minimizes the effects of the sterilization process on the surface chemistry and consequent biocompatibility; thus, it is believed to be the optimal sterilization method for Mg-based BMs.

7. Concluding remarks and perspectives

7.1. What are the ideal biodegradable metal devices

The performance criteria of an ideal BM device should perfectly match the injured tissue reconstruction process in terms of providing temporary mechanical support mimicking the near-term performance of traditional metallic implants and completely dissolve in longer time frames with an appropriate degradation rate tolerable for the human body.

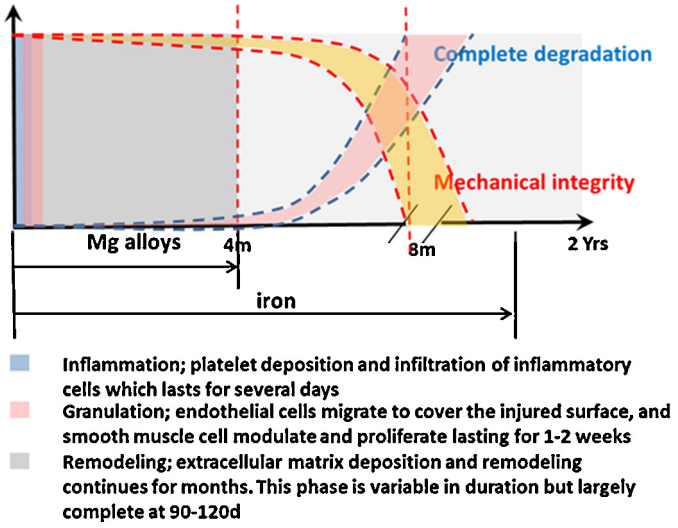

Fig. 11. The schematic diagram of degradation behavior and the change of mechanical integrity of BM stents during the vascular healing process.

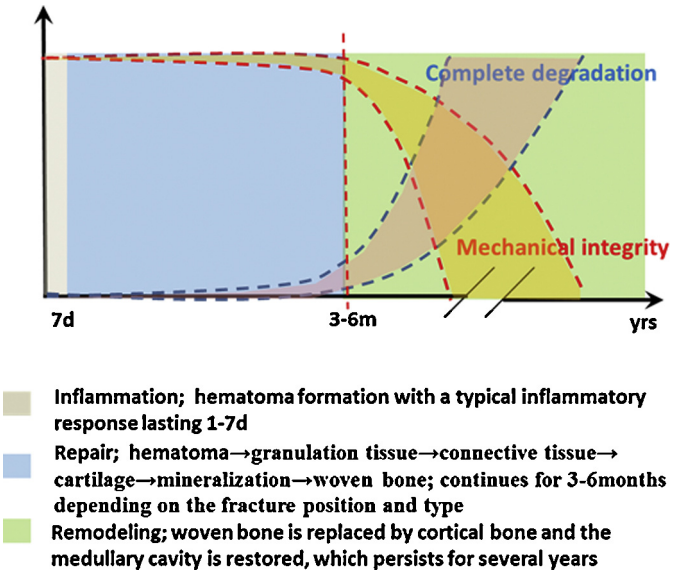

Fig. 12. The schematic diagram of degradation behavior and the change of mechanical integrity of BM implants during the bone healing process.

For cardiovascular applications, vascular injury is common and often extensive following balloon angioplasty. The injured vessels exhibit a wound healing response that can be described in three overlapping phases: inflammation, granulation and remodeling [329], as shown in Fig. 11. A complete degradation is expected to occur after the vessel remodel phase which is usually completed at 90–120 d. Serruys et al. [330] observed that "almost all lesions deteriorated to some extent by 120 days post-coronary angioplasty" and the minimal luminal diameter tended to stabilize after the three month follow-up in 342 patients. Hence, a very slow degeneration of mechanical support is expected in the first ~4 months providing sufficient support to the injured vessels. Even though experts still debate whether full mechanical support in stented lesions is mandatory during the first four months after implantation, it would certainly be wise to use this clinical opinion as a safety design parameter and a benchmark for market approval evaluations based on the fact that there is insufficient human *in vivo* data available especially for mechanical vessel wall properties during the healing/remodeling phase.

Bone fracture healing occurs in three stages: inflammation, repair and remodeling phases [331,332], as shown in Fig. 12. During the first two to three weeks post-fracture, the soft callus forms which corresponds roughly to the time when the fragments are no longer moving freely. This early soft callus can resist compression, but show similar tensile properties to the fibrous tissue of which the ultimate tensile strength and elongation at rupture are 4–19 N m/mm^2 and 10–12.8%, respectively [332]. Hence the mineralization of the soft callus proceeds from the fragment ends toward the center of the fracture site and forms a hard callus, which has regained enough strength and rigidity to allow low-impact exercise at the end of the repair phases [331,332]. The time to achieve the hard bone union varies greatly according to the fracture configuration and location, status of the adjacent soft tissues, and patient characteristics (e.g. species, age, health status, concurrent injuries/diseases). According to Perkin's classification of fracture healing, a spiral fracture in the upper limb unites in three weeks and consolidates in six weeks. The fracture healing time doubles for a transverse fracture and doubles again for the lower limb. Table 9 lists a rough estimate of bone healing time for different fractures. Hence, the mechanical support should be sustained for 12–24 weeks depending on the clinical conditions.

Currently, the reported Mg alloy stents and bone implants indicate a relatively faster degeneration of mechanical properties (Tables 4 and 5) before/during the tissue remodeling process than expected. For example, the reported Mg-based BM stents completely degraded within four months and, thus, a much faster loss of mechanical integrity of stent would occur. In the coming future, surface coating could be used as a remedy to extend the mechanical integrity of Mg-based BM stents. In the case of Fe-based BM stents, they exhibit good mechanical support during four months and much slower loss of mechanical integrity of stent would occur. In the near future, research should consider how to accelerate the biodegradation.

7.2. How to use biodegradation byproducts

Biodegradation products are unavoidably formed at the BMs/host interface until the chemical reaction of the BM with the body fluid has reached 100% completion. They should be biocompatible and biosafe to the host tissue at the minimum requirements. Subsequently, the next logical question is how to fully exploit the bio-function of the degradation products. The scientific reports on the biological functions on various typical biodegradation products of BMs (i.e. Mg ions, OH^- ions, MgO particles, hydrogen, Fe particles and Fe oxide particles) might provide some useful hints on the best uses for BMs in the future.

Table 9
Bone healing time for different fractures.

Fracture		Healing time (weeks)
Upper limb	Clavicle	5–7
	Fingers	4–8
	Scaphoid	>10
	Humerus	5–8
	Radius and ulna	8–12
	Distal radius	3–4
Lower limb	Pelvis	6–10
	Femur	8–14
	Neck of femur	12–24
	Tibia	8–12
	Calcaneus	6
	Toes	6–8

(1) Mg ions: Increased Mg levels could stimulate new bone growth. Numerous studies on various Mg alloys have reported enhanced bone growth around the corroding Mg implant [7,78,108,194,242]. Park et al. [333] compared the bone healing capacity of an Mg ion-incorporated porcine bone prepared with hydrothermal treatment in an alkaline Mg-containing solution in the rabbit calvarial defect with untreated porcine cancellous bone and deproteinized bovine bone. The Mg-incorporated porcine bone with surface nanostructures achieved rapid new bone formation in the osseous defects of rabbit calvarias compared with untreated xenografts of porcine and bovine origins. Recently pure Mg wires were implanted into femora in STZ-induced diabetic rats [334]. The serum Mg level and bone mineral contents increased significantly and as a result, the bone mineral density in the Mg treatment group was higher than that in the diabetic group. Besides, blood biochemical analysis indicated that Mg implants had no toxic effect on the liver and kidney functions. All of this indicated that the implantation of Mg could stimulate new bone growth and potentially has an anti-osteoporotic activity [334]. Additionally, Slutsky et al. [335] studied the effect of increasing brain Mg using Mg–L-threonate on learning and memory in rat models. Their results suggested that elevating brain Mg enhanced short-term synaptic facilitation and long-term potentiation as well as improved learning and memory functions.

(2) OH^- ion: The effects of Mg metal and increased Mg^{2+} concentration and alkaline pH value on the *in vitro* growth of *Escherichia coli*, *Pseudomonas aeruginosa* and *Staphylococcus aureus* were evaluated [336]. It was found that: (i) as Mg metal corrodes in culture medium, the Mg^{2+} concentration increases parallel to that of the OH^-; (ii) when Mg corrosion products were added to the growth media, the growth of *E. coli*, *P. aeruginosa* and *S. aureus* was inhibited; (iii) the addition of Mg^{2+} alone will not inhibit bacterial growth; But, (iv) increasing the OH^- ions (i.e. higher pH) will inhibit bacterial growth. Moreover, OH^- ion might also influence bone growth *in vivo*. Experiments in rabbits with implanted $Mg(OH)_2$ cylinders have demonstrated enhanced bone remodeling adjacent to the dissolving cylinder [59]. This indicates that either local alkalinity and/or enhanced Mg ion concentration might stimulate bone growth.

(3) MgO: MgO is an ideal biodegradable material to be added into the targeted tissues in nano-cryosurgery with its relatively lightweight property, excellent thermal conductivity, and specific heat. Di et al. [337] studied the temperature response and different damages to the biological tissues loaded with and without MgO nanoparticles (NPs) during the cryosurgical experiment as well as the nucleation-accelerating effect of MgO NPs. The freezing effect of the cryosurgery was highly enhanced, causing more thorough damage to *in vivo* biological tissues when MgO NPs were added during cryosurgery. Furthermore, this study demonstrated that MgO NPs significantly induced lower supercooling degrees when deionized water, physiological saline solution, or biological tissue suspension (*in vitro)* was frozen to nucleation.

(4) Hydrogen: Hydrogen is a stable gas that can react with oxide radical ion ($^{\bullet}O^-$) and hydroxyl radical ($^{\bullet}OH$) in water with low reaction rate constants. Hydrogen, however, is a small molecule that can easily dissipate throughout the body and cells and therefore, the collision rates of hydrogen with other molecules are expected to be very high, which is likely to be able to overcome the low-reaction rate constants. Hydrogen is not easily dissolved in water and 100%-saturated hydrogen water contains 1.6 ppm or 0.8 mM hydrogen at room temperature. A major breakthrough in hydrogen research occurred after Ohsawa et al. reported a prominent effect of molecular hydrogen on a rat model of cerebral infarction in 2007 [338]. The effects of molecular hydrogen on various diseases have been documented for over sixty model and human diseases. Most studies have been performed on rodents including two models of Parkinson's disease and three models of Alzheimer's disease. Protective effects were observed especially in oxidative stress-mediated diseases including neonatal cerebral hypoxia; Parkinson's disease; ischemia/reperfusion of spinal cord, heart, lung, liver, kidney, and intestine; and transplantation of lung, heart, and kidney [339].

(5) Fe particles at nano- and micro-scales: Iron powders have been considered for biomedical applications such as controlled drug release (e.g. an increase in the density of the rumino-reticulum devices (RRDs) to allow the RRDs to remain in the rumino-reticulum during the time for the release of the drug). Iron powders (30–50 μm) were dispersed into poly-(e-caprolactone) and a faster release profile of levamisole was achieved [340]. Nanoscale metallic iron is a new tool for the treatment of contaminated water and soil and can effectively transform a wide array of environmental contaminants including chlorinated solvents, organochlorine pesticides, PCBs, organic dyes, and inorganic pollutants such as perchlorate, nitrate, and heavy metal ions [341,342]. The presence of iron nanowires (Fe NWs, ~50 nm in diameter), which were prepared by electrodeposition within the nanopores of anodic aluminum oxide (AAO) templates, had no significant effect on the cell proliferation and cell viability; even the HeLa cells exposed to Fe NWs at the high concentration of 10,000 per cell for 72 h still showed high cell viability of about 80% [343].

(6) Iron oxides: For the past two decades magnetic nanoparticles (MNPs) such as hematite (α-Fe_2O_3), maghemite (γ-Fe_2O_3), and magnetite (Fe_3O_4) find wide biomedical applications such as MRI contrast enhancement, cellular imaging, and cancer diagnostics [344]. Biocompatibility and saturation magnetization can be obtained for reliable/reproducible superparamagnetic iron oxide nanoparticles with optimum surface charge, shape, size, and colloidal stability. The nature of surface coatings and their subsequent geometric arrangement on the nanoparticles determine not only the overall size of the colloid but also play a significant role in biokinetics and biodistribution of nanoparticles in the body [345]. Therefore, various iron oxides may be used in composites with iron powders to enhance its biodegradation rate. This may shift the original surface chemistry techniques on iron oxides to the surface treatment of Fe-based BMs to enhance the biodegradation rate and reach a more uniform biodegradation mode.

7.3. Competition with permanent metallic materials and biodegradable polymers

BMs have shown encouraging results when used as both hard and soft tissue scaffolds, especially in comparison with the permanent metallic materials used over decades (Table 10), including stainless steel, Ti alloys and Co-based alloys. Recently there was a prospective, randomized, clinical pilot trial [349] to determine if Mg-based BM screws are equivalent to standard titanium screws for fixation during chevron osteotomy in 26 patients with a mild hallux valgus, and six month follow-up included clinical, laboratory, and radiographic assessments revealed that they were equivalent. Out of question, there is still a long way to go for BMs to be widely used in clinical settings. The choice between degradable and non-degradable metallic devices must carefully consider many factors, such as patient age (child or adult) and personal physical condition, the type of fracture, the risk of infection, etc. Clearly, the improvement of the mechanical

Table 10
Comparison between permanent metallic materials and biodegradable metals.

Items	Permanent metallic materials	Biodegradable metals
Mechanical property	Stable over time	Degraded with the time, and should match the tissue recovery process
Ion release	Unwanted, try to avoid	The released metal ions should be acceptable by the host locally and all over the body
Interaction with the surrounding tissue	Bio-inert	Bio-active
Application fields	Ubiquitous	Special applications

properties and more predictable degradation behaviors of BM devices will be helpful for broadening their use.

Several polymers already have a long history as degradable materials for biomedical and pharmaceutical applications. Resorbable sutures, for example, have been commercialized for decades before biodegradable devices for osteosynthesis were available [346]. Today, degradable polymeric devices for osteosynthesis are successful in low or mild load bearing applications. There are many biodegradable polymers that have been approved by the FDA, including LPLA, DLPLA, PGA, and PCL [347]. These polymers have been used for FDA approved products as fracture fixation pins and plates, interference screws, suture anchors, craniomaxillofacial fixation devices, and tacks for meniscal repair [346].

BMs have been viewed as the promising alternative to biodegradable polymers for hard tissue repair. Taking the interference screws comprised of biodegradable polymers as an example, the degradation rate of polymer screws is not well controlled, with some screws showing limited degradation after three years of insertion. Additionally, polymer screws exhibit an increased occurrence of breakage upon screw insertion. Polymers that completely degrade in bone within a year or two usually exhibit poor biocompatibility, which can adversely affect osseointegration and result in bone tunnel widening. In contrast, the advantages of BM screws appear; through the use of alloying and coating, BM screws can be designed to degrade at a controllable rate. Upon degradation, the screws are replaced by native tissue, eliminating the need for additional surgeries to remove the implants. Additionally, BM has superior mechanical properties compared to polymer, resulting in a reduction of surgical complications associated with breakage. Moreover, the BM would form a weak base microenvironment around the implant instead of the acidic degradation products of polymer (e.g. PLA), which would induce strong host inflammatory reaction.

All in all, the beginning competition between permanent metallic materials and BMs is relatively low, however, it can be conjectured that the competition between BMs and biodegradable polymers might be relatively high.

7.4. Challenge and future R&D direction for BM

The successes on the clinic trails of Mg-based BMs within bone [349] and blood vessel [261] in 2013 were the important milestones on the way to push the class III BM implants into the final medical market with the official approvals such as FDA, SFDA, and CE. Currently, there are still several obstacles in the present evaluation methods preventing broad and straightforward market access to BMs. The majority of these obstacles are based on the fact that most standard tests are designed for permanent implant materials, biodegradable polymers, or ceramics (e.g. EN ISO standards). A common requirement for standardization (in compliance with the requirements of ISO or ASTM) is the availability of experimental approaches that are highly reproducible across different laboratories and companies. To achieve this level of reproducibility, specific experimental procedures and study designs for BMs need to be established in the academic and industrial world [348].

The future research and development direction of BMs may lean toward "multifunctional capabilities" (e.g. providing a temporary implant material with both structure of traditional metallic biomaterials; new BM bio-function as revolutionized metallic biomaterials). The new biological functions originate from the biological and physiological function of various biodegradation products of BM in a controllable manner to benefit the local tissue reconstruction. In addition, the combination/integration with other biomaterials, especially the biodegradable ceramics and polymers with advanced techniques for materials fabrication will be a promising direction for future development of BMs. Wong et al. [350] developed a new biodegradable composite composed of polycaprolactone and magnesium. By incorporating magnesium micro-particles, the compressive moduli of the composites can be adjusted to be within the range of the human cancellous bone. *In vitro* studies indicate that the silane-coated Mg/PCL composites have excellent cytocompatibility and osteoblastic differentiation properties.

Besides serving as the raw materials for manufacturing the traditional passive implantable medical device, BM may have promising new opportunity as the candidate materials for fabricating active implantable medical device. A pioneer work [351] uses magnesium (Mg) for the conductors, magnesium oxide (MgO) (silicon dioxide, SiO_2, is also possible) for the dielectrics, monocrystalline silicon (Si) nanomembranes (NMs) for the semiconductors, and silk (which is watersoluble and enzymatically degradable) for the substrate and packaging material; Mg/MgO inductors, Mg/MgO capacitor, Si/MgO/Mg transistor, Mg resistor, Mg interconnect and Mg electrode had been fabricated as the new-concept implantable transient electronic device. Inductive coils of Mg combined with resistive microheaters of doped Si NMs, integrated on silk substrates and housed in silk packages, had provided transient thermal therapy to control surgical site infections as a nonantibiotic, programmable bacteriocidal appliqué. In the future, various transient electronic components, circuits, and sensors, including simple integrated circuits and sensor arrays might be designed with BMs, and they would function for medically useful time frames but then completely disappear via resorption by the body.

In comparison to the traditional bioinert metallic biomaterials, the BM can be classified into "bioactive" biomaterials, and should develop toward the "third-generation biomedical materials" [352]. BM will play a more active role once implanted, not simply as a tissue engineering scaffold. A direct and active interaction with the host would happen for BM during its service life; the interface between the BM implant and the host always keeps a dynamic balance and the host-biodegradation-products-BM double interfaces change all the time until final biodegradation of the BM. Besides providing the mechanical support during the initial degradation stage, the continuous chemical productions of various biodegradation products will stimulate the host to response, and more importantly will help the body heal itself. The mechanical, chemical and biological interactions mix together and proceed as the functions of time and space, until one hundred percentage of the repair and regeneration of tissues.

Undoubtedly, biodegradable metals are the rising stars as the next generation of metallic biomaterials. There are still a lot of unknowns about BM and there are plenty of R&D works to commercialize BM medical devices. With the collaboration of material scientists and medical doctors, there will be more new BM candidates developed with unexpected properties, which may provide new opportunities to promote both the fundamental research and their applications.

Acknowledgements

This work was supported by the National Basic Research Program of China (973 Program) (Grant no. 2012CB619102 and 2012CB619100), National Science Fund for Distinguished Young Scholars (Grant no. 51225101), Research Fund for the Doctoral Program of Higher Education under Grant no. 20100001110011, National Natural Science Foundation of China (no. 31170909), the NSFC/RGC Joint Research Scheme under Grant No. 51361165101 State Key Lab of Advanced Metals and Materials (Grant no. 2011-ZD01), State Key Laboratory for Mechanical Behavior of Materials (Grant no. 20111210), Beijing Municipal Science and Technology Project (Z131100005213002) and Project for Supervisor of Excellent Doctoral Dissertation of Beijing (20121000101) and Guangdong Province innovation R&D team project (no. 201001C0104669453). YF would like to thank Ms. Huafang Li, Ms Nan Li, Mr. Jian Cheng, Mr. Feiyu Zhou and Mr. Tao Huang at Peking University for their help on the preparation of the manuscript, and thank Dr. Zhigang Xu at North Carolina A&T State University for his suggestive comments and language editing work. FW would like to thank Ms Dandan Hong for her language editing work.

References

[1] R.W. Revie, H.H. Uhlig, Corrosion and Corrosion Control, 4th ed., John Wiley & Sons, Hoboken, New Jersey, 2008.
[2] J. Cheng, B. Liu, Y.H. Wu, Y.F. Zheng, Journal of Materials Science & Technology 29 (2013) 619–627.
[3] B.D. Ratner, A.S. Hoffman, F.J. Schoen, J.E. Lemons, Biomaterials Science: An Introduction to Materials in Medicine, Elsevier Academic Press, New York, 2004, pp. 10–11.
[4] E. Crubzy, P. Murail, L. Girard, J.-P. Bernadou, Nature 391 (1998) 29.
[5] P.G. Laing, ASTM-STP 684 (1979) 199–211.
[6] A. Lambotte, Bulletins et Mémories de la Société National de Chirurgie 28 (1932) 1325–1334.
[7] F. Witte, Acta Biomaterialia 6 (2010) 1680–1692.
[8] E.C. Huse, Chicago Medical Journal and Examiner 37 (1878) 171–172.
[9] E. Payr, Archiv für Klinische Chirurgie 62 (1900) 67–93.
[10] E. Payr, Centralblatt für Chirurgie 28 (1901) 31–37.
[11] V. Chlumský, Mitteilungen aus den Grenzgebieten der Medizin und Chirurgie 3 (1907) 416–451.
[12] E. Payr, Deutsche Zeitschrift für Chirurgie 63 (1902) 503–511.
[13] E. Payr, Zentralblatt für Chirurgie 30 (1903) 233–234.
[14] S. Hoffheinz, N. Dimitroff, Deutsche Zeitschrift für Chirurgie 208 (1928) 346–353.
[15] E. Payr, A. Martina, Archiv für Klinische Chirurgie 77 (1905) 962–998.
[16] E. Sonntag, Ergebnisse der Chirurgie und Orthopädie 8 (1914) 1–156.
[17] E. Glass, Deutsche Zeitschrift für Chirurgie 194 (1926) 352–366.
[18] P. Wilflingseder, R. Martin, C. Papp, Chirurgia Plastica 6 (1981) 105–116.
[19] J. Verbrugge, La Press Medicale 23 (1934) 460–465.
[20] J. Verbrugge, Presse Medicale 55 (1933) 1112–1114.
[21] J. Verbrugge, Bulletins et Mémories de la Société National de Chirurgie 59 (1937) 813–823.
[22] E. McBride, Southern Medical Journal 31 (1938) 508–515.
[23] O. Maier, Deutsche Zeitschrift für Chirurgie 253 (1940) 552–556.
[24] V. Troitskii, D. Tsitrin, Khirurgiia 8 (1944) 41–44.
[25] G. Song, A. Shayan, Corrosion of steel in concrete: causes, detection and prediction, A state-of-the-art review, in: Review Report 4, ARRB Transport Research Ltd., Victoria, Vermont, 1998.
[26] E. Zhang, H. Chen, F. Shen, Journal of Materials Science: Materials in Medicine 21 (2010) 2151–2163.
[27] Y. Xin, K. Huo, H. Tao, G. Tang, P.K. Chu, Acta Biomaterialia 4 (2008) 2008–2015.
[28] R. Ambat, N.N. Aung, W. Zhou, Journal of Applied Electrochemistry 30 (2000) 865–874.
[29] A. Yamamoto, S. Hiromoto, Materials Science and Engineering C 29 (2009) 1559–1568.
[30] L. Xu, S. Zhu, N. Huang, X. Li, Y. Zhang, Journal of Biomedical Engineering 26 (2009) 783–786.
[31] Y. Xin, T. Hu, P.K. Chu, Acta Biomaterialia 7 (2011) 1452–1459.
[32] R. Willumeit, J. Fischer, F. Feyerabend, N. Hort, U. Bismayer, S. Heidrich, B. Mihailova, Acta Biomaterialia 7 (2011) 2704–2715.
[33] R. Rettig, S. Virtanen, Journal of Biomedical Materials Research Part A 85A (2008) 167–175.
[34] C. Liu, Y. Xin, X. Tian, P.K. Chu, Journal of Materials Research 22 (2007) 1806–1814.
[35] A. Kocijan, I. Milošev, B. Pihlar, Journal of Materials Science: Materials in Medicine 14 (2003) 69–77.
[36] D.D. Zabel, S.A. Brown, K. Merritt, J.H. Payer, Journal of Biomedical Materials Research 22 (1988) 31–44.
[37] S. Omanovic, S.G. Roscoe, Langmuir 15 (1999) 8315–8321.
[38] Y.-C. Tang, S. Katsuma, S. Fujimoto, S. Hiromoto, Acta Biomaterialia 2 (2006) 709–715.
[39] M.V. Vinnichenko, M.T. Pham, T. Chevolleau, L.V. Poperenko, M.F. Maitz, Applied Surface Science 207 (2003) 176–182.
[40] X.N. Gu, W.R. Zhou, Y.F. Zheng, Y. Cheng, S.C. Wei, S.P. Zhong, T.F. Xi, L.J. Chen, Acta Biomaterialia 6 (2010) 4605–4613.
[41] K.J. Bundy, C.J. Williams, R.E. Luedemann, Biomaterials 12 (1991) 627–639.
[42] K.J. Bundy, M.A. Vogelbaum, V.H. Desai, Journal of Biomedical Materials Research 20 (1986) 493–505.
[43] J. Lévesque, H. Hermawan, D. Dubé, D. Mantovani, Acta Biomaterialia 4 (2008) 284–295.
[44] Y. Chen, S. Zhang, J. Li, Y. Song, C. Zhao, X. Zhang, Materials Letters 64 (2010) 1996–1999.
[45] B. Liu, Y.F. Zheng, Acta Biomaterialia 7 (2011) 1407–1420.
[46] S. Zhang, X. Zhang, C. Zhao, J. Li, Y. Song, C. Xie, H. Tao, Y. Zhang, Y. He, Y. Jiang, Y. Bian, Acta Biomaterialia 6 (2010) 626–640.
[47] Q. Wang, L. Tan, W. Xu, B. Zhang, K. Yang, Materials Science and Engineering B 176 (2011) 1718–1726.
[48] M.B. Kannan, R.K.S. Raman, Biomaterials 29 (2008) 2306–2314.
[49] M.B. Kannan, R.K.S. Raman, Scripta Materialia 59 (2008) 175–178.
[50] M.B. Kannan, R.K.S. Raman, F. Witte, C. Blawert, W. Dietzel, Journal of Biomedical Materials Research Part B: Applied Biomaterials 96B (2011) 303–309.
[51] M. Niinomi, International Journal of Fatigue 29 (2007) 992–1000.
[52] A. Yamamoto, R. Honma, M. Sumita, Journal of Biomedical Materials Research 39 (1998) 331–340.
[53] F. Witte, N. Hort, C. Vogt, S. Cohen, K.U. Kainer, R. Willumeit, F. Feyerabend, Current Opinion in Solid State and Materials Science 12 (2008) 63–72.
[54] J. Fischer, M.H. Prosenc, M. Wolff, N. Hort, R. Willumeit, F. Feyerabend, Acta Biomaterialia 6 (2010) 1813–1823.
[55] Y. Chen, S.X. Zhang, J.N. Li, Y. Song, C.L. Zhao, H.J. Wang, X.N. Zhang, Materials Science and Engineering B 176 (2011) 1823–1826.
[56] H. Hermawan, A. Purnama, D. Dube, J. Couet, D. Mantovani, Acta Biomaterialia 6 (2010) 1852–1860.
[57] B. Zberg, P.J. Uggowitzer, J.F. Loffler, Nature Materials 8 (2009) 887–891.
[58] Y.B. Wang, X.H. Xie, H.F. Li, X.L. Wang, M.Z. Zhao, E.W. Zhang, Y.J. Bai, Y.F. Zheng, L. Qin, Acta Biomaterialia 7 (2011) 3196–3208.
[59] C. Janning, E. Willbold, C. Vogt, J. Nellesen, A. Meyer-Lindenberg, H. Windhagen, F. Thorey, F. Witte, Acta Biomaterialia 6 (2010) 1861–1868.
[60] H.G. Seiler, H. Sigel, Handbook of Toxicity of Inorganic Compounds, Marcel Dekker Inc., New York, 1988.
[61] F. Witte, J. Fischer, J. Nellesen, H.-A. Crostack, V. Kaese, A. Pisch, F. Beckmann, H. Windhagen, Biomaterials 27 (2006) 1013–1018.
[62] M.M. Avedesian, H. Baker, Magnesium and Magnesium Alloys (ASM Specialty Handbook), ASM International, Materials Park, Ohio, 1999.
[63] ASTM-G01-03-E: Standard Practice for Preparing, Cleaning, and Evaluating Corrosion Test Specimens, Annual Book of ASTM Standards, American Society for Testing and Materials, Philadelphia, PA, USA, 2003.
[64] F. Witte, J. Fischer, J. Nellesen, C. Vogt, J. Vogt, T. Donath, F. Beckmann, Acta Biomaterialia 6 (2010) 1792–1799.
[65] H. Sigel, Metal Ions in Biological System, Marcel Dekker Inc., New York, 1986.
[66] B.A. Bowman, R.M. Russell, Present Knowledge in Nutrition, 8th ed., International Life Science Institute, Washington DC, 2001.
[67] F. Feyerabend, J. Fischer, J. Holtz, F. Witte, R. Willumeit, H. Drücker, C. Vogt, N. Hort, Acta Biomaterialia 6 (2010) 1834–1842.
[68] N.J. Hallab, C. Vermes, C. Messina, K.A. Roebuck, T.T. Glant, J.J. Jacobs, Journal of Biomedical Materials Research 60 (2002) 420–433.
[69] A. Loos, R. Rohde, A. Haverich, S. Barlach, Macromolecular Symposia 253 (2007) 103–108.
[70] Z. Li, X. Gu, S. Lou, Y. Zheng, Biomaterials 29 (2008) 1329–1344.
[71] X.N. Gu, X.H. Xie, N. Li, Y.F. Zheng, L. Qin, Acta Biomaterialia 8 (2012) 2360–2374.
[72] X.N. Gu, Y.F. Zheng, Y. Cheng, S.P. Zhong, T.F. Xi, Biomaterials 30 (2009) 484–498.
[73] A. Drynda, T. Hassel, R. Hoehn, A. Perz, F.-W. Bach, M. Peuster, Journal of Biomedical Materials Research Part A 93A (2010) 763–775.
[74] P.P. Mueller, T. May, A. Perz, H. Hauser, M. Peuster, Biomaterials 27 (2006) 2193–2200.
[75] A. Purnama, H. Hermawan, S. Champetier, D. Mantovani, J. Couet, Acta Biomaterialia 9 (2013) 8746–8753.
[76] A. Purnama, D. Mantovani, J. Couet, Acta Biomaterialia 9 (2013) 8754–8760.
[77] M. Peuster, C. Hesse, T. Schloo, C. Fink, P. Beerbaum, C. von Schnakenburg, Biomaterials 27 (2006) 4955–4962.
[78] F. Witte, H. Ulrich, C. Palm, E. Willbold, Journal of Biomedical Materials Research Part A 81A (2007) 757–765.
[79] F. Witte, H. Ulrich, M. Rudert, E. Willbold, Journal of Biomedical Materials Research Part A 81A (2007) 748–756.
[80] Z. Qiao, Z. Shi, N. Hort, N.I. Zainal Abidin, A. Atrens, Corrosion Science 61 (2012) 185–207.
[81] G.L. Song, Corrosion Science 49 (2007) 1696–1701.
[82] H.E. Friedrich, B.L. Mordike, Magnesium Technology—Metallurgy, Design Date, Applications, Springer, Berlin/Heidelberg/New York, 2005.
[83] Y. Wan, G. Xiong, H. Luo, F. He, Y. Huang, X. Zhou, Materials & Design 29 (2008) 2034–2037.
[84] W.-C. Kim, J.-G. Kim, J.-Y. Lee, H.-K. Seok, Materials Letters 62 (2008) 4146–4148.

[85] N.T. Kirkland, N. Birbilis, J. Walker, T. Woodfield, G.J. Dias, M.P. Staiger, Journal of Biomedical Materials Research Part B: Applied Biomaterials 95B (2010) 91–100.
[86] H. Du, Z.J. Wei, X.W. Liu, E.L. Zhang, Materials Chemistry and Physics 125 (2011) 568–575.
[87] Y. Li, P. Hodgson, C.E. Wen, Journal of Materials Science 46 (2011) 365–371.
[88] I.S. Berglund, H.S. Brar, N. Dolgova, A.P. Acharya, B.G. Keselowsky, M. Sarntinoranont, M.V. Manuel, Journal of Biomedical Materials Research Part B: Applied Biomaterials 100B (2012) 1524–1534.
[89] H.S. Brar, J. Wong, M.V. Manuel, Journal of the Mechanical Behavior of Biomedical Materials 7 (2012) 87–95.
[90] X. Gu, Biodegradation and biocompatibility evaluation of magnesium based materials, (doctor thesis), Peking University, 2011.
[91] M. Bornapour, N. Muja, D. Shum-Tim, M. Cerruti, M. Pekguleryuz, Acta Biomaterialia 9 (2013) 5319–5330.
[92] B. Zhang, Y. Wang, L. Geng, Chapter 9 in Biomaterials – Physics and Chemistry, InTech, Rijeka, Croatia, 2011.
[93] B. Zhang, Y. Hou, X. Wang, Y. Wang, L. Geng, Materials Science and Engineering C 31 (2011) 1667–1673.
[94] E. Zhang, D. Yin, L. Xu, L. Yang, K. Yang, Materials Science and Engineering C 29 (2009) 987–993.
[95] E. Zhang, W. He, H. Du, K. Yang, Materials Science and Engineering A 488 (2008) 102–111.
[96] Z. Huan, M. Leeflang, J. Zhou, L. Fratila-Apachitei, J. Duszczyk, Journal of Materials Science: Materials in Medicine 21 (2010) 2623–2635.
[97] X.S. Hu, K. Wu, M.Y. Zheng, W.M. Gan, X.J. Wang, Materials Science and Engineering A 452–453 (2007) 374–379.
[98] E. Zhang, L. Yang, J. Xu, H. Chen, Acta Biomaterialia 6 (2010) 1756–1762.
[99] H. Liu, Y. Chen, Y. Tang, S. Wei, G. Niu, Journal of Alloys and Compounds 440 (2007) 122–126.
[100] G. Nayyeri, R. Mahmudi, Materials & Design 32 (2011) 1571–1576.
[101] X. Yang, Study on microstructure and properties of biomedical Mg–Sn–Mn alloy, (master thesis), Harbin Engineering University, 2011.
[102] M.-H. Tsai, M.-S. Chen, L.-H. Lin, M.-H. Lin, C.-Z. Wu, K.-L. Ou, C.-H. Yu, Journal of Alloys and Compounds 509 (2011) 813–819.
[103] Y.L. Zhou, J. An, D.M. Luo, W.Y. Hu, Y.C. Li, P. Hodgson, C.E. Wen, Materials Technology: Advanced Performance Materials 27 (2012) 52–54.
[104] W. Zhang, M. Li, Q. Chen, W. Hu, W. Zhang, W. Xin, Materials & Design 39 (2012) 379–383.
[105] Y. Li, C. Wen, D. Mushahary, R. Sravanthi, N. Harishankar, G. Pande, P. Hodgson, Acta Biomaterialia 8 (2012) 3177–3188.
[106] ASTM-B275-04: Standard Practice for Codification of Certain Nonferrous Metals and Alloys, Cast and Wrought, Annual Book of ASTM Standards, American Society for Testing and Materials, Philadelphia, PA, USA, 2004.
[107] Z. Wen, C. Wu, C. Dai, F. Yang, Journal of Alloys and Compounds 488 (2009) 392–399.
[108] F. Witte, V. Kaese, H. Haferkamp, E. Switzer, A. Meyer-Lindenberg, C.J. Wirth, H. Windhagen, Biomaterials 26 (2005) 3557–3563.
[109] N. Birbilis, M.A. Easton, A.D. Sudholz, S.M. Zhu, M.A. Gibson, Corrosion Science 51 (2009) 683–689.
[110] T. Razychoń, J. Michalska, A. Kielbus, Journal of Achievements in Materials and Manufacturing Engineering 20 (2007) 191–194.
[111] R. Walter, M. Kannan, Materials Letters 65 (2011) 748–750.
[112] X. Zhang, G. Yuan, Z. Wang, Materials Letters 74 (2012) 128–131.
[113] X. Zhang, G. Yuan, L. Mao, J. Niu, P. Fu, W. Ding, Journal of the Mechanical Behavior of Biomedical Materials 7 (2012) 77–86.
[114] N. Hort, Y. Huang, D. Fechner, M. Störmer, C. Blawert, F. Witte, C. Vogt, H. Drücker, R. Willumeit, K.U. Kainer, F. Feyerabend, Acta Biomaterialia 6 (2010) 1714–1725.
[115] M. Liu, P. Schmutz, P.J. Uggowitzer, G. Song, A. Atrens, Corrosion Science 52 (2010) 3687–3701.
[116] L. Yang, Y. Huang, Q. Peng, F. Feyerabend, K.U. Kainer, R. Willumeit, N. Hort, Materials Science and Engineering B 176 (2011) 1827–1834.
[117] E. Aghion, T. Yered, Y. Perez, Y. Gueta, Advanced Engineering Materials 12 (2010) B374–B379.
[118] C.E. Wen, M. Mabuchi, Y. Yamada, K. Shimojima, Y. Chino, T. Asahina, Scripta Materialia 45 (2001) 1147–1153.
[119] C.E. Wen, Y. Yamada, K. Shimojima, Y. Chino, H. Hosokawa, M. Mabuchi, Materials Science Forum 419–422 (2003) 1001–1006.
[120] H. Zhuang, Y. Han, A. Feng, Materials Science and Engineering C 28 (2008) 1462–1466.
[121] M.P. Staiger, I. Kolbeinsson, N.T. Kirkland, T. Nguyen, G. Dias, T.B.F. Woodfield, Materials Letters 64 (2010) 2572–2574.
[122] F. Geng, L. Tan, B. Zhang, C. Wu, Y. He, J. Yang, K. Yang, Journal of Materials Science & Technology 25 (2009) 123–129.
[123] X.N. Gu, W.R. Zhou, Y.F. Zheng, Y. Liu, Y.X. Li, Materials Letters 64 (2010) 1871–1874.
[124] A.L. Feng, Y. Han, Journal of Alloys and Compounds 504 (2010) 585–593.
[125] A.L. Feng, Y. Han, Materials & Design 32 (2011) 2813–2820.
[126] M. Razavi, M.H. Fathi, M. Meratian, Materials Science and Engineering A 527 (2010) 6938–6944.
[127] X.N. Gu, W.R. Zhou, Y.F. Zheng, L.M. Dong, Y.L. Xi, D.L. Chai, Materials Science & Engineering C: Materials for Biological Applications 30 (2010) 827–832.
[128] X.N. Gu, X. Wang, N. Li, L. Li, Y.F. Zheng, X. Miao, Journal of Biomedical Materials Research Part B: Applied Biomaterials 99B (2011) 127–134.
[129] F. Witte, F. Feyerabend, P. Maier, J. Fischer, M. Stormer, C. Blawert, W. Dietzel, N. Hort, Biomaterials 28 (2007) 2163–2174.
[130] X. Ye, M. Chen, M. Yang, J. Wei, D. Liu, Journal of Materials Science: Materials in Medicine 21 (2010) 1321–1328.
[131] D. Liu, Y. Zuo, W. Meng, M. Chen, Materials Science and Engineering C 32 (2012) 1253–1258.
[132] Z.G. Huan, M.A. Leeflang, J. Zhou, J. Duszczyk, Materials Science and Engineering B 176 (2011) 1644–1652.
[133] T. Lei, W. Tang, S. Cai, F. Feng, N. Li, Corrosion Science 54 (2012) 270–277.
[134] Y.F. Zheng, X.N. Gu, Y.L. Xi, D.L. Chai, Acta Biomaterialia 6 (2010) 1783–1791.
[135] Z. Huan, J. Zhou, J. Duszczyk, Journal of Materials Science: Materials in Medicine 21 (2010) 3163–3169.
[136] X.N. Gu, X.L. Li, W.R. Zhou, Y. Cheng, Y.F. Zheng, Biomedical Materials 5 (2010) 035013.
[137] Z. Xu, C. Smith, S. Chen, J. Sankar, Materials Science and Engineering B 176 (2011) 1660–1665.
[138] J.H. Gao, S.K. Guan, Z.W. Ren, Y.F. Sun, S.J. Zhu, B. Wang, Materials Letters 65 (2011) 691–693.
[139] F. Kang, J.Q. Liu, J.T. Wang, X. Zhao, Advanced Engineering Materials 12 (2010) 730–734.
[140] X.N. Gu, N. Li, Y.F. Zheng, F. Kang, J.T. Wang, L. Ruan, Materials Science and Engineering B 176 (2011) 1802–1806.
[141] H. Wang, Y. Estrin, H. Fu, G. Song, Z. Zúberová, Advanced Engineering Materials 9 (2007) 967–972.
[142] X. Guo, R. Remennik, C. Xu, D. Shechtman, Materials Science and Engineering A 473 (2008) 266–273.
[143] X. Guo, D. Shechtman, Journal of Materials Processing Technology 187–188 (2007) 640–644.
[144] E. Willbold, K. Kalla, I. Bartsch, K. Bobe, M. Brauneis, S. Remennik, D. Shechtman, J. Nellesen, W. Tillmann, C. Vogt, F. Witte, Acta Biomaterialia 9 (2013) 8509–8517.
[145] X.N. Gu, Y.F. Zheng, S.P. Zhong, T.F. Xi, J.Q. Wang, W.H. Wang, Biomaterials 31 (2010) 1093–1103.
[146] V. Wessels, G. Le Mené, S.F. Fischerauer, T. Kraus, A.-M. Weinberg, P.J. Uggowitzer, J.F. Löffler, Advanced Engineering Materials 14 (2012) B357–B364.
[147] M.K. Datta, D.-T. Chou, D. Hong, P. Saha, S.J. Chung, B. Lee, A. Sirinterlikci, M. Ramanathan, A. Roy, P.N. Kumta, Materials Science and Engineering B 176 (2011) 1637–1643.
[148] B. Zberg, E.R. Arata, P.J. Uggowitzer, J.F. Löffler, Acta Materialia 57 (2009) 3223–3231.
[149] S. González, E. Pellicer, J. Fornell, A. Blanquer, L. Barrios, E. Ibáñez, P. Solsona, S. Suriñach, M.D. Baró, C. Nogués, J. Sort, Journal of the Mechanical Behavior of Biomedical Materials 6 (2012) 53–62.
[150] H.-J. Yu, J.-Q. Wang, X.-T. Shi, D.V. Louzguine-Luzgin, H.-K. Wu, J.H. Perepezko, Advanced Functional Materials 23 (2013) 4793–4800.
[151] M. Salahshoor, Y.B. Guo, International Journal of Machine Tools and Manufacture 51 (2011) 579–590.
[152] M. Salahshoor, Y. Guo, Production Engineering 5 (2011) 641–650.
[153] Y.B. Guo, M. Salahshoor, CIRP Annals: Manufacturing Technology 59 (2010) 151–154.
[154] M. Salahshoor, Y. Guo, International Journal of Advanced Manufacturing Technology 67 (2013) 601–611.
[155] M.P. Sealy, Y.B. Guo, Journal of the Mechanical Behavior of Biomedical Materials 3 (2010) 488–496.
[156] Z. Pu, J.C. Outeiro, A.C. Batista, O.W. Dillon Jr., D.A. Puleo, I.S. Jawahir, International Journal of Machine Tools and Manufacture 56 (2012) 17–27.
[157] Z. Pu, G.L. Song, S. Yang, J.C. Outeiro, O.W. Dillon Jr., D.A. Puleo, I.S. Jawahir, Corrosion Science 57 (2012) 192–201.
[158] Z. Pu, J.C. Outeiro, A.C. Batista, O.W. Dillon, D.A. Puleo, I.S. Jawahir, Procedia Engineering 19 (2011) 282–287.
[159] K.Y. Chiu, M.H. Wong, F.T. Cheng, H.C. Man, Surface and Coatings Technology 202 (2007) 590–598.
[160] T. Yan, L. Tan, D. Xiong, X. Liu, B. Zhang, K. Yang, Materials Science and Engineering C 30 (2010) 740–748.
[161] L. Li, J. Gao, Y. Wang, Surface and Coatings Technology 185 (2004) 92–98.
[162] X.N. Gu, W. Zheng, Y. Cheng, Y.F. Zheng, Acta Biomaterialia 5 (2009) 2790–2799.
[163] Y. Zhu, G. Wu, Y.-H. Zhang, Q. Zhao, Applied Surface Science 257 (2011) 6129–6137.
[164] Y. Zhu, Q. Zhao, Y.-H. Zhang, G. Wu, Surface & Coatings Technology 206 (2012) 2961–2966.
[165] X.N. Gu, N. Li, W.R. Zhou, Y.F. Zheng, X. Zhao, Q.Z. Cai, L. Ruan, Acta Biomaterialia 7 (2011) 1880–1889.
[166] S. Hiromoto, T. Shishido, A. Yamamoto, N. Maruyama, H. Somekawa, T. Mukai, Corrosion Science 50 (2008) 2906–2913.
[167] Y.M. Wang, F.H. Wang, M.J. Xu, B. Zhao, L.X. Guo, J.H. Ouyang, Applied Surface Science 255 (2009) 9124–9131.
[168] Z. Yao, L. Li, Z. Jiang, Applied Surface Science 255 (2009) 6724–6728.
[169] Y. Song, S. Zhang, J. Li, C. Zhao, X. Zhang, Acta Biomaterialia 6 (2010) 1736–1742.
[170] H. Wang, S. Guan, Y. Wang, H. Liu, H. Wang, L. Wang, C. Ren, S. Zhu, K. Chen, Colloids and Surfaces B: Biointerfaces 88 (2011) 254–259.
[171] H.X. Wang, S.K. Guan, X. Wang, C.X. Ren, L.G. Wang, Acta Biomaterialia 6 (2010) 1743–1748.
[172] C. Wen, S. Guan, L. Peng, C. Ren, X. Wang, Z. Hu, Applied Surface Science 255 (2009) 6433–6438.
[173] X.B. Chen, N. Birbilis, T.B. Abbott, Corrosion Science 53 (2011) 2263–2268.
[174] S. Keim, J.G. Brunner, B. Fabry, S. Virtanen, Journal of Biomedical Materials Research Part B: Applied Biomaterials 96B (2011) 84–90.
[175] Z. Wei, H. Du, E. Zhang, Surface and Interface Analysis 43 (2011) 791–794.

[176] J.X. Yang, F.Z. Cui, Q.S. Yin, Y. Zhang, T. Zhang, X.M. Wang, IEEE Transactions on Plasma Science 37 (2009) 1161–1168.
[177] L. Xu, F. Pan, G. Yu, L. Yang, E. Zhang, K. Yang, Biomaterials 30 (2009) 1512–1523.
[178] J. Hu, C. Zhang, B. Cui, K. Bai, S. Guan, L. Wang, S. Zhu, Applied Surface Science 257 (2011) 8772–8777.
[179] A. Roy, S.S. Singh, M.K. Datta, B. Lee, J. Ohodnicki, P.N. Kumta, Materials Science and Engineering B 176 (2011) 1679–1689.
[180] A. Zomorodian, F. Brusciotti, A. Fernandes, M.J. Carmezim, T. Moura e Silva, J.C.S. Fernandes, M.F. Montemor, Surface and Coatings Technology 206 (2012) 4368–4375.
[181] A. Doepke, D. Xue, Y. Yun, W.J. Vanooij, H. Brian Halsall, W.R. Heineman, Electrochimica Acta 70 (2012) 165–170.
[182] J. Li, P. Cao, X. Zhang, S. Zhang, Y. He, Journal of Materials Science 45 (2010) 6038–6045.
[183] P. Lu, L. Cao, Y. Liu, X. Xu, X. Wu, Journal of Biomedical Materials Research Part B: Applied Biomaterials 96B (2011) 101–109.
[184] P. Lu, H. Fan, Y. Liu, L. Cao, X. Wu, X. Xu, Colloids and Surfaces B: Biointerfaces 83 (2011) 23–28.
[185] X. Xu, P. Lu, M. Guo, M. Fang, Applied Surface Science 256 (2010) 2367–2371.
[186] L. Xu, A. Yamamoto, Applied Surface Science 258 (2012) 6353–6358.
[187] Y.Z. Wan, G.Y. Xiong, H.L. Luo, F. He, Y. Huang, Y.L. Wang, Applied Surface Science 254 (2008) 5514–5516.
[188] C. Liu, Y. Xin, X. Tian, J. Zhao, P.K. Chu, Journal of Vacuum Science & Technology A: Vacuum, Surfaces, and Films 25 (2007) 334–339.
[189] Y. Zhao, G. Wu, H. Pan, K.W.K. Yeung, P.K. Chu, Materials Chemistry and Physics 132 (2012) 187–191.
[190] G. Wu, K. Feng, A. Shanaghi, Y. Zhao, R. Xu, G. Yuan, P.K. Chu, Surface and Coatings Technology 206 (2012) 3186–3195.
[191] J.X. Yang, F.Z. Cui, I.-S. Lee, Y.P. Jiao, Q.S. Yin, Y. Zhang, Surface and Coatings Technology 202 (2008) 5737–5741.
[192] J.X. Yang, Y.P. Jiao, F.Z. Cui, I.-S. Lee, Q.S. Yin, Y. Zhang, Surface and Coatings Technology 202 (2008) 5733–5736.
[193] P. Salunke, V. Shanov, F. Witte, Materials Science and Engineering B 176 (2011) 1711–1717.
[194] Y.S. Zou, Y.F. Wu, H. Yang, K. Cang, G.H. Song, Z.X. Li, K. Zhou, Applied Surface Science 258 (2011) 1624–1629.
[195] M. Li, Y. Cheng, Y.F. Zheng, X. Zhang, T.F. Xi, S.C. Wei, Applied Surface Science 258 (2012) 3074–3081.
[196] M.D. Pereda, C. Alonso, L. Burgos-Asperilla, J.A. del Valle, O.A. Ruano, P. Perez, M.A. Fernández Lorenzo de Mele, Acta Biomaterialia 6 (2010) 1772–1782.
[197] J.-M. Seitz, K. Collier, E. Wulf, D. Bormann, F.-W. Bach, Advanced Engineering Materials 13 (2011) 313–323.
[198] Y. Al-Abdullat, S. Tsutsumi, N. Nakajima, M. Ohta, H. Kuwahara, K. Ikeuchi, Materials Transactions 42 (2001) 1777–1780.
[199] S. Hiromoto, A. Yamamoto, Materials Science and Engineering C 30 (2010) 1085–1093.
[200] X. Zhang, Z. Zhao, F. Wu, Y. Wang, J. Wu, Journal of Materials Science 42 (2007) 8523–8528.
[201] D.-W. Wang, Y. Cao, H. Qiu, Z.-G. Bi, Journal of Biomedical Materials Research Part A 99A (2011) 166–172.
[202] P.B. Srinivasan, J. Liang, C. Blawert, M. Störmer, W. Dietzel, Applied Surface Science 256 (2010) 4017–4022.
[203] P.B. Srinivasan, J. Liang, C. Blawert, M. Störmer, W. Dietzel, Journal of Materials Science 45 (2010) 1406–1410.
[204] J. Gao, X. Shi, B. Yang, S. Hou, E. Meng, F. Guan, S. Guan, Journal of Materials Science: Materials in Medicine 22 (2011) 1681–1687.
[205] J.H. Gao, S.K. Guan, J. Chen, L.G. Wang, S.J. Zhu, J.H. Hu, Z.W. Ren, Applied Surface Science 257 (2011) 2231–2237.
[206] Y. Shi, M. Qi, Y. Chen, P. Shi, Materials Letters 65 (2011) 2201–2204.
[207] D. Sreekanth, N. Rameshbabu, Materials Letters 68 (2012) 439–442.
[208] M. Guo, L. Cao, P. Lu, Y. Liu, X. Xu, Journal of Materials Science: Materials in Medicine 22 (2011) 1735–1740.
[209] P. Liu, X. Pan, W. Yang, K. Cai, Y. Chen, Materials Letters 75 (2012) 118–121.
[210] H. Wang, C. Zhao, Y. Chen, J. Li, X. Zhang, Materials Letters 68 (2012) 435–438.
[211] Y.W. Song, D.Y. Shan, E.H. Han, Materials Letters 62 (2008) 3276–3279.
[212] E. Meng, S. Guan, H. Wang, L. Wang, S. Zhu, J. Hu, C. Ren, J. Gao, Y. Feng, Applied Surface Science 257 (2011) 4811–4816.
[213] B. Wang, J. Gao, L. Wang, S. Zhu, S. Guan, Materials Letters 70 (2012) 174–176.
[214] Y. Zhang, G. Zhang, M. Wei, Journal of Biomedical Materials Research Part B: Applied Biomaterials 89B (2009) 408–414.
[215] J.E. Gray-Munro, M. Strong, Journal of Biomedical Materials Research Part A 90A (2009) 339–350.
[216] H. Du, Z. Wei, H. Wang, E. Zhang, L. Zuo, L. Du, Colloids and Surfaces B: Biointerfaces 83 (2011) 96–102.
[217] L. Xu, E. Zhang, K. Yang, Journal of Materials Science: Materials in Medicine 20 (2009) 859–867.
[218] S.S. Singh, A. Roy, B. Lee, P.N. Kumta, Materials Science and Engineering B 176 (2011) 1695–1702.
[219] H.M. Wong, K.W.K. Yeung, K.O. Lam, V. Tam, P.K. Chu, K.D.K. Luk, K.M.C. Cheung, Biomaterials 31 (2010) 2084–2096.
[220] L. Xu, A. Yamamoto, Colloids and Surfaces B: Biointerfaces 93 (2012) 67–74.
[221] J.N. Li, P. Cao, X.N. Zhang, S.X. Zhang, Y.H. He, Journal of Materials Science 45 (2010) 6038–6045.
[222] X.N. Gu, Y.F. Zheng, Q.X. Lan, Y. Cheng, Z.X. Zhang, T.F. Xi, D.Y. Zhang, Biomedical Materials 4 (2009) 044109.
[223] T.F. da Conceicao, N. Scharnagl, W. Dietzel, K.U. Kainer, Corrosion Science 53 (2011) 338–346.
[224] K.Y. Cai, X.J. Sui, Y. Hu, L. Zhao, M. Lai, Z. Luo, P. Liu, W.H. Yang, Materials Science and Engineering C 31 (2011) 1800–1808.
[225] X. Luo, X.T. Cui, Acta Biomaterialia 7 (2011) 441–446.
[226] W.F. Ng, M.H. Wong, F.T. Cheng, Surface and Coatings Technology 204 (2010) 1823–1830.
[227] R. Xu, G. Wu, X. Yang, T. Hu, Q. Lu, P.K. Chu, Materials Letters 65 (2011) 2171–2173.
[228] C. Liu, Y. Xin, X. Tian, P.K. Chu, Thin Solid Films 516 (2007) 422–427.
[229] E. Zhang, L. Xu, K. Yang, Scripta Materialia 53 (2005) 523–527.
[230] T. Zhu, F. Fang, J. Kennedy, W. Gao, Advanced Materials Development and Performance (AMDP2011) 6 (2012) 700–704.
[231] G. Wu, R. Xu, K. Feng, S. Wu, Z. Wu, G. Sun, G. Zheng, G. Li, P.K. Chu, Applied Surface Science 258 (2012) 7651–7657.
[232] T.T. Yan, L.L. Tan, D.S. Xiong, X.J. Liu, B.C. Zhang, K. Yang, Materials Science & Engineering C: Materials for Biological Applications 30 (2010) 740–748.
[233] M. Sekiguchi, C. Otani, M. Takaya, Journal of Japan Institute of Light Metals 56 (2006) 156–161.
[234] Y. Han, T. Fu, J. Lu, K. Xu, Journal of Biomedical Materials Research 54 (2001) 96–101.
[235] O. Duygulu, R.A. Kaya, G. Oktay, A.A. Kaya, Materials Science Forum 546–549 (2007) 421–424.
[236] M. Thomann, C. Krause, D. Bormann, N. von der Hoh, H. Windhagen, A. Meyer-Lindenberg, Materialwissenschaft Und Werkstofftechnik 40 (2009) 82–87.
[237] M. Thomann, C. Krause, N. Angrisani, D. Bormann, T. Hassel, H. Windhagen, A. Meyer-Lindenberg, Journal of Biomedical Materials Research Part A 93A (2010) 1609–1619.
[238] N. von der Höh, B. von Rechenberg, D. Bormann, A. Lucas, A. Meyer-Lindenberg, Materialwissenschaft Und Werkstofftechnik 40 (2009) 88–93.
[239] N. Von Der Höh, D. Bormann, A. Lucas, B. Denkena, C. Hackenbroich, A. Meyer-Lindenberg, Advanced Engineering Materials 11 (2009) B47–B54.
[240] N. Erdmann, N. Angrisani, J. Reifenrath, A. Lucas, F. Thorey, D. Bormann, A. Meyer-Lindenberg, Acta Biomaterialia 7 (2011) 1421–1428.
[241] L.P. Xu, G.N. Yu, E. Zhang, F. Pan, K. Yang, Journal of Biomedical Materials Research Part A 83A (2007) 703–711.
[242] E. Zhang, L. Xu, G. Yu, F. Pan, K. Yang, Journal of Biomedical Materials Research Part A 90A (2009) 882–893.
[243] S. Chen, S.K. Guan, W. Li, H.X. Wang, J. Chen, Y.S. Wang, H.T. Wang, Journal of Biomedical Materials Research Part B: Applied Biomaterials 100B (2012) 533–543.
[244] C. Castellani, R.A. Lindtner, P. Hausbrandt, E. Tschegg, S.E. Stanzl-Tschegg, G. Zanoni, S. Beck, A.M. Weinberg, Acta Biomaterialia 7 (2011) 432–440.
[245] A. Celarek, T. Kraus, E.K. Tschegg, S.F. Fischeraurer, S. Stanzl-Tschegg, P.J. Uggowitzer, A.M. Weinberg, Materials Science and Engineering C 32 (2012) 1503–1510.
[246] S. Remennik, I. Bartsch, E. Willbold, F. Witte, D. Shechtman, Materials Science and Engineering B 176 (2011) 1653–1659.
[247] B. Heublein, R. Rohde, V. Kaese, M. Niemeyer, W. Hartung, A. Haverich, Heart 89 (2003) 651–656.
[248] C. Di Mario, H.U.W. Griffiths, O. Goktekin, N. Peeters, J.A.N. Verbist, M. Bosiers, K. Deloose, B. Heublein, R. Rohde, V. Kasese, C. Ilsley, R. Erbel, Journal of Interventional Cardiology 17 (2004) 391–395.
[249] R. Waksman, R. Pakala, P.K. Kuchulakanti, R. Baffour, D. Hellinga, R. Seabron, F.O. Tio, E. Wittchow, S. Hartwig, C. Harder, R. Rohde, B. Heublein, A. Andreae, K.-H. Waldmann, A. Haverich, Catheterization and Cardiovascular Interventions 68 (2006) 607–617.
[250] T.L.P. Slottow, R. Pakala, T. Okabe, D. Hellinga, R.J. Lovec, F.O. Tio, A.B. Bui, R. Waksman, Cardiovascular Revascularization Medicine 9 (2008) 248–254.
[251] M. Maeng, L.O. Jensen, E. Falk, H.R. Andersen, L. Thuesen, Heart 95 (2009) 241–246.
[252] P. Zartner, R. Cesnjevar, H. Singer, M. Weyand, Catheterization and Cardiovascular Interventions 66 (2005) 590–594.
[253] D. Schranz, P. Zartner, I. Michel-Behnke, H. Akintürk, Catheterization and Cardiovascular Interventions 67 (2006) 671–673.
[254] P. Zartner, M. Buettner, H. Singer, M. Sigler, Catheterization and Cardiovascular Interventions 69 (2007) 443–446.
[255] C.J. McMahon, P. Oslizlok, K.P. Walsh, Catheterization and Cardiovascular Interventions 69 (2007) 735–738.
[256] P. Peeters, M. Bosiers, J. Verbist, K. Deloose, B. Heublein, Journal of Endovascular Therapy 12 (2005) 1–5.
[257] M. Bosiers, K. Deloose, J. Verbist, P. Peeters, Journal of Cardiovascular Surgery 47 (2006) 171–176.
[258] P. Barlis, J. Tanigawa, C. Di Mario, European Heart Journal 28 (2007) 2319.
[259] R. Waksman, R. Erbel, C. Di Mario, J. Bartunek, B. de Bruyne, F.R. Eberli, P. Erne, M. Haude, M. Horrigan, C. Ilsley, D. Böse, H. Bonnier, J. Koolen, T.F. Lüscher, N.J. Weissman, JACC: Cardiovascular Interventions 2 (2009) 312–320.
[260] R. Erbel, C. Di Mario, J. Bartunek, J. Bonnier, B. de Bruyne, F.R. Eberli, P. Erne, M. Haude, B. Heublein, M. Horrigan, C. Ilsley, D. Böse, J. Koolen, T.F. Lüscher, N. Weissman, R. Waksman, Lancet 369 (2007) 1869–1875.
[261] M. Haude, R. Erbel, P. Erne, S. Verheye, H. Degen, D. Böse, P. Vermeersch, I. Wijnbergen, N. Weissman, F. Prati, R. Waksman, J. Koolen, Lancet 381 (2013) 836–844.
[262] R.O.N. Waksman, R. Pakala, T. Okabe, D. Hellinga, R. Chan, M.O. Tio, E. Wittchow, S. Hartwig, K.-H. Waldmann, C. Harder, Journal of Interventional Cardiology 20 (2007) 367–372.
[263] R. Waksman, R. Pakala, Current Pharmaceutical Design 16 (2010) 4041–4051.
[264] G.B. Lim, Nature Reviews Cardiology 10 (2013) 120.

[265] M. Moravej, F. Prima, M. Fiset, D. Mantovani, Acta Biomaterialia 6 (2010) 1726–1735.
[266] F.L. Nie, Y.F. Zheng, S.C. Wei, C. Hu, G. Yang, Biomedical Materials 5 (2010) 065015.
[267] B. Wegener, B. Sievers, S. Utzschneider, P. Müller, V. Jansson, S. Rößler, B. Nies, G. Stephani, B. Kieback, P. Quadbeck, Materials Science and Engineering B 176 (2011) 1789–1796.
[268] J. Cheng, Y.F. Zheng, Journal of Biomedical Materials Research Part B: Applied Biomaterials 101B (2013) 485–497.
[269] Q. Feng, D. Zhang, C. Xin, X. Liu, W. Lin, W. Zhang, S. Chen, K. Sun, Journal of Materials Science: Materials in Medicine 24 (2013) 713–724.
[270] M. Schinhammer, A.C. Hänzi, J.F. Löffler, P.J. Uggowitzer, Acta Biomaterialia 6 (2010) 1705–1713.
[271] B. Liu, Y.F. Zheng, L. Ruan, Materials Letters 65 (2011) 540–543.
[272] W. Xu, X. Lu, L. Tan, K. Yang, Acta Metallurgica Sinica 47 (2011) 1342–1347.
[273] M. Moravej, D. Mantovani, International Journal of Molecular Sciences 12 (2011) 4250–4270.
[274] H. Hermawan, D. Dubé, D. Mantovani, Journal of Biomedical Materials Research Part A 93A (2010) 1–11.
[275] H. Hermawan, D. Dubé, D. Mantovani, Advanced Materials Research 15 (2007) 107–112.
[276] H. Hermawan, H. Alamdari, D. Mantovani, D. Dubé, Powder Metallurgy 51 (2008) 38–45.
[277] M. Schinhammer, P. Steiger, F. Moszner, J.F. Löffler, P.J. Uggowitzer, Materials Science and Engineering C 33 (2013) 1882–1893.
[278] M. Schinhammer, I. Gerber, A.C. Hänzi, P.J. Uggowitzer, Materials Science and Engineering C 33 (2013) 782–789.
[279] M. Moravej, S. Amira, F. Prima, A. Rahem, M. Fiset, D. Mantovani, Materials Science and Engineering B 176 (2011) 1812–1822.
[280] M. Moravej, A. Purnama, M. Fiset, J. Couet, D. Mantovani, Acta Biomaterialia 6 (2010) 1843–1851.
[281] D.-T. Chou, D. Wells, D. Hong, B. Lee, H. Kuhn, P.N. Kumta, Acta Biomaterialia 9 (2013) 8593–8603.
[282] S. Zhu, N. Huang, L. Xu, Y. Zhang, H. Liu, Y. Lei, H. Sun, Y. Yao, Surface and Coatings Technology 203 (2009) 1523–1529.
[283] S. Zhu, N. Huang, H. Shu, Y. Wu, L. Xu, Applied Surface Science 256 (2009) 99–104.
[284] C.-Z. Chen, X.-H. Shi, P.-C. Zhang, B. Bai, Y.-X. Leng, N. Huang, Solid State Ionics 179 (2008) 971–974.
[285] M. Peuster, P. Wohlsein, M. Brugmann, M. Ehlerding, K. Seidler, C. Fink, H. Brauer, A. Fischer, G. Hausdorf, Heart 86 (2001) 563–569.
[286] R.O.N. Waksman, R. Pakala, R. Baffour, R. Seabron, D. Hellinga, F.O. Tio, Journal of Interventional Cardiology 21 (2008) 15–20.
[287] D. Pierson, J. Edick, A. Tauscher, E. Pokorney, P. Bowen, J. Gelbaugh, J. Stinson, H. Getty, C.H. Lee, J. Drelich, J. Goldman, Journal of Biomedical Materials Research Part B: Applied Biomaterials 100B (2012) 58–67.
[288] P.P. Mueller, S. Arnold, M. Badar, D. Bormann, F.-W. Bach, A. Drynda, A. Meyer-Lindenberg, H. Hauser, M. Peuster, Journal of Biomedical Materials Research Part A 100A (2012) 2881–2890.
[289] C. Wu, X. Hu, H. Qiu, Y. Ruan, Y. Tang, A. Wu, Y. Tian, P. Peng, Y. Chu, X. Xu, Q. Wang, L. Xu, B. Xu, D. Zhang, R.-L. Gao, Journal of the American College of Cardiology 60 (2012).
[290] D. Vojtěch, J. Kubásek, J. Šerák, P. Novák, Acta Biomaterialia 7 (2011) 3515–3522.
[291] X. Wang, H.M. Lu, X.L. Li, L. Li, Y.F. Zheng, Transactions of Nonferrous Metals Society of China 17 (2007) s122–s125.
[292] T. Butler, R. Jackson, J. Robson, R. Owen, H. Delves, C. Sieniawska, J. Rose, British Journal of Radiology 73 (2000) 601.
[293] M. Peuster, C. Fink, P. Wohlsein, M. Bruegmann, A. Günther, V. Kaese, M. Niemeyer, H. Haferkamp, C. Schnakenburg, Biomaterials 24 (2003) 393–399.
[294] M. Peuster, Biomaterials 24 (2003) 4057–4061.
[295] W. Jiao, H.F. Li, K. Zhao, H.Y. Bai, Y.B. Wang, Y.F. Zheng, W.H. Wang, Journal of Non-Crystalline Solids 357 (2011) 3830–3840.
[296] J.F. Li, D.Q. Zhao, M.L. Zhang, W.H. Wang, Applied Physics Letters 93 (2008) 171907.
[297] K. Zhao, J.F. Li, D.Q. Zhao, M.X. Pan, W.H. Wang, Scripta Materialia 61 (2009) 1091–1094.
[298] H.F. Li, K. Zhao, Y.B. Wang, Y.F. Zheng, W.H. Wang, Journal of Biomedical Materials Research Part B: Applied Biomaterials 100B (2012) 368–377.
[299] W. Jiao, K. Zhao, X.K. Xi, D.Q. Zhao, M.X. Pan, W.H. Wang, Journal of Non-Crystalline Solids 356 (2010) 1867–1870.
[300] H.F. Li, Y.B. Wang, Y. Cheng, Y.F. Zheng, Materials Letters 64 (2010) 1462–1464.
[301] O.I. Velikokhatnyi, P.N. Kumta, Acta Biomaterialia 6 (2010) 1698–1704.
[302] M. Muzyk, Z. Pakiela, K.J. Kurzydlowski, Scripta Materialia 66 (2012) 219–222.
[303] X. Zhang, G. Yuan, J. Niu, P. Fu, W. Ding, Journal of the Mechanical Behavior of Biomedical Materials 9 (2012) 153–162.
[304] Y. Zong, G. Yuan, X. Zhang, L. Mao, J. Niu, W. Ding, Materials Science and Engineering B 177 (2012) 395–401.
[305] X. Zhang, G. Yuan, L. Mao, J. Niu, W. Ding, Materials Letters 66 (2012) 209–211.
[306] H.-F. Sun, C.-J. Li, W.-B. Fang, Transactions of Nonferrous Metals Society of China 21 (Suppl. 2) (2011) s258–s261.
[307] L.X. He, Research on optimization of extrusion and drawing process of pure magnesium wire and influences on biological corrosion, (master thesis), Harbin Institute of Technology, 2010.
[308] B. Xu, Research on drawing process of AZ31 magnesium alloy wire, (master thesis), Harbin Institute of Technology, 2006.
[309] J.-M. Seitz, E. Wulf, P. Freytag, D. Bormann, F.-W. Bach, Advanced Engineering Materials 12 (2010) 1099–1105.
[310] http://www.originmedtech.com/news_view.asp?id=45.
[311] Y. Xue, Y. Ni, Z. Zhang, L. Lang, Y. Duan, China Metal Forming Equipment & Manufacturing Technology 43 (2008) 81–84.
[312] S. Lin, The research on WE43 magnesium alloys microtubules forming and medical modification, (master thesis), Lanzhou University of Technology, 2009.
[313] http://www.vascotube.com/.
[314] J.A. Grogan, S.B. Leen, P.E. McHugh, Journal of the Mechanical Behavior of Biomedical Materials 12 (2012) 129–138.
[315] S. Pant, N.W. Bressloff, C. Limbert, Biomechanics and Modeling in Mechanobiology 11 (2012) 61–82.
[316] W. Wu, L. Petrini, D. Gastaldi, T. Villa, M. Vedani, E. Lesma, M. Previtali, F. Migliavacca, Annals of Biomedical Engineering 38 (2010) 2829–2840.
[317] D. Gastaldi, V. Sassi, L. Petrini, M. Vedani, S. Trasatti, F. Migliavacca, Journal of the Mechanical Behavior of Biomedical Materials 4 (2011) 352–365.
[318] W. Wu, D. Gastaldi, K. Yang, L. Tan, L. Petrini, F. Migliavacca, Materials Science and Engineering B 176 (2011) 1733–1740.
[319] J.A. Grogan, B.J. O'Brien, S.B. Leen, P.E. McHugh, Acta Biomaterialia 7 (2011) 3523–3533.
[320] Y. Onuma, T. Muramatsu, A. Kharlamov, P.W. Serruys, Cardiovascular Intervention and Therapeutics 27 (2012) 141–154.
[321] Y. Yun, Z. Dong, N. Lee, Y. Liu, D. Xue, X. Guo, J. Kuhlmann, A. Doepke, H.B. Halsall, W. Heineman, S. Sundaramurthy, M.J. Schulz, Z. Yin, V. Shanov, D. Hurd, P. Nagy, W. Li, C. Fox, Materials Today 12 (2009) 22–32.
[322] M.R. Smith, P. Atkinson, D. White, T. Piersma, G. Gutierrez, G. Rossini, S. Desai, S. Wellinghoff, H. Yu, X. Cheng, Journal of Biomedical Materials Research Part B: Applied Biomaterials 100B (2012) 206–216.
[323] C.B. Chng, D.P. Lau, J.Q. Choo, C.K. Chui, Acta Biomaterialia 8 (2012) 2835–2844.
[324] D.P. Lau, C.B. Chng, J.Q. Choo, N. Teo, R.M. Bunte, C.K. Chui, Laryngoscope 122 (2012) 1809–1814.
[325] F. Klocke, M. Schwade, A. Klink, A. Kopp, Procedia Engineering 19 (2011) 190–195.
[326] I. Shigematsu, N. Saito, M. Nakanishi, M. Mabuchi, H. Matsuyama, M. Nakamura, Journal of Japan Institute of Light Metals 50 (2000) 446–450.
[327] S.O. Kim, J.S. Kwak, Transactions of Nonferrous Metals Society of China 18 (Suppl. 1) (2008) s369–s373.
[328] X.L. Liu, W.R. Zhou, Y.H. Wu, Y. Cheng, Y.F. Zheng, Materials Science and Engineering C 33 (2013) 4144–4154.
[329] J. Forrester, M. Fishbein, R. Helfant, J. Fagin, Journal of the American College of Cardiology 17 (1991) 758–769.
[330] P. Serruys, H. Luijten, K. Beatt, R. Geuskens, P. de Feyter, M. van den Brand, J. Reiber, H. ten Katen, G. van Es, P. Hugenholtz, Circulation 77 (1988) 361–371.
[331] T.P. Rüedi, W.M. Murphy, AO Principles of Fracture Management, 1st ed., Thieme, New York, 2000.
[332] A.L. Johnson, J.E.F. Houlton, R. Vannini, AO Principles of Fracture Management in the Dog and Cat, Thieme, New York, 2005.
[333] J.-W. Park, H.-J. Ko, J.-H. Jang, H. Kang, J.-Y. Suh, Journal of Biomedical Materials Research Part A 100A (2012) 834–840.
[334] W. Yang, Y. Zhang, J. Yang, L. Tan, K. Yang, Journal of Biomedical Materials Research Part A 99A (2011) 386–394.
[335] I. Slutsky, N. Abumaria, L.-J. Wu, C. Huang, L. Zhang, B. Li, X. Zhao, A. Govindarajan, M.-G. Zhao, M. Zhuo, S. Tonegawa, G. Liu, Neuron 65 (2010) 165–177.
[336] D.A. Robinson, R.W. Griffith, D. Shechtman, R.B. Evans, M.G. Conzemius, Acta Biomaterialia 6 (2010) 1869–1877.
[337] D.-R. Di, Z.-Z. He, Z.-Q. Sun, J. Liu, Nanomedicine: Nanotechnology, Biology, and Medicine 8 (2012) 1233–1241.
[338] I. Ohsawa, M. Ishikawa, K. Takahashi, M. Watanabe, K. Nishimaki, K. Yamagata, K.-I. Katsura, Y. Katayama, S. Asoh, S. Ohta, Nature Medicine 13 (2007) 688–694.
[339] K. Ohno, M. Ito, M. Ichihara, M. Ito, Oxidative Medicine and Cellular Longevity 2012 (2012) 11.
[340] T.F. Vandamme, J.F. Ngombo Mukendi, International Journal of Pharmaceutics 145 (1996) 77–86.
[341] R.A. Crane, T.B. Scott, Journal of Hazardous Materials 211–212 (2012) 112–125.
[342] Y.-P. Sun, X.-Q. Li, W.-X. Zhang, H.P. Wang, Colloids and Surfaces A: Physicochemical and Engineering Aspects 308 (2007) 60–66.
[343] M.-M. Song, W.-J. Song, H. Bi, J. Wang, W.-L. Wu, J. Sun, M. Yu, Biomaterials 31 (2010) 1509–1517.
[344] M. Mahmoudi, S. Sant, B. Wang, S. Laurent, T. Sen, Advanced Drug Delivery Reviews 63 (2011) 24–46.
[345] A.K. Gupta, M. Gupta, Biomaterials 26 (2005) 3995–4021.
[346] J.C. Middleton, A.J. Tipton, Biomaterials 21 (2000) 2335–2346.
[347] S. Dorozhkin, Journal of Materials Science 44 (2009) 2343–2387.
[348] M.P. Staiger, F. Feyerabend, R. Willumeit, C.S. Sfeir, Y.F. Zheng, S. Virtanen, W.D. Müeller, A. Atrens, M. Peuster, P.N. Kumta, D. Mantovani, F. Witte, Materials Science and Engineering B 176 (2011) 1596–1599.
[349] H. Windhagen, K. Radtke, A. Weizbauer, J. Diekmann, Y. Noll, U. Kreimeyer, R. Schavan, C. Stukenborg-Colsman, H. Waizy, Biomedical Engineering Online 12 (2013) 62.
[350] H.M. Wong, S. Wu, P.K. Chu, S.H. Cheng, K.D. Luk, K.M. Cheung, K.W. Yeung, Biomaterials 34 (2013) 7016–7032.
[351] S.-W. Hwang, H. Tao, D.-H. Kim, H. Cheng, J.-K. Song, E. Rill, M.A. Brenckle, B. Panilaitis, S.M. Won, Y.-S. Kim, Y.M. Song, K.J. Yu, A. Ameen, R. Li, Y. Su, M. Yang, D.L. Kaplan, M.R. Zakin, M.J. Slepian, Y. Huang, F.G. Omenetto, J.A. Rogers, Science 337 (2012) 1640–1644.
[352] L.L. Hench, J.M. Polak, Science 295 (2002) 1014–1017.